

Integral Support Structure and Controller Design of an Offshore Wind Turbine

D.T.B. Stinenbosch

Master of Science Thesis

Integral Support Structure and Controller Design of an Offshore Wind Turbine

MASTER OF SCIENCE THESIS

For the degree of Master of Science in Systems and Control at Delft
University of Technology

D.T.B. Stinenbosch

2 January, 2020

Faculty of Mechanical, Maritime and Materials Engineering (3mE) · Delft University of
Technology

SIEMENS Gamesa
RENEWABLE ENERGY

 **TU Delft** Delft
University of
Technology

Copyright © Delft Center for Systems and Control (DCSC)
All rights reserved.

DCSC

Abstract

In the past decade, the wind energy subsidies provided by the Dutch government is declining. In order to adopt wind energy as a well-established source of renewable energy, the costs of (offshore) wind energy should be lowered. This can be achieved by increasing the energy production or by lowering the maintenance and initial costs. In search of lowering the costs, the wind industry is pushing towards the boundary limits of design. The use of multi-objective design is needed for exploring those limits, for which the field of control and structural engineering get together. Currently, little research is conducted of combining controller and structural design in the wind turbine industry.

The goal of this thesis is to investigate the possibility of optimizing the support structure design and the controller design into one single optimization routine. The method describes the use of nonsmooth \mathcal{H}_∞ -synthesis. The modelling principles of the turbine makes use of different approaches. A simple finite element model of the wind turbine tower is constructed. The wall thickness of the tower sections is extracted as a tunable parameter, through an affine representation of the Ordinary Differential Equation (ODE).

In this thesis, the Controller Structure Optimization (CSO) for the offshore wind turbine combines the design of a load reducing Rotor Speed Controller (RSC) and wall thickness reduction. In theory, the bandwidth of the RSC is limited by the first tower bending mode. Therefore, the bandwidth of the designed controller is chosen well below the first eigenfrequency. It was found that the limitations do not influence the solution. The limitations of the proposed method are bounded by the weight functions, which impose a limit on the performance. Furthermore, it was found that the CSO framework can minimize the wall thickness of the tower elements, and simultaneously design a suitable RSC for tracking a rotor speed. The results are verified in high-fidelity wind turbine model, where the control-relevant subjects are addressed and specified. It was found that by addressing multi-objectives, we can design a controller with rotor tracking abilities and load reducing properties. Hence, the proposed CSO framework, can simultaneously design controllers and alter the structure and thereby increase the overall performance of the system.

Table of Contents

Preface	xi
1 Introduction	1
1-1 Motivation	1
1-2 Related research	4
1-3 Research objectives	5
1-4 Structure of the thesis	6
2 Theoretical background	9
2-1 The Offshore Wind Turbine	10
2-2 Controller Structure Optimization	14
2-3 Parameter Dependent State-Space models	15
2-4 Controller design framework	16
2-5 Summary	22
3 Structural sensitivity analysis	23
3-1 Modal Reduction	24
3-2 The extended system description	25
3-3 Showcase example: mass-spring-damper system	28
4 Modelling of the OWT	37
4-1 Aerodynamic model	38
4-2 Mechanical model	43
4-3 The complete OWT model	50
4-4 Summary	57

5 Preliminaries for the CSO	59
5-1 Controller design	60
5-2 Structural design	66
5-3 The resulting design cases	71
5-4 Summary	80
6 Simulation Results	81
6-1 Case 1: The Rotor Speed Controller	82
6-2 Case 2: The Rotor Speed Controller and Active Tower Damper	83
6-3 Case 3: Controller Structure Optimization	86
6-4 Summary of the cases	91
6-5 Verification with nonlinear simulations	92
6-6 Conclusion	95
7 Conclusions and Recommendations	97
7-1 Conclusion	97
7-2 Recommendations	99
A Preliminaries structural dynamics	103
A-1 Free vibration problem	103
A-2 Eigenfrequency sensitivity	104
A-3 Eigenmode sensitivity	104
B Definitions of the 8.0MW SGRE Wind Turbine	107
C Fatigue analysis	111
Bibliography	115
Glossary	119
List of Acronyms	119
List of Symbols	120

List of Figures

1-1	Estimated subsidy prices of offshore wind energy in cents per kWh over the years.	2
1-2	The ideal power curve with characteristic operating regions (Bianchi et al., 2006).	4
2-1	Schematic overview of a monopile foundation based Offshore Wind Turbine. . . .	10
2-2	Frequency design diagram of an Offshore Wind Turbine (OWT) incorporating the wave and wind spectra	11
2-3	Principal bending modes of an OWT at the left the Fore-Aft (FA) direction and at the right Side-Side (SS) direction.	11
2-4	General structure of the control problem for wind turbines. Flowchart is adopted from Shan (2018)	12
2-5	Generalized plant P with controller block K and model update block Δp which allows for parametric changes of the system.	17
2-6	Linear parameterization of a PID controller. The generalized plant is represented by the yellow box. (Van Solingen et al., 2014)	19
2-7	Simplified diagram of the generalized plant P , the weighting filters W_u, W_P and W_Δ . The controller diagonal K and the Δp are included, for which the latter allows for the structural perturbations.	19
2-8	Block diagram of a basic feedback loop. The controller is given by K . The external signals are the reference signal r , the load disturbance d_1 and the measurement noise d_2 . The process output and controller signal are given by respectively: h and u . Furthermore, there is the error signal e and measured output y	20
3-1	Double mass-spring-damper system interconnected through a spring k and viscous damper d	25
3-2	Eigenmodes of the double mass-spring-damper system.	29
3-3	Open-loop bode plot for the transfer relation of the position for x_1 and x_2 with as input the applied force F . For $m_1 = m_2 = 1$ and $k = 1; d = 0.05$	29
3-4	Model assurance criterion along linear varying a structural parameter (k, m_1, m_2) by a coefficient μ	31

3-5	Configuration of the plant and the controller for simultaneous design of plant and controller for the double mass-spring-damper system given by $G(s)$	32
3-6	The open-loop frequency response of the original system	34
3-7	The original open-loop frequency response and the updated system.	34
3-8	Step response of both the nominal case and the CSO case. A slight improvement of the CSO case with respect to the nominal case is noticed.	35
4-1	A schematic representation of the closed-loop wind turbine model based on Bianchi et al. (2006)	38
4-2	A schematic representation of the aerodynamic model inputs and outputs.	38
4-3	Nominal operating trajectory of the 8MW turbine obtained from BHAWC simulations.	40
4-4	Aerodynamic thrust F_T and torque T_r curves of 8.0MW Siemens Gamesa Renewable Energy (SGRE) wind turbine.	41
4-5	Aerodynamic gains of the 8.0MW SGRE turbine.	42
4-6	A schematic representation of the mechanical model inputs and outputs.	43
4-7	The tower consists of a finite number of shells. Each shell can be described by corresponding diameter D_i , length L_i and wall thickness t_i . Where i stands for the number of shells.	45
4-8	Deformation of a Timoshenko beam (blue) compared with an Euler-Bernoulli beam (red) under an applied shear force F and moment M . The total displacement is given by δ	45
4-9	Schematic representation of a lumped mass model of the 8.0MW SGRE wind turbine with corresponding coordinates.	46
4-10	Frequency response from thrust force at tower top F_T to acceleration \ddot{y}_t for the structural model of the wind turbine. Both the reduced and full model description is depicted.	50
4-11	Frequency response of multiple wind turbine models linearized around above-rated wind speeds.	51
4-12	Time domain simulation of the tower acceleration (above) excited by temporarily thrust force F_T (below).	53
4-13	Varying frequency $f(t)$ over time for Equation (4-18).	54
4-14	Time domain simulation of the tower acceleration (above) excited by a periodic force F_T (below).	55
4-15	The resulting rotor speed response of the high-fidelity BHAWC model (—) and the derived linear wind turbine model (---) are shown (above).	56
4-16	Relative error between the response of BHAWC model and the derived linear model for rotor speed	56
5-1	Flowchart of the structure of Chapter 5.	60
5-2	Rotor Speed Controller combined with Active Tower Damping.	62
5-3	Open-loop frequency response of subsystem $G_{\hat{\beta} \rightarrow \hat{\Omega}_r}$ from the variation in pitch angle $\hat{\beta}$ as input to the variation of the rotor speed $\hat{\Omega}_r$ as output.	63
5-4	Time domain simulation of applying a step input on the Closed-Loop (CL) subsystem $G_{CL, \hat{\beta} \rightarrow \hat{\Omega}_r}$ without control (—) and with control (—).	63

5-5	Frequency response of both the magnitude and phase for the initial tower control loop: Open-loop (—) versus the closed-loop (—).	65
5-6	Step response of an additional pitch actuation to tower acceleration. The open-loop (—) and the effect of including tower feedback control (—).	65
5-7	Eigenfrequency sensitivity for the two tower modes with respect to the vertical tower element number. (a) shows for the eigenvalue ω_{1st}^2 (b) shows for the eigenvalue ω_{2nd}^2	68
5-8	Modeshape sensitivity of different perturbations of wall thickness.	71
5-9	Inverse weight design of $W_{p,1}$ and $W_{p,2}$. which in series forms the final weight design $W_{p,rsc}$	73
5-10	Sensitivity plot of different CL systems using different controller parameters for the RSC.	73
5-11	Generalized plant description (yellow area) of the proposed \mathcal{H}_∞ problem for case 1.	74
5-12	Weight design of $1/W_{p,\ddot{y}_t}$, the Open-Loop (OL) system and CL subsystem for the initial control design is shown as well.	75
5-13	Generalized plant description (yellow area) of the proposed multi-objective problem of case 2.	76
5-14	Generalized plant configuration of the proposed CSO problem.	79
6-1	Resulting sensitivity plot for case 1.	83
6-2	Resulting sensitivity functions for case 2.	85
6-3	Resulting bode magnitude plot of the tower control-loop for case 2.	85
6-4	Bode magnitude plots of the sensitivity plot of case 3a	87
6-5	Bode magnitude plots for the perturbations channels are shown (a,b). The inverse weighting function of the static gain is shown as well.	88
6-6	Bode magnitude plots of the sensitivity plot of case 1.	89
6-7	Bode magnitude plots for the perturbations channels are shown (a,b), the inverse weighting function of the static gain is shown as well.	89
6-8	Grid search results of varying the wall thickness weights.	90
6-9	Time domain simulation of applying a mean wind speed of 18 m/s with a turbulence intensity of 10%.	93
6-10	Calculated damage for the tower top moment (a), the tower bottom moment (b) and pitch bearing damage (c) for the different control designs.	94
B-1	Schematic representation of a lumped mass model of the 8.0MW SGRE wind turbine with corresponding coordinates.	107
B-2	The element-wise thickness along the tower length (a) and the element-wise radius along the tower length (b).	109
C-1	The procedure of rainflow counting	112

List of Tables

2-1	Relevant operational signals and belongings for this work (Shan, 2018).	12
3-1	Sensitivity analysis (k, m_1, m_2) for the first and second eigenfrequency of the double mass spring damper system	30
4-1	Physical properties cylinders and thin walled cylinders ($t \ll r$)	44
4-2	Damping of the first two modes of the 8.0MW SGRE wind turbine model.	52
5-1	Locations of the OL poles and zeros for the subsystem $G_{\beta \rightarrow \hat{\Omega}_r}$	63
5-2	Modal Assurance Criterion (MAC) values for different wall thickness perturbations.	70
5-3	Parameters for the weight design of $W_{p, rsc} = \text{series}(W_{p,1}, W_{p,2})$	72
5-4	Weight selection for case 2.	77
5-5	Weight function design input values for the static constants.	79
6-1	Summary of the different design cases throughout this chapter	91
6-2	Comparison of the different control design cases simulated with the high-fidelity 8.0MW Bonus Horizontal Axis Wind turbine Code (BHAWC) model normalized with respect to case 1.	94
B-1	Numerical values for the Rotor Nacelle Assembly (RNA) of the 8.0MW SGRE wind turbine.	109
B-2	Element values and characteristics for the Euler-Bernoulli beam theory for the 8.0MW SGRE wind turbine.	110
B-3	Operating characteristics for the 8.0MW SGRE wind turbine	110

Preface

This thesis is written as the final work to complete the Master's programme Systems and Control at Delft University of Technology. This master thesis was carried out in the collaboration with Siemens Gamesa Renewable Energy in The Hague. The completion of this research marks the end of an extraordinary period.

I was not able to perform and complete the research without the help of others. First and foremost, I would show my sincere gratitude to my committee members. From the TU Delft, I would like to thank Jan-Willem van Wingerden and Joeri Frederik. Jan-Willem, thank you for introducing me to the interesting world of multi-variable control and your useful comments when I needed to find my way. Joeri, thank you for all the regular meetings and probably the countless hours assessing this thesis, your constructive feedback has been crucial in the development of this thesis.

Special thanks to my daily supervisor Bart-Jan van Roekel of Siemens Gamesa Renewable Energy. Bart, thanks for helping me to organize my thoughts during our nice weekly meetings, and always willing to have a small discussion whenever I got stuck. Your enthusiasm and support made it a very pleasant experience at SGRE.

Additionally, I would like to thank the whole SGRE team for the warm and open atmosphere at the office. In particular, I would like to thank Sachin, for helping me with the validation part through the in-house codes of SGRE. Furthermore, Ronald, Sara, Friso, Jason, Rameen and Matthijs for the interesting discussions about all the different thesis topics. But most of all, for providing the necessary distractions at the office.

Then of course, I would also like to thank my friends and family, especially my parents, for all their support over the past years. Finally, I would also like to thank Daniëlle for her support and advice during these past few months.

Chapter 1

Introduction

In this chapter, the topics related to the integral support structure and controller design are introduced. First, the motivation for doing this study is presented in Section 1-1, followed by the related research, which provides a first introduction to integral controller and structure optimization, in Section 1-2. Section 1-3 presents the research objectives. Finally, the structure of this report is presented in Section 1-4.

1-1 Motivation

On the 10th of July 2019, the second unsubsidized offshore wind farm, Hollandse Kust Zuid III-IV, located in the North Sea was permitted by the Dutch government. This wind farm will be the first operating wind farm in the North Sea, which will stop receiving subsidies and start paying ground rent instead ([Rijksoverheid, 2019](#)). Figure 1-1 depicts the trend of granting subsidies throughout the years for offshore wind farm projects in the Netherlands. It is interesting to see that this trend starts with a modest increase for the first realised wind farms followed by a spectacular dive in subsidy expenses. The main reason for this trend is that wind farms are becoming increasingly cheaper to exploit due to the higher efficiency of the wind turbines, making the realization less dependent on granted subsidies ([Algemene Rekenkamer, 2018](#)). A good part of costs is still being covered by the Dutch government, for example by providing site assessments of the location and connecting the wind farm to the national grid. For wind turbine manufacturers, the exponential decrease in subsidies should strongly motivate the production of even more efficient and long-lasting wind turbines compared to current standards. This will lead to wind turbine designs, which are genuinely competitive to the traditional oil-based power production. This in turn adds additional pressure to the improvement of the design cycle, the overall performance and the durability.

Therefore, this research aims to seek methods to further lower the Levelized Costs of Energy (LCoE) for wind turbines ([Mone et al., 2015](#)). There are several ways of lowering the LCoE, either in reducing the initial costs, or extending the lifetime of the turbine. Alternatively, the LCoE can be lowered by increasing the energy production over the wind turbine's

lifetime. Both the initial costs and the costs over the lifetime can be decreased by optimizing the design of the turbine.

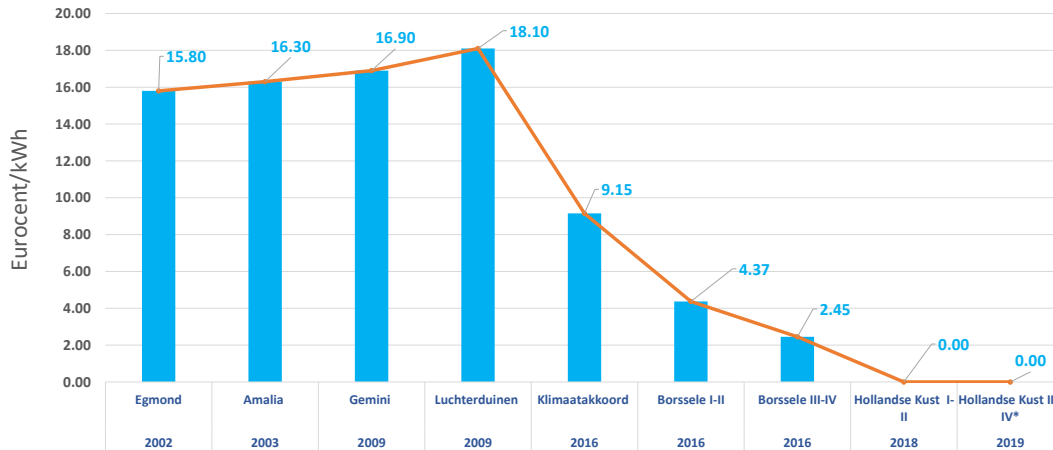


Figure 1-1: Estimated subsidy prices of offshore wind energy in cents per kWh over the years. The asterisk at Hollandse-Kust III-IV represents the only wind farm paying ground rent ([Algemene Rekenkamer, 2018](#); [Rijksoverheid, 2019](#)).

Currently, offshore wind turbines are designed conservatively in order to be certain they can withstand the rough conditions at sea. By optimizing the design of the support structure, it is possible to reduce the mass or increase the lifetime of the turbine and, subsequently, reduce the LCoE. The performance of the turbine design can be increased by implementing control systems. Therefore, the overall performance of a wind turbine is determined by both the controller and the structural parameters. The global optimum in lowering the LCoE will neither be achieved by only looking at the design of the support structure, nor by only looking at the control systems. Because of this, it is proposed to simultaneously consider the support structure and the controller design in order to achieve the global optimum.

Note that this integrated design is already applied in the world of precision systems in e.g. [Van der Veen et al. \(2017\)](#) and has been applied to a wind turbine in [Shirazi et al. \(2012\)](#). Therefore, in this thesis, it will be investigated whether the same sort of integrated design principles can be applied to an Offshore Wind Turbine (OWT) model. This research combines the objectives such as mass reduction of the tower with industry-standard low order control strategies.

Wind turbine design cycle

Within this work, the design cycle of the wind turbine combines the structural design and the controller design. This proposed design cycle simultaneously optimizes the controller and structure directly. The conventional design process of a wind turbine is as follows: firstly, the support structure is optimized through imposing mechanical objectives. The most mentioned objectives in literature are designing the first eigenfrequency in a certain range with respect

to the environment, and reducing the stresses. Such that the outcome satisfies the criteria of the designer. Afterwards, the active controller elements are optimized concerning the control objective (e.g., reducing disturbance, maximizing the bandwidth) leading to a re-evaluation of the structural design (Fischer et al., 2012). In practice, these teams of experts on one or several disciplines in a company finalize their design and hand it over to the next team. Such a multi-disciplinary design process will result in a time-consuming iterative process. In order to tackle this multi-disciplinary challenge, the approach of controller structure optimization is proposed. This implies coupling the controller and the structure design in one single optimization routine. The simultaneous redesign allows changes of the overall system, without iterating the structural and controller parts between different departments.

Control of wind turbines

In order to simultaneously alter the structure with the controller, the control system of the turbine should be explained. The control systems are one of the leading research areas of making wind turbine designs more efficient. The aim of the control system is to optimize the performance of the turbine design. This increase of the performance can be achieved through power maximization and (fatigue) load mitigation (Pao and Johnson, 2011). The controller objectives of a variable-speed variable-pitch wind turbine are different depending on the wind speeds. The objectives are related to the power versus wind speed curve, as shown in Figure 1-2, which consists out of the following four regions:

- **Region I** is when the wind speed is below the cut-in wind speed, $V_{wind} < V_{cut-in}$. In this case, the power available in the wind does not outweigh losses in the turbine system. Therefore, the wind turbine is kept at an idle or standstill operation by supervisory control (Bianchi et al., 2006).
- **Region II** is a partial load operation. The region comprises wind speeds between the cut-in and the rated wind speed $V_{cut,in} < V_{wind} < V_{rated}$. In this region, the turbine should extract as much power as possible from the wind. This extraction is done through operating the rotor at the maximum power coefficient while keeping the pitch angle constant. For variable-speed turbines, this is done through torque control (Bianchi et al., 2006).
- **Region III** comprises wind speeds such that the rated power can be extracted, which is given by $V_{rated} < V_{wind} < V_{cut-out}$. For the above-rated regime, the rated rotor speed and power output are maintained. By maintaining the rated rotor speed, no excessive mechanical loads occur on the wind turbine. Generally, for a variable-pitch wind turbine, this is achieved through Collective Pitch Controller (CPC), which alters the aerodynamic torque acting on the rotor.
- **Region IV** is when the wind speed exceeds the contains of region III, $V_{wind} > V_{cut-out}$. In this case, the wind turbine is shut down by supervisory control. This protects the system from high aerodynamic loading.

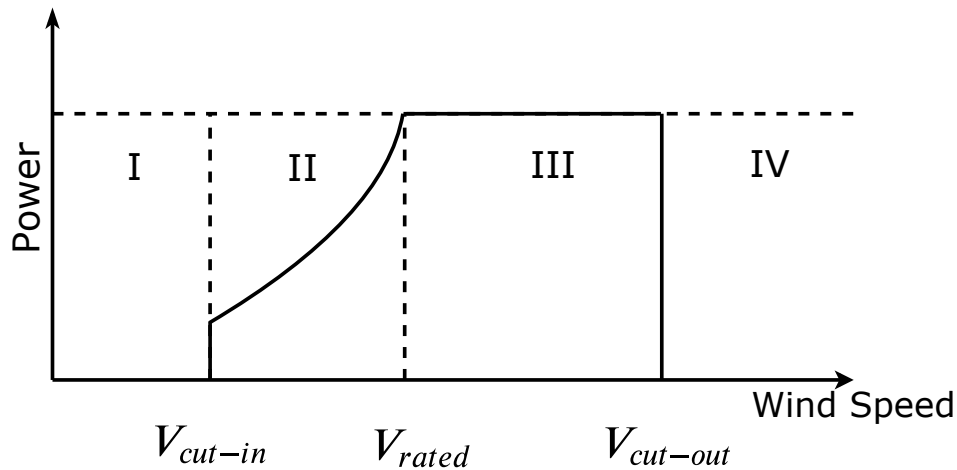


Figure 1-2: The ideal power curve with characteristic operating regions (Bianchi et al., 2006).

In region III, the controller aims to reduce the rotor speed fluctuations while limiting the loads on the turbine. This implies that the controller has multiple primary objectives. Therefore, this research focuses on the design of controllers applicable for region III. The foremost reason is that the two goals, of power maximization and a load mitigation, are addressed. Then, the resulting controller contributes to further LCoE reduction.

1-2 Related research

The field of coupling the controller and the structure in one single optimization routine is adopted in the field of high precision industry (Silva, 2009). Strict demands on the speed, weight and scale have made this multi-objective approach a necessity. For these motion systems, the interaction between the structural dynamics and the control system is crucial for achieving performance. However, the coupling between structural and controller parameters is not always known a priori, which makes it hard to assume that an optimal design can be obtained by dividing the original problem into sub-problems (Fathy et al., 2001).

Within the world of controller structure optimization, there are four different approaches to solving this problem of multi-objective design. These approaches are sequential design, iteratively, nested design or simultaneous (direct) design (Fathy et al., 2001). However, according to Silva (2009), there are two effective numerical strategies, namely the nested design and direct design. These methods are successfully applied in the work of Vandyshev et al. (2012) and Van der Veen et al. (2017) in order to optimize the closed-loop performance for simplified motion systems, where Vandyshev et al. (2012) compare the sequential design with the nested design approach, while Van der Veen et al. (2017) compare the sequential design with the direct design. Both the authors find slightly improved closed-loop performance for the nested and direct design approach with respect to the sequential design. Furthermore, the direct design method can be extended for the positioning of actuators and sensors as well by Van Herpen et al. (2014). Therefore, the method of direct design and nested design will be further investigated for application on an OWT .

Related research on the application of controller structure optimization on wind turbines is founded in the work of Shirazi et al. (2012) and Adegas (2013). Both the authors make use of solving Linear Matrix Inequalities (LMIs) in order to change the structure and controller simultaneously. Another method based on a robust based technique is proposed in Van Solingen et al. (2014) and Perez et al. (2016). This method involves fixed-structured robust techniques which are based on \mathcal{H}_∞ -controller synthesis algorithms (Apkarian and Noll, 2017). This approach allows for simultaneously designing the controller and the structure in one single optimization routine. Both the citations address that the difficulty of the method lies in how to impose the correct requirements on the \mathcal{H}_∞ minimization. The benefit of using the method is that all the objectives are addressed in frequency-domain specifications. The most profound reason for preferring the frequency-domain is because it has got insightful design tools like loop-shaping and Nyquist diagrams (Aström and Murray, 2010). Therefore, the framework directly provides an assessment of the closed-loop system performance.

Before one of these above mentioned controller-structure optimization methods can be applied, a suitable OWT model should be derived. Regarding the model, this work is done in cooperation with Siemens Gamesa Renewable Energy (SGRE), which provided the structural design of a full-scale 8.0MW offshore wind turbine. The design is recast into a usable mechanical model for controller design purposes. There are different kind of modelling concepts to model the mechanical structure of wind turbines. For an extensive overview of different methodologies, see Molenaar (2003). The mechanical model is based on principles of using finite element principles of creating a highly-detailed support structure design. Through the support structure model, the structural parameters related to the geometry can be extracted, e.g. the wall thickness. The principle of using a finite element based mechanical model introduces high order models, which are not directly suitable for control design (Arany et al., 2015).

A reduction method is needed to tackle the complexity of the high order model. The reduction method should preserve the most dominate dynamics of the wind turbine. Several ways of reducing high order mechanical models are presented in Cook et al. (2007) and Géradin and Rixen (2014). The reduced mechanical model can then be coupled with the aerodynamic model to obtain a controllable wind turbine system, as described in Bianchi et al. (2006). However, the aerodynamic model introduces non-linear behaviour. Therefore, for simplicity, the coupled wind turbine system is linearized for controller purposes.

1-3 Research objectives

This thesis explores the principles of multi-objective design by combining the controller and structure in one single optimization routine. The apparent benefit of using the integrated design routine becomes evident for the current time-consuming design cycle. The integrated design routine makes the iterative switching between design disciplines unnecessary. Therefore, the proposed framework should be considered for designing a full-scale wind turbine at SGRE. Based on this goal, the following main research objective is formulated:

"The main objective is to simultaneously optimize the integral support structure design and controller design for large scale offshore wind turbines."

The research objective can be divided into two sub-problems to create a guideline for the to-be performed activities and derivations throughout this thesis. The first challenge is to provide a suitable approach for simultaneous controller-structure optimization. It is still preferred to work with low order controllers as preferred in industry. Therefore, the chosen controller structure is fixed beforehand. Moreover, the evaluation of the overall system should be done in the frequency domain, as well. Performing the evaluation in frequency domain is preferred, because of the insightful tools (e.g. Bode plots, Nyquist), which is a direct measure of the closed-loop stability and performance of the overall system. The first sub-problem can be formulated as follows:

"Provide a framework for simultaneous structured controller design and tunable plant optimization through frequency-based optimization"

In line with the reduction of LCoE, the goal is to satisfy the controller objectives and at the same time, the structural objectives. The former is formulated by ensuring that the controller objectives (load mitigation and rotor speed tracking) are guaranteed. The latter is formulated by minimizing the wall thickness of the support structure. It is known that the structural deformations will influence the closed-loop performance of the system. Therefore, the second sub-problem will be the following:

"Apply the controller-structure optimization to prove its effectiveness on the linear 8.0MW SGRE wind turbine model, while achieving wall thickness reduction and rotor tracking performance."

It is chosen to use the 8.0MW SGRE wind turbine model to represent a large scale turbine. The main reason for this is that the full design of the support-structure can be used for publication with fewer confidentially issues. In the next section, it will be discussed how these problems are to be tackled through this thesis.

1-4 Structure of the thesis

This thesis is structured in the following way. This first chapter introduces the research goal of this work. Chapter 2 starts by presenting an OWT that will be used for the integrated design. Furthermore, the basic concepts for an OWT and controller-structure optimization methods are discussed. The chapter finishes with formalizing the integrated design problem. Since the structure of the system should be sensitive to structural perturbations, the system description is extended with additional inputs in Chapter 3. In addition, model reduction methods are applied to reduce the complexity of the system while preserving the most dominant dynamics. The chapter concludes with a showcase example of controller-structure optimization of a two Degrees of Freedom (DoF) mass-spring-damper system.

The next chapters are dedicated to the application of the integrated design framework to the 8.0MW SGRE wind turbine. In Chapter 4 a linearized wind turbine model is derived from the provided specifications of the 8.0MW SGRE wind turbine. It should be mentioned that the derived linear model uses a highly-detailed support structure model, where the wall

thickness is extracted as a tunable parameter. Before the controller structure optimization can be applied, some preliminaries are needed in Chapter 5. From these preliminaries different design cases are defined. These cases are simulated and will be presented in Chapter 6. The goal is to seek the effectiveness of the proposed integral method. The redesigned controller and structure are verified in a high-fidelity model of the wind turbine called Bonus Horizontal Axis Wind turbine Code (BHAWC). The thesis ends with the conclusions and recommendations for further studies in Chapter 7.

At the end of the thesis, appendices are included. The appendices provide relevant background information for respectively, the structural sensitivity analysis, the 8.0MW SGRE wind turbine specifications and the fatigue assessment. Note, it should be mentioned due to the use of confidential data some of the figures or tables are given without labels.

Theoretical background

The analysis of multi-objective design involving a combination of structural and controller optimization is well-known in the world of precision systems, see [Vandyshev et al. \(2012\)](#), [Silva \(2009\)](#). However, for larger mechanical systems, solving this integrated Controller Structure Optimization (CSO) problem is not common practice. Only a few applications can be found of integrated design for wind turbine design, an example being the work of [Shirazi et al. \(2012\)](#). From these current applications for both the precision systems and wind turbines is the increase of closed-loop performance by coupling the controller and the structure. The reason for increase of performance is mainly the physical interaction between the dynamics of the controller and the structure.

The aim of this chapter is to provide a single optimization routine for solving the multi-objective problem for an Offshore Wind Turbine (OWT). The chapter begins in Section 2-1 with presenting the lay-out of the 8.0MW Siemens Gamesa Renewable Energy (SGRE) offshore wind turbine and some explanatory information. Furthermore, it highlights the additional control objective for mitigating the movement in the fore-aft direction. Section 2-2 provides a brief overview of different methods for CSO and concludes with the chosen simultaneous CSO method. Thereafter, Section 2-3 and Section 2-4 introduce the preliminaries to enable the optimization, extracting the physical parameters of the system and the controller design framework, respectively.

2-1 The Offshore Wind Turbine

The OWT consists of multiple large components which are depicted in Figure 2-1. The components which are used throughout this thesis are briefly discussed. First of all, the foundation is used to embed the wind turbine into the seabed. The Transition Piece (TP) is placed on top of the tower. Subsequently, the Rotor Nacelle Assembly (RNA) is mounted on top of the tower. The RNA can be directly rotated towards the incoming wind. Furthermore, the blades of the turbine can pitch in and out of the wind. Through pitching, the rotor speed can be altered, and subsequently, the turbine is able to generate power at even higher wind speeds. The TP, the foundation and the tower altogether are called the support structure and this term will be used throughout this work.

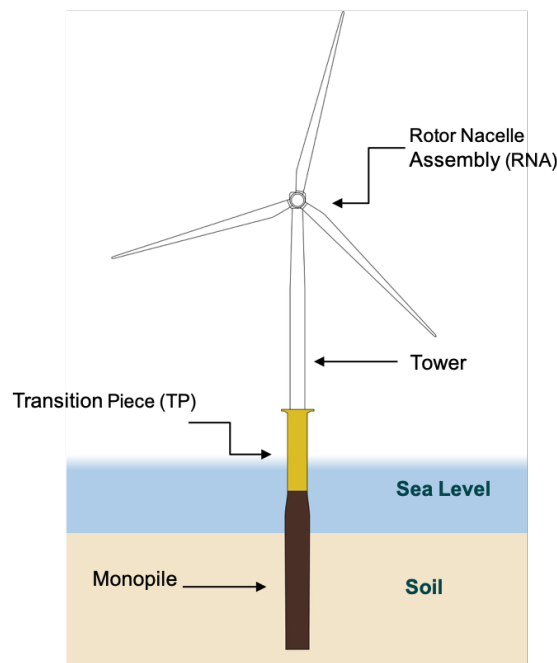


Figure 2-1: Schematic overview of a monopile foundation based Offshore Wind Turbine.

An OWT is continually subjected to wind and wave loading during its lifetime. By knowing the wind and wave conditions of a particular site, it is possible to design turbines that are able to withstand these loads. Moreover, an OWT is currently designed to withstand maximum loads at a given time, as well as suppressing cyclic loads during its entire lifetime. The former is addressed as Ultimate Limit State (ULS) and the latter as Fatigue Limit State (FLS). The fatigue loads are the main design driver for determining the structural integrity of the wind turbine components. Therefore, the amount of fatigue provides a good indication of the estimated lifetime of the turbine ([Hendriks and Bulder, 1995](#)).

Most wind turbines have an estimated lifetime of 25 years ([Jensen, 2019](#)). The fatigue damage is the predominant factor for the design of the support structure. Fatigue damage is the result of cyclic loading of a structure, resulting in microscopic fractures in the structure which grow over time. One can imagine that the lifetime is heavily influenced by the amplitude of

these loads. In order to mitigate the fatigue loads, the classical design approach is to avoid interference of the first eigenfrequency and the dynamics acting on the turbine (Damgaard et al., 2014). The so-called interference regions are visualized in Figure 2-2. The frequency ranges result from the excitation of wind and waves with the structure. The corresponding rotational frequency of the rotor (f_{1P}), the blade passing frequency (f_{3P}) and first natural frequency (f_0) are visualized in Figure 2-2, as well. The industry trend is developing bigger wind turbines in order to lower the costs (Wiser et al., 2016). By doing so, the tower length increases, which results in that the RNA is installed at a higher height. The higher top mass results in a lower first natural frequency. By itself, lowering the natural frequency is no problem. However, the wave spectra are located close to this frequency (Passon et al., 2015). This can be seen in Figure 2-2: if f_0 moves to the left, it coincides with the wave related frequencies. Hence, by lowering the eigenfrequency into the interference range higher loads are inevitable.

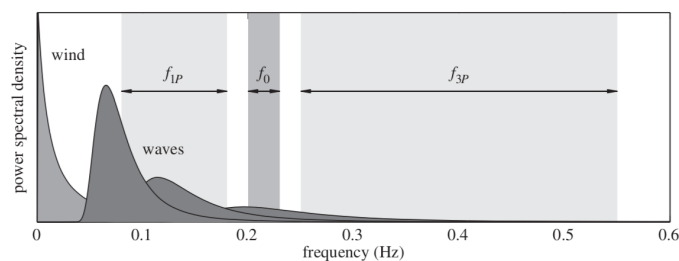


Figure 2-2: Frequency design diagram of an OWT incorporating the wave and wind spectra. The different operating regions are the rotational frequency (f_{1P}), the blade passing frequency (f_{3P}) and the first natural frequency (f_0).

By only describing the involved features of designing an OWT do not solve the load mitigation problem. Even if the turbine is not operating in the resonance regions, the turbine is still influenced by the wind and wave loading. The loading causes the turbine to move in different directions. The largest contribution of movement arises from the first bending modes of the structure. These modes move in the Fore-Aft (FA) and the Side-Side (SS) direction. To illustrate these directions of movement, the modes are depicted in Figure 2-3.

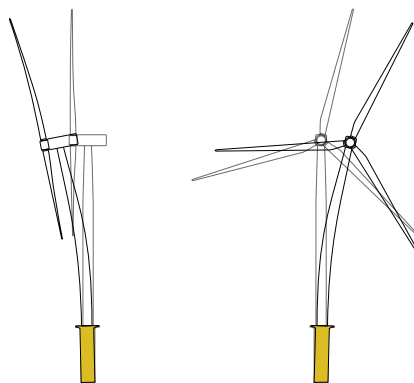


Figure 2-3: Principal bending modes of an OWT at the left the FA direction and at the right SS direction.

These movements can be actively influenced and suppressed by using different control methods. In this particular case, the movement is suppressed by pitching the rotor blades in and out of the wind. This results in alternating the aerodynamic forces, which results, when properly executed, in mitigation of these movements. Due to the fact wind turbines operate in stochastically varying wind fields, the effective wind speed acting on the rotor can have large sudden variations. As a consequence, there is a possibility that the relevant operational limits of the signals and loads are violated. Therefore, the primary objective of the designed controller is summarized as the suppression of external disturbances such that the limits of the operational signals are not exceeded. An overview of relevant operational signals and their corresponding limits for this work is given in Table 2-1, for a more extensive overview see [Shan \(2018\)](#).

Table 2-1: Relevant operational signals and belongings for this work ([Shan, 2018](#)).

Operational Signal	Physicals Limits
Rotor Speed Ω_r	Mechanical loads in rotor and drive-train
	Limitation of the rotational speed with respect to the induced voltage in the generator
Tower top acceleration \ddot{y}_t	Mechanical loads in tower and rotor blades
	Mechanical stresses in the components of the RNA

In general, the wind turbine control objectives and operational signals can be depicted as Figure 2-4. The figure shows the general structure of the control problem for wind turbines. The most profound external disturbance is the incoming turbulent wind field. The wind interacts with the aerodynamics of the turbine, resulting in fluctuations of the aerodynamic forces acting on the rotor. It can be seen that the generator torque is included in Figure 2-4 as well. However, the dynamics of the generator system is not included in this work. The reason for this is further explained in Chapter 4.

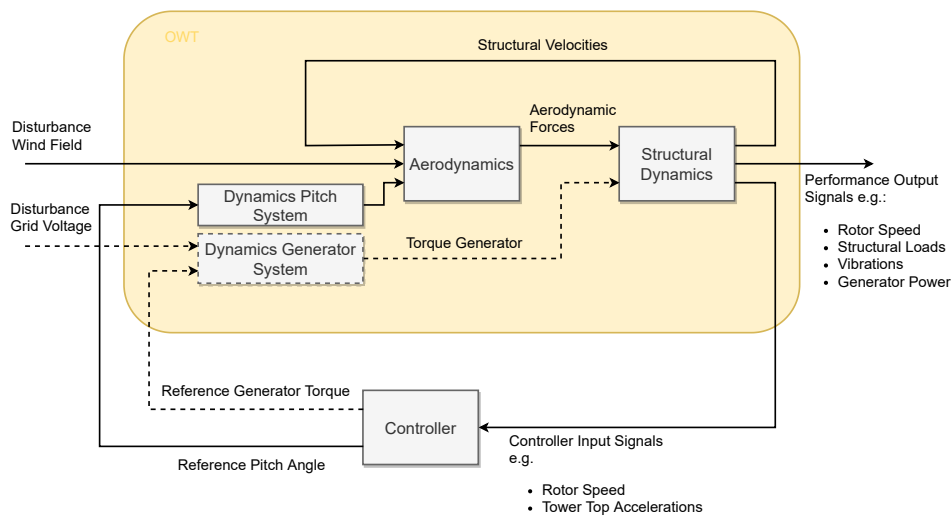


Figure 2-4: General structure of the control problem for wind turbines. Flowchart is adopted from [Shan \(2018\)](#).

Moreover, the trend of the control strategies for wind turbines is going towards multi-variable and multi-objective design. In this work, the multi-objective design originates from the operating region of the turbine, namely region III. The main objective of the pitch control design is the limitation on the rotor speed. As mentioned in Chapter 1, the controller has a major influence on the mechanical loads, especially for the tower and the blades. Therefore, another objective for control design is to keep the fatigue loads for the structural components below specified limits. These two objectives may conflict with one another. An example, that a more aggressive Rotor Speed Controller (RSC) tends to increase the fatigue loading of the tower [Tony \(2001\)](#). This results in conflicts between different controller objectives. As a consequence, modern multi-variable approaches are needed for finding an optimum between these control-objectives. The developed RSC in this thesis is based on those multi-variable approaches. These approaches guarantee closed-loop stability while minimizing the \mathcal{H}_∞ system norm of the plant. The interpretation of this system norm is shortly summarized, more details can be found in [Skogestad and Postlethwaite \(2007\)](#).

The \mathcal{H}_∞ -norm of a scalar transfer function is defined as the maximum value of the magnitude of the transfer function over all frequencies. For multi-variable plants, this is determined through the maximum of the largest singular value $\bar{\sigma}$ of the transfer function matrix $N(\omega)$ over all frequencies:

$$\|N(\omega)\|_\infty = \max_{\omega} \bar{\sigma}(N(\omega)) \quad (2-1)$$

The maximum singular value is an induced norm of the vector magnitude. It can be interpreted as maximum gain of the plant over all possible directions of the input vector v :

$$\bar{\sigma}(N) = \max_{v, |v|=1} |Nv| \quad (2-2)$$

The \mathcal{H}_∞ -norm is resembled as the worst case gain of a transfer function matrix over all directions and over all frequencies of the input vector. By using this for application of control design methods, an upper bound on the \mathcal{H}_∞ is placed:

$$\|N(\omega)\|_\infty \leq \gamma \quad (2-3)$$

Through doing so, the closed-loop system can be shaped in such a way that for example peaks are suppressed (increase the damping of certain modes). In this particular case, the \mathcal{H}_∞ -norm is minimized to mitigate the loads of the tower in the FA direction while regulating the rotor speed at a nominal value for high wind speeds. The SS suppression through active control methods is outside the scope of this work. Now that the main objective of the designed controller has been discussed. The next step is to combine this with the structural design of the wind turbine. In the upcoming section, a suitable method is chosen for combining the controller design with the structural design in one single optimization routine.

2-2 Controller Structure Optimization

As mentioned in Chapter 1, it is a well-known fact that the structure and controller are coupled (Vandyshev et al., 2012). To tackle the controller objectives of the wind turbine and allow the structure to alter, the overall system performance should be increased. The reason for the performance increase is investigated by Fathy et al. (2001) and it can be seen that the different strategies of combining the structure with controller design results in different optima. The additional objective of changing the structural design implies a multi-objective design approach. This will be referred to as integrated design or Controller Structure Optimization (Silva, 2009). Integrated design implies simultaneous controller and structure optimization. In literature, there are four different approaches to solve the involved multi-objective non-convex optimization. These approaches are sequential design, iteratively design, nested design and direct design (Fathy et al., 2001). However, according to Silva (2009), there are two effective numerical strategies, namely the nested design and direct design. In the following sections, nested design and direct design are briefly discussed.

Nested design

The nested design approach is a combination of nonlinear optimization methods and model-based control design techniques involving Riccati or Linear Matrix Inequalities (LMIs) approaches (Fathy et al., 2001). The procedure of this strategy is based on two different design loops. There is an inner loop which is responsible for the control derivation, enclosed by an outer loop which is responsible for changing the structural parameters and the closed-loop evaluation. The controller design can be done by using convex optimization. However, the outer-loop yields a non-convex optimization, which requires a nonlinear optimization method (e.g., genetic algorithms) Vandyshev et al. (2012). The final design is obtained when the outer loops converge to the constraints defined by the designer.

Direct Design

The direct design strategy involves a nonlinear optimization or genetic algorithm in order to simultaneously adjust the control and structural parameters to one another. Through this, the structural and controller parameters should always be accessible for the designer, leading to the condition that the controller structure is fixed beforehand. This condition implies that the system must be well understood in order to design a controller that meets the requirements. The driving factor of the direct design approach is that the dynamic response is evaluated through an objective function defined by the designer. There are two main different kinds of direct design found in literature, which are the following:

- **Gradient-based optimization:** Gradient-based optimization addresses the sensitivity of changing design parameters for the optimization of an objective function. These sensitivities provide insight into the magnitude and direction of changing parameters, as shown in Van der Veen et al. (2017). The main advantage of using this method is the evaluation of parameters in the frequency domain, for example, changing the overall system performance is directly noticeable through frequency response functions.

- **Non-smooth H_∞ synthesis:** The idea of using non-smooth H_∞ optimization is to simultaneously design the controller and the plant by looking at the frequency response. The method is successfully used in [Van Solingen et al. \(2014\)](#), where an example of a 2-DoF mass spring damper is presented. It makes use of an adjusted generalized plant which tolerates parameter changes while simultaneously adjusting the controller parameters. The system is extended in order to allow for parametric changes, as explained later in this work. The method makes use of non-smooth optimization for the integrated design problem. The gradient information is neither needed to change free parameters and nor convexity properties are required for the objective function ([Apkarian and Noll, 2017](#)).

Comparison of the different methods

The preferred method of CSO is the direct design method. The main reason for this originates from the fact of the simplicity of only having one design loop. Furthermore, a combination of gradient based and \mathcal{H}_∞ synthesis will be used. The structural parameters of the system will be altered by using the sensitivity of the system to perturbations in the structure. This works in the same manner as the gradient-based approach. These perturbations are included in the controller block of \mathcal{H}_∞ synthesis. The \mathcal{H}_∞ synthesis will include the use of fixed-structured controllers ([Apkarian et al., 2014](#)), which is preferred due to the fact the controller order can be assigned by the designer. Another possibility is using a series of LMIs for the \mathcal{H}_∞ synthesis. This approach is already applied on a wind turbine in the work of [Shirazi et al. \(2012\)](#). However, according to [Paijmans et al. \(2008\)](#) the integrated design problem can become infeasible for higher order models. Therefore, it is chosen to continue with the fixed-structured controller framework in combination with the gradient-based approach. The proposed framework allows for simultaneous redesign through frequency-domain evaluations of the system and provides an assessment of the closed-loop system performance.

The CSO routine combines the controller and the structure in one optimization routine. Therefore, the system description should be described by its structural parameters, which can then be extracted for the structural redesign. In the next section, the parameterization of the structure will be presented. Thereafter, the controller design framework will be discussed.

2-3 Parameter Dependent State-Space models

In order to execute the proposed CSO, the first step of the design approach is to parameterize the structure. This implies characterizing the structure through a few physical parameters such as tower length, wall thickness and diameter. These structural parameters are free for optimization and are admissible for changes. The structural dependencies of a model are represented through the scheduling parameter p . In the end, the optimization is performed in order to find the optimal values for this scheduling parameter $p \in \mathbb{R}^{n_p}$.

The parameter dependencies can easily be visualized by using linear Ordinary Differential Equation (ODE), which describe the dynamics of a mechanical system as follows:

$$M(p)\ddot{x} + D(p)\dot{x} + K(p)x = bF(t) \quad (2-4)$$

with $M \in \mathbb{R}^{n \times n}$ is a real symmetric positive definite mass matrix. Moreover, the damping matrix $D \in \mathbb{R}^{n \times n}$ contains the amount of energy dissipated by the system and the stiffness matrix $K \in \mathbb{R}^{n \times n}$ describes the elastic energy. The nodes of the model are given by x , which can be in translational or rotational (u_y, u_z, u_θ) . For example, for one single beam element the nodes are defined as $x = [u_{z_1} \ u_{y_1} \ u_{\theta_1} \ u_{z_2} \ u_{y_2} \ u_{\theta_2}]^T$, where the subscript 1 and 2 stands for the outermost points of the beam. With the parameter dependency, the ODE can be rewritten into a state-space model as follows:

$$\begin{bmatrix} \ddot{x} \\ \dot{x} \end{bmatrix} = \underbrace{\begin{bmatrix} -M(p)^{-1}D(p) & -M(p)^{-1}K(p) \\ I & 0 \end{bmatrix}}_{A(p)} \begin{bmatrix} \dot{x} \\ x \end{bmatrix} + \underbrace{\begin{bmatrix} M(p)^{-1}b \\ 0 \end{bmatrix}}_{B(p)} u \quad (2-5)$$

This modelling principle will be used for the parameterization of the wind turbine model in Chapter 4. The wind turbine model will be derived from multiple Ordinary Differential Equations (ODEs), which are parameterized through the wall thickness t of the tower section ($p = t_i$). The tower consist out of multiple sections with varying wall thickness. For example, the tower consist out of 3 sections with varying wall thickness constant over each section, then the scheduling parameter is given by:

$$p = \{t_1, t_2, t_3\} \quad (2-6)$$

Subsequently, the ODEs are recasted in the parameter dependent state-space form as in Equation (2-5). The structural parameterization discussed here will be combined with the controller design framework in the next section.

2-4 Controller design framework

With the system description now being parameter dependent, the next step is to set up a framework for which the controller can be designed simultaneously. One of the main challenges arises from the fact that control objectives must be transformed into frequency domain terms. Furthermore, the system must be extended in order to tolerate structural deformations. These structural deformations are addressed in frequency domain terms as well. This involves some necessary principles from multi-variable design as described in [Skogestad and Postlethwaite \(2007\)](#).

Generalized plant description

Figure 2-5 shows the necessary generalized plant description for the controller design framework and can be defined as follows:

$$\begin{bmatrix} z \\ y \end{bmatrix} = \underbrace{\begin{bmatrix} P_{11}(s) & P_{12}(s) \\ P_{21}(s) & P_{22}(s) \end{bmatrix}}_{P(s)} \begin{bmatrix} w \\ u \end{bmatrix} \quad (2-7)$$

with the following definitions: the performance channel z , the exogenous inputs w , the measured output y and the controller input u . The partitioning of the generalized plant P is

obtained by looking at the input-output transfer relations from $[w \ u]^T$ to $[z \ y]^T$ excluding the controller block K . The transfer functions of the partitioning of $P(s)$ are assumed to be stable. The next step is to find controllers, which guarantee closed-loop stability and nominal performance. The former can be achieved by incorporating output feedback to the generalized plant P with a stabilizing controller, as $u = Ky$. The latter can be achieved by looking at the following description of the closed-loop system, which is as follows:

$$\mathcal{F}_l(P, K) = P_{11} + P_{12}K(I - P_{22}K)^{-1}P_{21} \quad (2-8)$$

By definition, the obtained closed-loop transfer function is also known as the lower Linear Fractional Transformation (LFT). Closed-loop performance is determined by calculating the system norm. The goal is to find a suitable K that ensures $\|\mathcal{F}_l(P, K)\|_\infty < 1$. By minimizing this \mathcal{H}_∞ norm, a controller K which is based on the information in y , generates an input u which counteracts the influence of w on z , thereby minimizing the norm from w to z . The outcome of this \mathcal{H}_∞ -norm is called the performance index and will be referred to as γ .

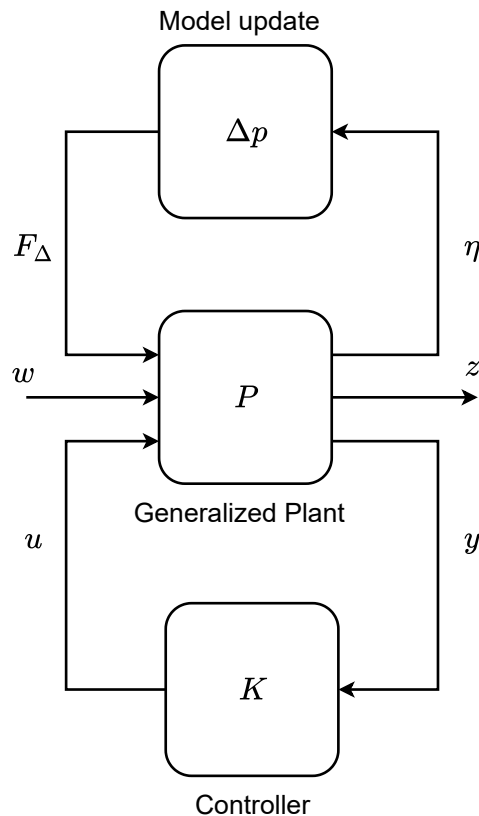


Figure 2-5: Generalized plant P with controller block K and model update block Δp which allows for parametric changes of the system. The signals of the plant are given by: the performance channel z , the disturbance channel w , the measured output y , the controller input u , the modal displacement vectors η and the perturbation input F_Δ .

Integral design framework

In the integral design framework the three main items of the CSO come together, namely, the controller, the structure and the optimization requirements. One can imagine that the optimization results from the specifications on the requirements on the controlled structure. Several examples can be given for these requirements, as an imposed bandwidth for the controller or a hard constraint on the structural deformation. Recall from the beginning of the section that the proposed problem is multi-objective.

These multi-objective approaches are normally specified by weighting functions. Each weight corresponds to one of the objectives. Therefore, the specifications or performance of the system can be enforced in terms of weighting functions. By means of suitable weighting functions, it is possible to define an upper bound of the closed-loop system transfer functions. Furthermore, the proposed CSO uses fixed-structured controllers, which is already applied by [Van Solingen et al. \(2014\)](#) for simultaneously varying the controller and structural parameters. By using the knowledge obtained from the work of Van Solingen an integrated design approach can be formulated with the following reasoning:

- In industry, low order controllers are still preferred to high order controllers. The main reason is that there are practical restrictions regarding the implementation. Therefore, the obtained controller K can be expressed through linear parameterized gains, an example of a parameterization of a simple PID controller is given by:

$$K_{PID}(s) = K_p + \frac{K_i}{s} + \frac{K_d s}{T_f s + 1} \quad (2-9)$$

The gains of the controller are stacked in a vector $\phi_{PID} = [K_p \ K_i \ K_d]^T$. Thereafter, the vector ϕ_{PID} is used to obtain a diagonal controller as depicted in Figure 2-6. Notice that the integrator and time delay term are merged into the generalized plant description.

- The simultaneous CSO is made available by extending the system in order to alter the structure as well. This is made available through a diagonal gain matrix Δp . Through this gain matrix, the tunable parameters of the system are accessible and tuned in the same manner as the controller gains. The method of extending the system will be presented in Chapter 3. Furthermore, the controller block K is diagonally structured as well as the aforementioned example of the PID controller.

The extended generalized plant for the simultaneous controller and structural redesign is shown in Figure 2-7. The proposed problem makes use of the control related sensitivity functions, which will be presented in the next section.

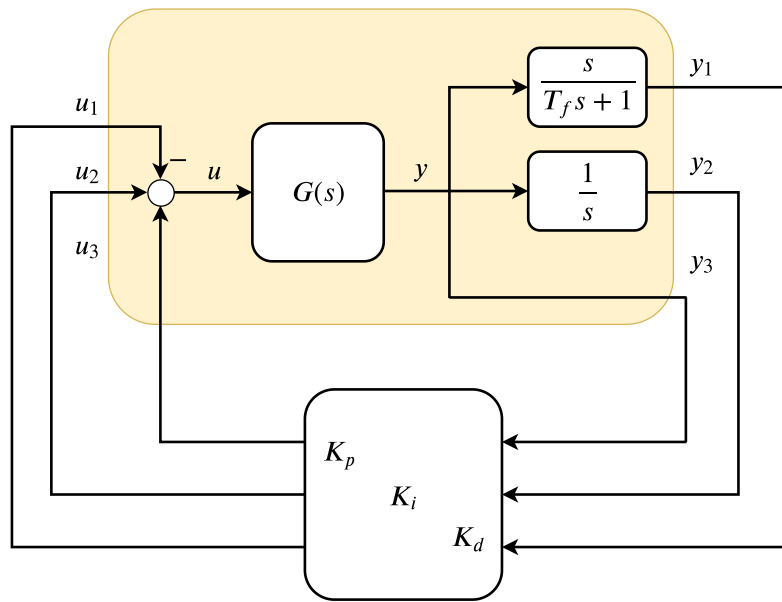


Figure 2-6: Linear parameterization of a PID controller. The generalized plant is represented by the yellow box. (Van Solingen et al., 2014)

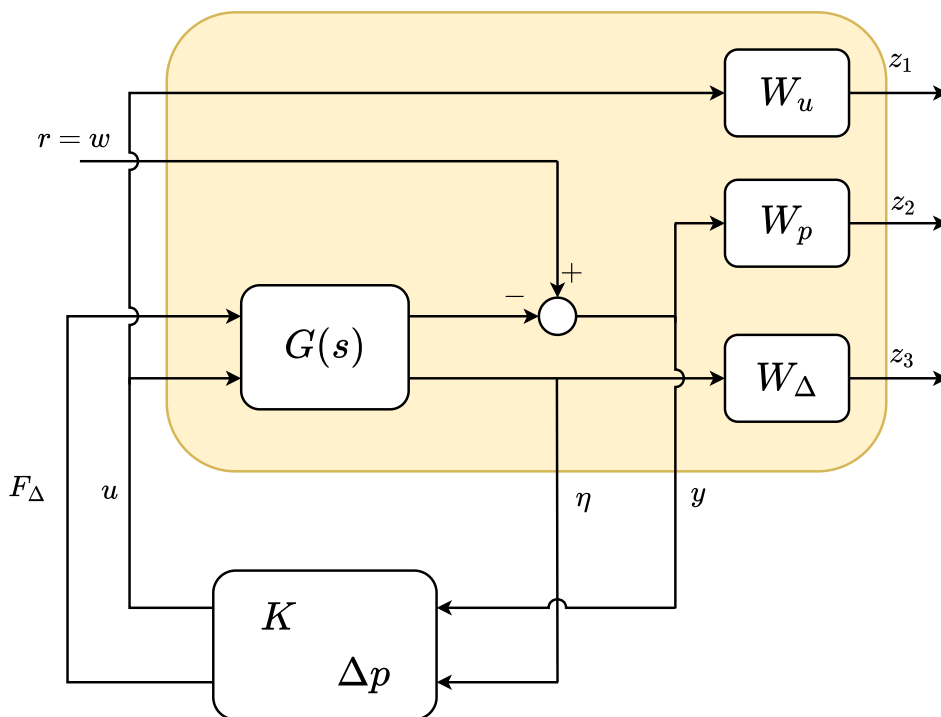


Figure 2-7: Simplified diagram of the generalized plant P , the weighting filters W_u , W_p and W_Δ . The controller diagonal K and the Δp are included, for which the latter allows for the structural perturbations.

Sensitivity analysis

The basic formulation of the integrated design problem was discussed in the previous section. It is stated that the \mathcal{H}_∞ norm should be minimized to a certain performance index γ . Keep in mind that closed-loop stability and desired performance of the controller is guaranteed when $\|\mathcal{F}_l(P, K)\|_\infty < 1$. From classical control theory, the performance of the controller is analysed through the sensitivity function S . This shows whether the closed-loop system is able to attenuate disturbances (Skogestad and Postlethwaite, 2007).

The classical negative feedback control loop model is shown in Figure 2-8. The aim for the control loop is to track the reference signal r with the output y . The relative error between these two $e = r - y$ is fed into the controller K . The controller gives an input signal u . Thereafter, a disturbance signal d_1 is added to the input signal u , the addition $v = u + d_1$ is fed into the plant G . The outcome is disturbed by an additional noise signal (measurement noise), which results in output signal h of the plant, resulting in the measured output $y = d_2 + h$.

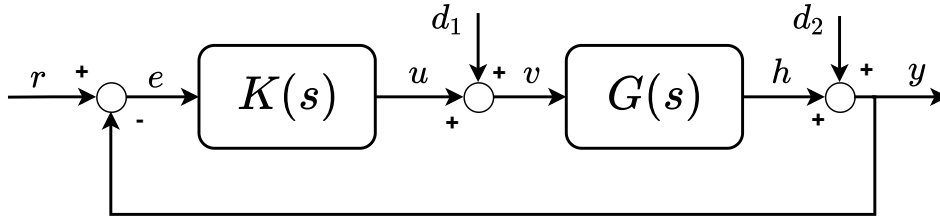


Figure 2-8: Block diagram of a basic feedback loop. The controller is given by K . The external signals are the reference signal r , the load disturbance d_1 and the measurement noise d_2 . The process output and controller signal are given by respectively: h and u . Furthermore, there is the error signal e and measured output y .

Then, as described in Aström and Murray (2010), the linear behaviour of the system is determined through the following four transfer functions presented in Equation (2-10).

$$\begin{aligned} S &= \frac{y}{d_2} = \frac{1}{1+GK} & GS &= \frac{y}{d_1} = \frac{G}{1+GK} \\ T &= \frac{y}{r} = \frac{GK}{1+GK} & KS &= \frac{u}{r} = \frac{K}{1+GK} \end{aligned} \quad (2-10)$$

It is assumed that the system has pure error feedback. These transfer functions are also known as the "Gang of Four". From these four, the example is made with the sensitivity function S , which is naturally related to the disturbance rejection of the system. It is a direct measure of how the error relates to the reference signal, or how much influence the disturbance will have on the tracking abilities of the system. These properties hold for both Single-Input Single-Output (SISO) and Multiple-Input Multiple-Output (MIMO) systems.

Considering a MIMO system, the effectiveness of the designed controller can be determined by the ratio of $\frac{\|e\|_2}{\|r\|_2}$. The following relation is given for this ratio:

$$\underline{\sigma}(S(j\omega)) \leq \frac{\|e(\omega)\|_2}{\|r(\omega)\|_2} \leq \bar{\sigma}(S(j\omega)) \quad (2-11)$$

where $\bar{\sigma}(S(j\omega))$ indicates the largest singular value of $S(j\omega)$ and $\underline{\sigma}(S(j\omega))$ the lowest singular value. The singular values correspond to the directions of the smallest and the biggest gains of $S(j\omega)$. The bandwidth of the system is related to those singular values. For SISO systems, the bandwidth of the system is given by the frequency where the sensitivity function $S(j\omega)$ crosses the -3 [dB]-line from underneath in a bode diagram. For MIMO systems, the bandwidth is given by a region. This region is indicated by the frequencies between where $\underline{\sigma}(S)$ and $\bar{\sigma}(S)$ crosses the -3 [dB], where the former is the best-case scenario and the latter the worst-case scenario.

These requirements can be combined in the following stacked problem:

$$\begin{aligned} \min_{K, \Delta p} \quad & \gamma \\ \left\| \begin{array}{c} W_p S \\ W_\Delta T \\ W_u K S \end{array} \right\|_\infty & < \gamma \end{aligned} \quad (2-12)$$

where K and Δp should stabilize the system. The proposed problem of Equation (5-18) makes use of multiple performance channels (z_1, z_2, z_3), each with their corresponding weight function (W_p, W_u, W_Δ). These weights will be explained in consecutive order, the weight W_p bounds the sensitivity function S in order to achieve the desired bandwidth of the designed controller K . In order to prevent too large inputs to the system $G(s)$, a bound is placed on KS . To make sure that the system has a structural deformation, a bound is placed by W_Δ on the extended system description as explained in Chapter 3. Notice, that the weight W_Δ bounds the complementary sensitivity T of the extended system description and enforces structural perturbations.

Furthermore, the considered \mathcal{H}_∞ problem is formed by the maximum singular value for each individual weight with corresponding transfer function. The largest singular value of $\bar{\sigma}(S)$ bounds the performance, $\bar{\sigma}(T)$ for the structural deformations, and $\bar{\sigma}(KS)$ penalizes large inputs to the plant. These values can be determined by analyzing the matrices obtained from a Singular Value Decomposition (SVD). Now that we have discussed all the relevant theories, it can be applied to the OWT model in Chapter 5.

Optimization solver

The proposed direct design framework is non-convex and nonlinear. In order to obtain fixed-structured controllers and optimize the structural parameters a solver is needed. The proposed \mathcal{H}_∞ controller synthesis is implemented in *MATLAB* in the work of [Apkarian and Noll \(2017\)](#). The toolbox is used to solve the \mathcal{H}_∞ controller design problem of Equation (5-18) and is discussed next. The proposed toolbox is already implemented in the *Robust Control Toolbox* of *MATLAB*. The choice for using the *Robust Control Toolbox* over the LMIs solvers, especially with the former being a black-box optimization routine, is mainly based on the aforementioned numerical problems in which the LMIs routine of higher order models can run into.

Moreover, the main benefits of using this fixed-structured controllers through the *Robust Control Toolbox* are the following:

- When a suitable controller structure is defined for the system, simultaneous design of decentralized controllers is possible. This implies the applicability of the structural optimization, which are simultaneously determined in an overall design/optimization process.
- Relating this to standard robust control design of wind turbines, the fixed and decentralized controller structure is well suited for gain scheduling or controller switching between different operation regions of the turbine.
- The computed controllers are always internally stable.

However, one certain drawback arises from the non-smooth behavior of the *Hinfstruct* algorithm. Namely, small changes in the weighting function parameters can result in completely different controller transfer function. This results in different performance magnitudes. This behavior makes it more difficult to apply this fixed structured control design in a higher level controller tuning approach. This will not throw a spanner in the works, because the proposed controller design has to be of a low order.

2-5 Summary

A general overview is presented of different methods for controller and structure design. The chosen method combines the work of [Van der Veen et al. \(2017\)](#) and [Van Solingen et al. \(2014\)](#) into one single optimization routine. The assumption is made that structure of the controller is simple and sufficient for industry purposes. The involved multi-objective design is captured by using a stacked (mixed-) sensitivity framework, which is solved by using the \mathcal{H}_∞ method of [Apkarian and Noll \(2017\)](#). Then the controller and structure are evaluated in frequency domain terms. However, the method of extending the system with additional inputs, which allows for structural alterations has not been investigated yet. Therefore, Chapter 3 will present this structural framework.

Structural sensitivity analysis

In the previous chapter, the fixed-structured control problem is defined which allows for perturbations of tunable elements in the plant description. In order to address or influence these tunable elements, it is still needed to extend the system description.

The integrated design method combines the work of [Van der Veen et al. \(2017\)](#) and [Van Solingen et al. \(2014\)](#), which results in a different framework as presented Chapter 2. The integral method of simultaneously varying the controller and structural parameters makes use of gradient-based principles. These principles involve the analysis of the eigenfrequency sensitivity. The goal of this chapter is to recast this sensitivity principle into a usable parameter for extending the system description. Subsequently, the structure is able to alter through the extension, given the fact that the eigenmodes do not change shape. Therefore, the influence of changing structural parameters on the eigenmodes is included in the analysis.

The structural sensitivity analysis should be applicable for the support structure of the wind turbine. In this thesis, a detailed support structure model are used. As a result, the dynamics of support structure is described by a high ordered model, which is not suitable for control design or time-domain simulations. Therefore, this chapter starts with the principle of modal reduction in Section 3-1. Thereafter, in Section 3-2 two methods of extending the system description are presented and concludes on a chosen extension method. Then the structural parameters are accessible for optimization. Finally, the technique of extending the system description, and subsequently, Controller Structure Optimization (CSO) is applied on a two degrees of freedom mass-spring-damper system. Specifically the eigenfrequency and eigenmodes sensitivity analysis is needed for mapping the boundaries of the applied CSO method.

3-1 Modal Reduction

For simple mechanical systems with just a few Degrees of Freedom (DoF), the structural mass M , damping D and stiffness K matrices can be used directly for control design, analyses and time-domain simulations. However, the derived model of the Offshore Wind Turbine (OWT) is described by higher order matrices. Therefore, model reduction methods are needed in order to make the model suitable for analysis (Molenaar, 2003). The quality of the model reduction method arises from the capability of capturing the important dynamics. In the end, the predominant dynamics of the original system should be preserved. Additionally, most systems operate at low frequencies making the higher-order modes (high frequencies) less valuable for incorporating in the analysis. Therefore, these high-order modes can be discarded. In this thesis, modal truncation is used, because it is relatively easy from the truncation to obtain reduced state-space models. The method is adopted from the work of Cook et al. (2007). Starting with the general expression of the aforementioned Ordinary Differential Equation (ODE) by describing an arbitrary mechanical system:

$$M\ddot{x} + D\dot{x} + Kx = bF(t) \quad (3-1)$$

The reduction method uses the modal displacement and starts with solving the generalized eigenvalue problem of Equation (3-1). The generalized eigenvalue problem is the same as a free vibration problem and is explained in Appendix A. The result of the derivation is adopted from Appendix A and is as follows:

$$(K - \omega_j^2 M)\phi_j = 0 \quad (3-2)$$

where the ϕ_j is the mode shape corresponding to the eigenfrequency ω_j of the system with modes $j \in \{1, \dots, n\}$. The next step is assuming that the ODE of Equation (3-1) can be described by the system response:

$$\begin{aligned} x(t) &= \sum_{j=1}^n \phi_j \eta_j(t) \\ &= \begin{bmatrix} \phi_1 & \phi_2 & \dots & \phi_n \end{bmatrix} \begin{bmatrix} \eta_1(t) \\ \eta_2(t) \\ \vdots \\ \eta_n(t) \end{bmatrix} \\ &= \tilde{V} \eta(t) \end{aligned} \quad (3-3)$$

where $\tilde{V} \in \mathbb{R}^{n \times k}$ is a matrix containing all the eigenmodes of the original system. Furthermore, the η is defined as the modal displacement, which is a set of modal coordinates corresponding to the coordinates of the modeshape ϕ_j . Notice that each element of η_j is multiplied with one corresponding eigenmode ϕ_j . Furthermore, each eigenmode has its own corresponding eigenfrequency ω_r . These are sorted on the diagonal matrix $\tilde{U} \in \mathbb{R}^{k \times k}$. It can be seen that the elements of $\eta(t)$ represent the number of Degrees of Freedom participating in describing the dynamics of the total system. Equation (3-3) describes the full dynamics over the whole frequency range of the system. In order to obtain a reduced order model, a number of modes is selected. By doing so, the modes of interest are selected and induce the

dynamical behavior of the reduced system. The number of modes contributing to the reduced system description is denoted by m . Subsequently, the system response of Equation (3-3) is reduced according to Equation (3-4):

$$\begin{aligned} x(t) &= \sum_{j=1}^m \phi_j \eta_j \\ &= \tilde{V}_r \eta(t) \end{aligned} \quad (3-4)$$

The ODE of Equation (3-1) can now be rewritten by multiplying each element with the selected eigenmodes, which is represented by the reduced matrix \tilde{V}_r as follows:

$$\underbrace{\tilde{V}_r^T M \tilde{V}_r}_{:=\tilde{M}_r} \ddot{\eta}(t) + \underbrace{\tilde{V}_r^T D \tilde{V}_r}_{:=\tilde{D}_r} \dot{\eta}(t) + \underbrace{\tilde{V}_r^T K \tilde{V}_r}_{:=\tilde{K}_r} \eta(t) = \underbrace{\tilde{V}_r^T b}_{:=\tilde{F}_r} F(t) \quad (3-5)$$

The principles of model reduction are discussed above and will be used in the extending system description in Section 3-2. Furthermore, the method of model reduction will be used for the mechanical model of the derived wind turbine model in Chapter 4 as well.

3-2 The extended system description

In order to allow for simultaneous controller and structure redesign, the system must be extended. The structural dependencies are extracted from the system description. This can be achieved through different methods, namely through extension using internal forces or an affinely-dependent system description. The two methods are discussed with the use of the double mass-spring-damper system of Figure 3-1. The following differential equation of Equation (3-6) describes the double mass-spring-damper system.

$$\underbrace{\begin{bmatrix} m_1 & 0 \\ 0 & m_2 \end{bmatrix}}_M \begin{bmatrix} \ddot{x}_1 \\ \ddot{x}_2 \end{bmatrix} + \underbrace{\begin{bmatrix} d & -d \\ -d & d \end{bmatrix}}_D \begin{bmatrix} \dot{x}_1 \\ \dot{x}_2 \end{bmatrix} + \underbrace{\begin{bmatrix} k & -k \\ -k & k \end{bmatrix}}_K \begin{bmatrix} x_1 \\ x_2 \end{bmatrix} = \underbrace{\begin{bmatrix} 1 \\ 0 \end{bmatrix}}_b F(t); \quad (3-6)$$

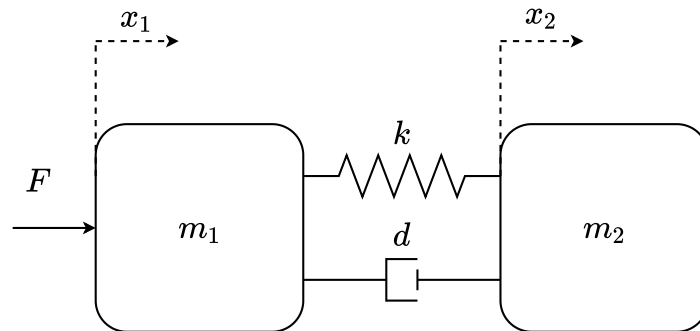


Figure 3-1: Double mass-spring-damper system interconnected through a spring k and viscous damper d .

The state-space representation is obtained by recasting the structural matrices and defining the states of the system as $[\dot{x}_1 \ \dot{x}_2 \ x_1 \ x_2]^T$. Furthermore, the outputs of the systems are the position of the masses, which are respectively x_1 and x_2 . Notice, that from the input F to x_1 the input is directly applied to the output y_1 (collocated) and from F to x_2 the input works not directly on the output y_2 (non-collocated). The full description of state-space realization is as follows:

$$\left\{ \begin{array}{l} \begin{bmatrix} \ddot{x}_1 \\ \ddot{x}_2 \\ \dot{x}_1 \\ \dot{x}_2 \end{bmatrix} = \begin{bmatrix} -d/m_1 & d & -k/m_1 & k \\ d & -d/m_2 & k & -k/m_2 \\ 1 & 0 & 0 & 0 \\ 0 & 1 & 0 & 0 \end{bmatrix} \begin{bmatrix} \dot{x}_1 \\ \dot{x}_2 \\ x_1 \\ x_2 \end{bmatrix} + \begin{bmatrix} 1 \\ 0 \\ 0 \\ 0 \end{bmatrix} F(t) \\ \\ \begin{bmatrix} y_1 \\ y_2 \end{bmatrix} = \begin{bmatrix} 0 & 0 & 1 & 0 \\ 0 & 0 & 0 & 1 \end{bmatrix} \begin{bmatrix} \dot{x}_1 \\ \dot{x}_2 \\ x_1 \\ x_2 \end{bmatrix} \end{array} \right. \quad (3-7)$$

For a more brief approach of recasting Equation (3-6) into a state-space form is given by Equation (3-8), and will be used in the upcoming sections.

$$\begin{bmatrix} \ddot{x} \\ \dot{x} \end{bmatrix} = \underbrace{\begin{bmatrix} -M^{-1}D & -M^{-1}K \\ I & 0 \end{bmatrix}}_A \begin{bmatrix} \dot{x} \\ x \end{bmatrix} + \underbrace{\begin{bmatrix} M^{-1}b \\ 0 \end{bmatrix}}_B F(t) \quad (3-8)$$

Extending with forces

This extension method is adopted from the work of [Van Solingen et al. \(2014\)](#). By using the extension through forces, then the structural parameters can be extracted by introducing an external force F_{ext} . For the mass-spring damper system, an external force replaces the actual spring stiffness by working on both the masses, as $F_k = k(x_2 - x_1)$. This reasoning can be applied for the damping constant, $F_d = d(\dot{x}_2 - \dot{x}_1)$ as well. The state-space representation of Equation (3-8) can be extended. By adding the internal forces of the spring and damper as function of respectively the position and velocity to the original input force $F(t)$.

$$F_{ext} = \begin{bmatrix} 1 & -1 & -1 \\ 0 & 1 & 1 \end{bmatrix} \begin{bmatrix} F(t) \\ F_k(t) \\ F_d(t) \end{bmatrix} \quad (3-9)$$

Notice that the input of the system is extended from one to three and the original b is included as well. The expression of Equation (3-9) is substituted in Equation (3-8) and the following extended state-space relation is derived:

$$\begin{bmatrix} \ddot{x} \\ \dot{x} \end{bmatrix} = \begin{bmatrix} 0_{2 \times 2} & 0_{2 \times 2} \\ I_{2 \times 2} & 0_{2 \times 2} \end{bmatrix} \begin{bmatrix} \dot{x} \\ x \end{bmatrix} + \begin{bmatrix} M^{-1}F_{ext} \\ 0_{2 \times 1} \end{bmatrix} \quad (3-10)$$

This method works as long as the structural dependencies can be made explicit through forces. By using this method, the spring and damper are replaced by forces acting on the system. However, instead of replacing the structural parameters with forces, they could be an addition to the system, like in the work of [Van Herpen et al. \(2014\)](#). The additional spring or damper correlates with the nominal value instead of a complete replacement. This could be beneficial for the design freedom of the structural parameters. However, for complicated physical systems it is rather difficult to extend the system through forces. Therefore, a different method is proposed using linear perturbations of the system parameters in the following section.

Affinely-dependent parameters

Due to the fact that the support structure of the wind turbine consists of multiple nodes, the approach of extracting the structural parameter through forces is time-consuming and not that straightforward. Therefore, the approach of extending the system through affinely-dependent parameters is proposed. This approach makes use of the original structural matrices (M, D, K) and split them in a summation of each structural matrix through a linear dependent parameter, for example a wall thickness parameter in Chapter 4. The extraction of the linear parameter makes it available for optimization. This approach originates from integrated design applications using Linear Matrix Inequalities (LMIs), as in the work of ([Grigoriadis and Skelton, 1998](#)). The structure is allowed to change by linearly varying the matrices in the description of Equation (2-4). This statement holds: first of all, when the structural parameters are linear terms in the system description ([Grigoriadis and Skelton, 1998](#)). Secondly, the structural perturbations are enforced by inputs to the actual system ([Apkarian and Noll, 2017](#)), like explained in Chapter 2.

The perturbations are formulated by looking at the work of [Van der Veen et al. \(2017\)](#), in which sensitivities of changing the mass and stiffness matrices are considered. Using this approach, the underlying sensitivities of parameters are mapped ([Gérardin and Rixen, 2014](#)). The parameter for which the sensitivity is computed is a property of the mass and stiffness matrix. In this thesis, the sensitivity assessment for mass and stiffness matrix is done for the wall thickness of the support structure. Furthermore, for most physical systems changing physical properties influences the mass and stiffness matrix in a coupled manner. The sensitivity matrices for the mass and stiffness matrices are as follows:

$$M(\Delta p_i) = \frac{\partial M}{\partial p_i} \Delta p_i \quad K(\Delta p_i) = \frac{\partial K}{\partial p_i} \Delta p_i \quad (3-11)$$

The next step is to use the expression of Equation (3-11) and convert it to an affine property of the system. This is achieved by computing for each structural perturbation Δp_i , the corresponding sensitivity of the mass and the stiffness matrices ([Gu et al., 2005](#)). The overall structural change of the mass and stiffness matrix can be resembled by a summation along the total number of perturbations n . The expression using the total number of perturbations is as follows:

$$M = M_0 + \sum_{i=1}^n \frac{\partial M}{\partial p_i} \Delta p_i \quad K = K_0 + \sum_{i=1}^n \frac{\partial K}{\partial p_i} \Delta p_i \quad (3-12)$$

where the subscript 0 at the structural matrices (M, D, K) stands for the initial unperturbed matrices, which are constant regardless of the change of the parameters in p_i . Subsequently,

Equation (3-12) is substituted in the following parameter dependent ODE resulting in an extended system description:

$$M(p)\ddot{x} + D(p)\dot{x} + K(p)x = bF(t) \quad (3-13)$$

where the structural parameters p can be varied as inputs for the system as Equation (3-15). Hence, it is now possible to incorporate this procedure on the integral controller and support structure design of a wind turbine in Chapter 5.

$$M_0\ddot{x} + D_0\dot{x} + K_0x = \begin{bmatrix} -\sum_{i=1}^n \frac{\partial M}{\partial p_i} \Delta p_i & -\sum_{i=1}^n \frac{\partial K}{\partial p_i} \Delta p_i & b \end{bmatrix} \begin{bmatrix} \ddot{x} \\ x \\ F(t) \end{bmatrix} \quad (3-14)$$

Furthermore, the representation of Equation (3-15) for integrated design can still be reduced with the method explained in the previous section. The above relation is reduced by still using the structural perturbation as an input of the system.

$$\tilde{M}_{0,r}\ddot{\eta} + \tilde{D}_{r,0}\dot{\eta} + \tilde{K}_{r,0}\eta = \begin{bmatrix} -\tilde{V}_r^T \sum_{i=1}^n \frac{\partial M}{\partial p_i} \tilde{V}_r \Delta p_i & -\tilde{V}_r^T \sum_{i=1}^n \frac{\partial K}{\partial p_i} \tilde{V}_r \Delta p_i & \tilde{V}_r^T b \end{bmatrix} \begin{bmatrix} \ddot{\eta} \\ \eta \\ F(t) \end{bmatrix} \quad (3-15)$$

However, linear varying the structural perturbations will influence the eigenfrequencies and modeshapes of the system. This influence will be discussed in the next section. Therefore, the needed definitions of eigenfrequency and eigenmode sensitivity are explained in Appendix A.

3-3 Showcase example: mass-spring-damper system

In order to clarify the steps taken for extending a system and to perform structural redesign, a showcase example is given of a mass-spring-damper system. Both [Van Solingen et al. \(2014\)](#) and [Van Herpen et al. \(2014\)](#) give an example of a 2-DoF system in order to explain and verify their extending method. The double mass-spring-damper system is displayed in Figure 3-1 and with the corresponding ODE of Equation (3-6). In this example, it is assumed that the damping can be represented by a viscous damper d , which is a constant value. For the structural model of the OWT a more practical expression for the damping is used, namely the Rayleigh damping. This makes use of a linear combination of the mass and stiffness matrix namely, $D = \alpha K + \beta M$. The advantage of using Rayleigh damping over other methods, is that it has no influence on the modeshapes and the eigensolutions. The eigenfrequencies with corresponding eigenmodes (Figure 3-2) are calculated by solving the eigenvalue problem (Appendix A) and are as follows:

$$\omega_{r,i} = \begin{cases} \omega_{r,1} = 0, & \text{with } \phi_1 = \begin{bmatrix} 1 & 1 \end{bmatrix}^T \\ \omega_{r,2} = \sqrt{\frac{k}{m_1 m_2 / (m_1 + m_2)}}, & \text{with } \phi_2 = \begin{bmatrix} 1 & -1 \end{bmatrix}^T \end{cases} \quad (3-16)$$

From the system description of Equation (3-7), a frequency response of the open-loop system can be made. The bode plot is shown in Figure 3-3 for both the mass positions. However, due

to relative ease of controlling the position of the first mass x_1 , only the second mass position x_2 is considered in this simulation example.

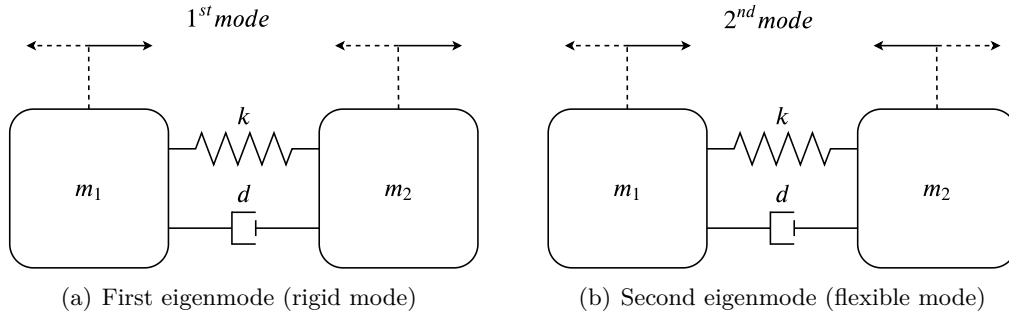


Figure 3-2: Eigenmodes of the double mass-spring-damper system.

It can be seen that changing structural parameters directly influence the eigenfrequency of the system. From a control perspective, the bandwidth ω_b of the system is bounded by the resonance frequency $\omega_{r,2}$ of the system. Implying that the eigenfrequency is high, then the bandwidth of the system is high, as well. This behavior originates from the fact that at the resonance frequency $\omega_{r,2}$ the phase of the open-loop drops -180° , which negatively influences the closed-loop behavior. Thus, the controller structure optimization heavily depends on the change of the eigenfrequency and the corresponding eigenmodes. Therefore, the sensitivities of perturbing a structural parameter on the eigenfrequencies and eigenmodes are determined.

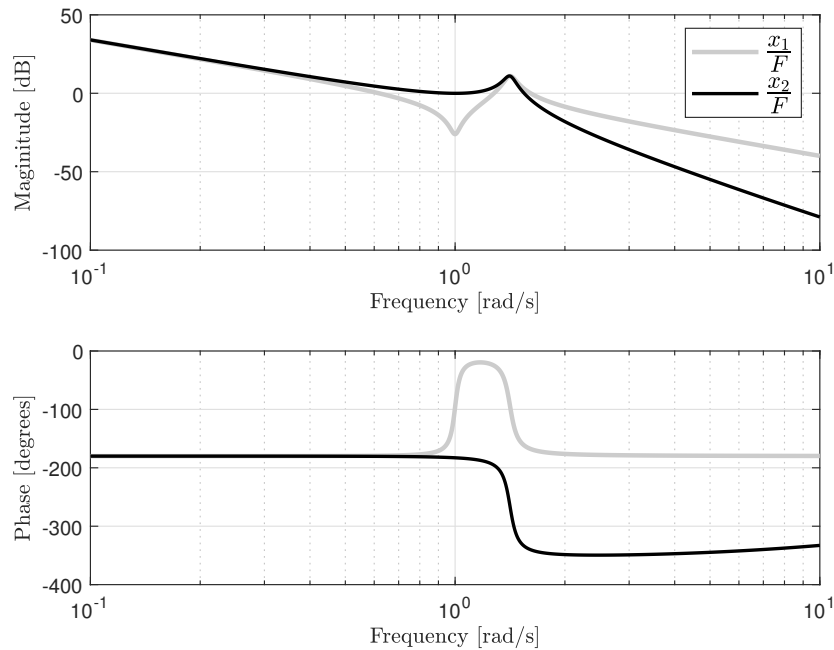


Figure 3-3: Open-loop bode plot for the transfer relation of the position for x_1 and x_2 with as input the applied force F . For $m_1 = m_2 = 1$ and $k = 1$; $d = 0.05$.

Eigenfrequency sensitivity

The method of calculating the eigenfrequency sensitivity is presented in Appendix A and is obtained from the work of [Géradin and Rixen \(2014\)](#). Due to the simplicity of the double mass-spring-damper system the structural parameters are independently varied. The analysis provides insight in the direction and magnitude regarding the system's eigenfrequency will change due to structural adjustments. In this case, there is no physical coupling between mass and stiffness of the system. In contrast to the coupled wind turbine structure in Chapter 4, both the mass and stiffness matrices are characterized by the same structural terms. In Table 3-1, the resulting sensitivities are shown. By looking at the table, the results are the same as the calculated eigenfrequencies of Equation (3-16). Hence, by increasing the stiffness k a higher eigenfrequency will be obtained while increasing the mass the eigenfrequency will drop. Moreover, this inverse behavior can lead to trivial solutions. Due to the infeasibility of the problem and the coupled wind turbine matrices, a coupling for the mass and stiffness parameters should be considered for CSO.

Table 3-1: Sensitivity analysis (k, m_1, m_2) for the first and second eigenfrequency of the double mass spring damper system

Mode i	$\partial\omega_i^2/\partial k$	$\partial\omega_i^2/\partial m_1$	$\partial\omega_i^2/\partial m_2$
$\phi_1 = [0 \ 0]^T$	0	0	0
$\phi_2 = [1 \ -1]^T$	2	-1	-1

Eigenmode sensitivity

One can imagine that when the eigenfrequencies change due to a structural perturbation, the corresponding eigenmodes will change as well. It should be avoided that the fundamental modes change shape, because this violates the assumption of linearly varying structural parameters ([Van der Veen et al., 2017](#)). In order to determine, whether the updated mode-shape shows a significant similarity with the original mode-shape, a measure of comparison is introduced.

First, the sensitivity of the modeshape to a structural change is determined with the work of [Géradin and Rixen \(2014\)](#). The derivation of the method is presented in Appendix A. Secondly, the similarity between the perturbed modeshape and original is checked by using the Modal Assurance Criterion (MAC) of [Pastor et al. \(2012\)](#).

By definition the outcome of the MAC value can only vary between 0 and 1, where 1 implies that updated mode-shape and the initial modeshape are completely similar. In order to perform the assessment, the structural parameter is varied by a coefficient μ with respect to the modeshape sensitivity. The resulting modeshape is added to original modeshape ϕ_c , which gives a new updated modeshape ϕ_{new} using Equation (3-17):

$$\phi_{new} = \mu \frac{\partial\phi}{\partial p_i} + \phi_c \quad (3-17)$$

The resulting modeshape ϕ_{new} is compared with the original modeshape ϕ_c by using the MAC value for several magnitudes of μ . The results are shown in Figure 3-4. From this figure, several things can be concluded. Firstly, only changing the stiffness k will not influence the modeshape. Secondly, solely changing the mass of the system results in slightly different modeshapes. Furthermore, due to the nonlinear relation between changing structural parameters and mode-shapes, it is stated that for high perturbations the original modes are not suitable for approximations (Allemang, 2003). As shown in Figure 3-4, the MAC value of the new modeshapes should stay in a bound of 5% with respect to the original modeshape. In order to avoid modes switching or nonlinear behavior. Hence, based on the results the perturbation in masses should be kept within 40% of the initial mass value.

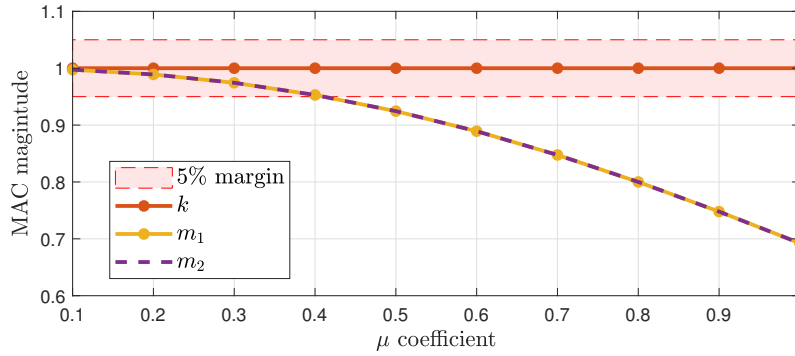


Figure 3-4: Model assurance criterion along linear varying a structural parameter (k, m_1, m_2) by a coefficient μ .

Final routine: Controller-Structure Optimization

The outcome of the structural analysis can be used for the final routine. The system description of Equation (3-6) is extended by using the affinely-dependent parameter framework of Equation (3-15). By using the outcome of the sensitivities of changing parameters the following extended system description is obtained:

$$M\ddot{x} + D\dot{x} + Kx = \begin{bmatrix} \frac{\partial M}{\partial m_1} \Delta m_1 & \frac{\partial M}{\partial m_2} \Delta m_2 & \frac{\partial K}{\partial k} \Delta k & b \end{bmatrix} \begin{bmatrix} \ddot{x} \\ \dot{x} \\ x \\ F(t) \end{bmatrix} \quad (3-18)$$

where the masses (m_1, m_2) and the stiffness (k) are made available for optimization. It can be noticed that the system description is extended from one to four different inputs. From Chapter 2, it is known that the goal is to optimize both the structural and controller parameters in order to obtain better closed-loop performance. The integrated design is based on fixed-structured controller design. Therefore, the controller framework is chosen beforehand and is directly obtained from the work of Van Solingen et al. (2014). The weight function is directly adopted as well and is shown in Equation (3-22). The controller is a PD-controller including a time-delay as:

$$K_{PD}(s) = \frac{K_p + K_d s}{0.01s + 1} \quad (3-19)$$

Furthermore, what is shown in Figure 3-5 is that the input of the controller is the measured position x_2 . The controller output is used as negative feedback relative to the input force F acting on x_1 . In order to show that including the structural parameters is beneficial, two cases are defined with their corresponding weight function W_p :

- Nominal case: in this case no structural alterations are implemented. The case will serve as a benchmark. The perturbations of the plant are excluded by introducing a hard constraint on the perturbation block, namely $\Delta p = 0$. The closed-loop system performance is enforced by a bound on the sensitivity function S by a second-order performance weight where $\beta_p = 0.3$, $M_p = 2$, $A_p = 1 \cdot 10^{-3}$ and $\omega_B = 0.1$.

$$W_p(s) = \frac{s^2/M_p^2 + 2\beta_p\omega_B s + \omega_B^2}{s^2 + 2\beta_p A_p \omega_B s + (A_p \omega_B)^2} \quad (3-22)$$

- Controller structure case: the case allows for structural perturbations. Therefore, the performance weight is slightly adjusted for this case. The adjustment of the performance weight enforces the eigenfrequency to shift. Additionally, the weight is constructed in such a way, that infeasible results are prevented (e.g. parameters going to infinity), adopted from [Van Solingen et al. \(2014\)](#)

$$W_{p,1} = W_p(s) \times \frac{s^2 + 2\beta_p^* A_p^* \omega_B^* s + (A_p^* \omega_B^*)^2}{s^2/(M_p^*)^2 + 2\beta_p^* \omega_B^* s + (\omega_B^*)^2} \quad (3-23)$$

where $\beta_p^* = 0.9$, $M_p^* = 1.9$, $A_p^* = 1.1$ and $\omega_B^* = 1$. These parameters are slightly changed with respect to the work of [Van Solingen et al. \(2014\)](#). The modification can be seen as putting a constraint on the peak of the resonance frequency forcing the system to be altered. Additionally, the value for β_p^* can be iteratively adjusted in order to explore the boundaries of changing the resonance frequency.

Case 1: Nominal case

The nominal case is performed by taking the same routine as [Van Solingen et al. \(2014\)](#). The nominal case gives a good starting point for comparing the results obtained from the CSO case. Furthermore, the system $G_{F \rightarrow x_2}(s)$ is used, implying that the structural properties are not altered. The performance weight W_p is placed as a bound on the sensitivity function in order to impose closed-loop performance. Then, the following norm $\|W_p S\|_\infty$ is minimized by changing the controller parameters K_p and K_d . For the nominal case, reduction methods are not included, due to the simplicity of the problem.

Figure 3-6 shows the open-loop frequency response and the sensitivity function of the system. The resonance peak is clearly visible in both graphs and cannot be shifted by only implementing a controller. The proposed norm reduction gives a satisfactory result of $\|W_p S\|_\infty = 0.873$ with the founded controller parameters $K_p = 0.073$ and $K_d = 0.136$. It is expected that for the next case by including the structural properties, e.g. the masses (m_1, m_2) and stiffness (k), the open-loop frequency response will change.

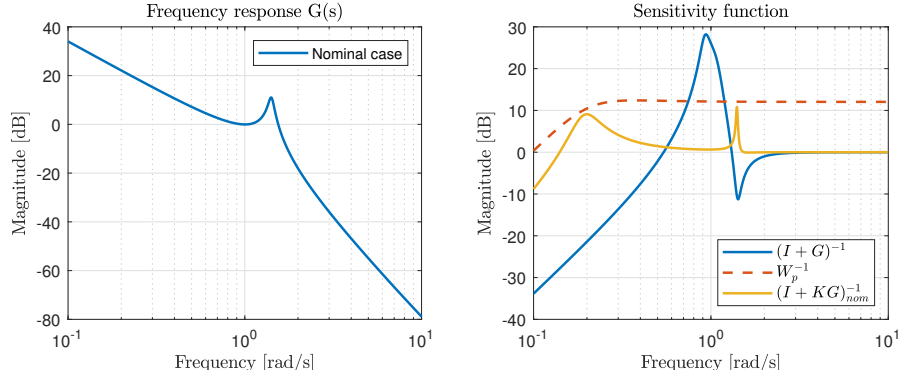


Figure 3-6: The open-loop frequency response of the original system $G(s)_{F \rightarrow x_2}$ (left). The sensitivity function (right) of the optimized controller and the initial sensitivity function (without control). The inverse of the performance weight W_p is shown, as well .

Case 2: Controller structure optimization case

The system is extended by using the description of Equation (3-15) by including the sensitivities for both the masses and stiffness. In order to look to enforce the resonance peak to shift the performance weight of W_p is slightly modified into $W_{p,1}$. This results in a more desired response in frequency domain terms. The design freedom of the structural parameters is determined from the modeshape sensitivity of previous section in order to avoid nonlinear mode switching. The design boundaries are given by $-0.4 \leq \Delta p \leq 0.4$, where $p = [m_1 \ m_2 \ k]$.

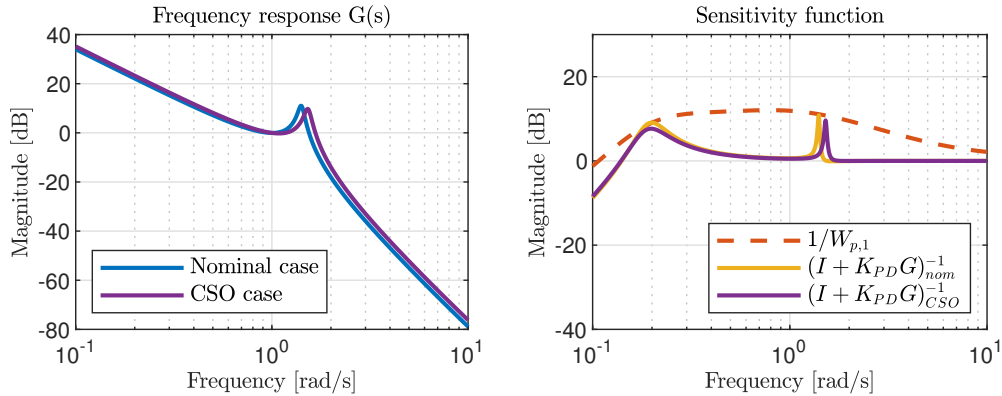


Figure 3-7: The original open-loop frequency response and the updated system (left). The sensitivity function of the controller-structure optimization case and the nominal case (right). The adjusted inverse of the performance weight $W_{p,1}$ is included as well.

The results are shown in Figure 3-7, including the open-loop frequency response of the nominal system and the updated system. Furthermore, from the updated sensitivity function it can be noticed that the frequency peak shifts, from 1.428 [rad/s] to 1.525 [rad/s]. The resonance peak is lowered when the structural parameters are available for optimization as well. This implies that the damping ratio of the system is influenced by changing both the stiffness and mass. Moreover, changing the resonance frequency to more favourable values introduces a problem

on its own. Now, the viscous damping is just a constant and cannot be influenced by control methods. The influence of changing modal damping should be considered when the method is applied on the wind turbine model. By including the structural perturbations the updated system has a closed-loop performance of $\|W_p S\|_\infty = 0.902$. The updated controller parameters are given by $K_p = 0.0613$ and $K_d = 0.1384$. The updated system has the following structural parameters: $m_1^* = 0.64$, $m_2^* = 1.11$ and $k^* = 0.95$. The step response of the implemented controllers for the updated system and the nominal system are shown in Figure 3-8. It can be observed that the CSO case have slightly improved settling time and peak response. The difference is marginal, however it should be noticed that the overall masses are reduced, which is of special interest for the mass minimization of the support structure in Chapter 5.

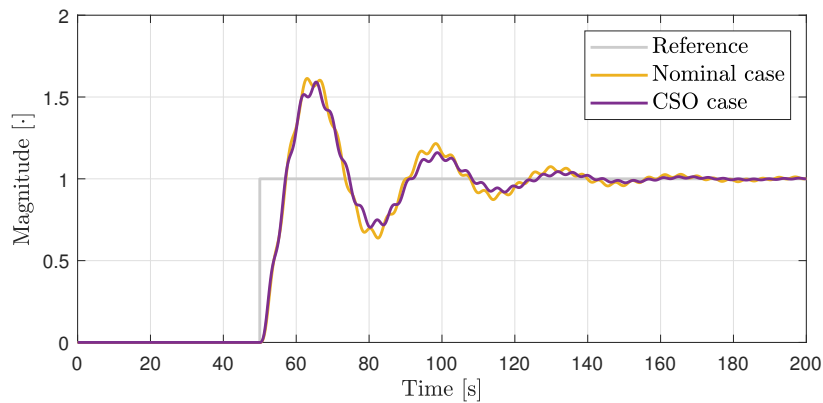


Figure 3-8: Step response of both the nominal case and the CSO case. A slight improvement of the CSO case with respect to the nominal case is noticed.

Hence, the structure and controller can be simultaneously varied, and subsequently, nominal performance is still guaranteed.

Modelling of the OWT

This chapter is dedicated to the modelling of an offshore wind turbine model and will be used for the application of the proposed integral design framework. The developed wind turbine model is based on the work of [Bianchi et al. \(2006\)](#) and the Simplified Low Order Wind turbine (SLOW) of [Sandner et al. \(2012\)](#). A simplified linear wind turbine model is derived and is compared to the more detailed nonlinear model from the in-house aeroelastic code of Siemens Gamesa Renewable Energy (SGRE) called Bonus Horizontal Axis Wind turbine Code (BHAWC).

The model combines an aerodynamic model with a more detailed support structure. The importance for incorporating the aerodynamic model is mainly for the following two reasons. Firstly, the relation between wind and resulting forces and torque on the turbine is captured. This relation allows the implementation of control inputs to alter these parameters. Secondly, additional damping is introduced to the system, which is referred to as aerodynamic damping. The support structure consists of a foundation, tower and soil dynamics, which is coupled with a concentrated mass representing the Rotor Nacelle Assembly (RNA).

A schematic representation of the proposed Offshore Wind Turbine (OWT) model is depicted in Figure 4-1. In this figure, the inputs of the OWT are given by the reference rotor speed $\hat{\Omega}_{ref}$, the wind speed \hat{V}_{wind} and pitch angle $\hat{\beta}$, where the hat "($\hat{\cdot}$)" relates to the variations around the steady-state values. The outputs are the rotor speed $\hat{\Omega}_r$ and the Fore-Aft (FA) acceleration \hat{y}_t at tower top. These outputs are deliberately selected in this way in order to obtain a load reducing controller for above-rated conditions. Furthermore, the aerodynamic model and mechanical model are coupled by the aerodynamic torque \hat{T}_r and thrust \hat{F}_T . The two negative feedback loops, from $\hat{\Omega}_r$ to $\hat{\Omega}_{ref}$ and from \hat{y}_t to \hat{V}_{wind} , are incorporated to capture the nonlinear interaction between the two submodels.

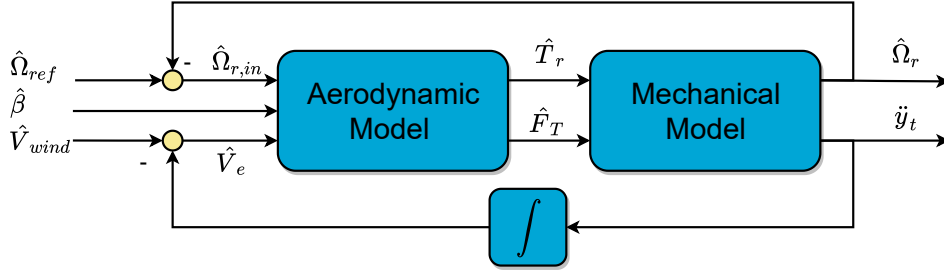


Figure 4-1: A schematic representation of the closed-loop wind turbine model based on Bianchi et al. (2006).

In the following sections, the OWT model of Figure 4-1 is broken up into two sub-models. Section 4-1 covers the aerodynamic model and highlights the interaction between the rotor and the wind. Then, in Section 4-2 the mechanical model is presented. Here, the support structure is described as a parameter dependent state-space model, addressing properties as wall thickness, length and diameter. In Section 4-3 the sub-models will be interconnected and linearized around wind speeds. Finally, the resulting wind turbine model is verified against the high-fidelity non-linear wind turbine model of BHAWC.

4-1 Aerodynamic model

The aerodynamic model is based on the interaction of the wind and the turbine, which results in a rotating rotor. Likewise, the produced torque introduces a thrust force exerted on the Rotor-Nacelle-Assembly (RNA). The input-output behavior of the aerodynamic model is summarized by the schematic representation in Figure 4-2. In this figure, the effective wind speed V_e accounts for the counteracting movement of the tower top velocity with respect to the incoming wind speed as $V_e = V_{wind} - \dot{y}_t$, where \dot{y}_t is the tower top velocity in FA direction. Furthermore, the use of $\hat{\Omega}_{in}$ is the subtraction of $\hat{\Omega}_{r,in} = \hat{\Omega}_{ref} - \hat{\Omega}_r$ as already explained in the introduction. In the following paragraphs these relations are discussed and linearized around different operating points.

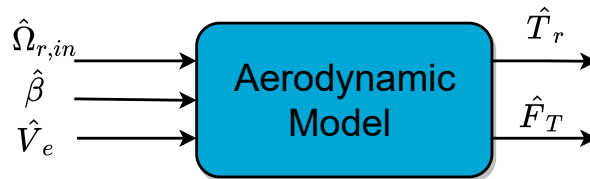


Figure 4-2: A schematic representation of the aerodynamic model inputs and outputs.

Aerodynamic relations and linearization

Usually the aerodynamic relations are expressed in terms of an effective wind speed V_e , the air density ρ , the rotor radius R and the aerodynamic properties of the rotor. The latter is normally described in terms of non-dimensional torque (C_Q) and thrust (C_T) coefficients. These coefficients depend on the tip-speed ratio $\lambda = \frac{\Omega_r R}{V_e}$ and the pitch angle β . Equivalently,

the aerodynamics thrust force and torque are described by Equation (4-1) according to [Bianchi et al. \(2006\)](#):

$$\begin{aligned} F_T &= \frac{1}{2} \rho \pi R^2 C_T(\lambda, \beta) V_e^2 \\ T_r &= \frac{1}{2} \rho \pi R^3 C_Q(\lambda, \beta) V_e^2 \end{aligned} \quad (4-1)$$

There is assumed that the aerodynamic efficiency along each turbine blade is rigid. Additionally, the wind along the blade is distributed equally over the entire swept area of the rotor. Due to the nonlinear behavior of the thrust and torque coefficients and the use effective wind speed, direct implementation unnecessarily complicates the system model. Therefore, a linearization is performed around the operating points of the wind turbine.

The linearization of the above stated aerodynamic equations can be done by a first order Taylor approximation. The aerodynamic thrust and torque are approximated by following expressions:

$$\begin{aligned} \hat{F}_T &= -B_T(\bar{\Omega}_r, \bar{V}_e, \bar{\beta}) \cdot \hat{\Omega}_r + k_{T,V_e}(\bar{\Omega}_r, \bar{V}_e, \bar{\beta}) \cdot \hat{V}_e + K_{T,\beta}(\bar{\Omega}_r, \bar{V}_e, \bar{\beta}) \cdot \hat{\beta} \\ \hat{T}_r &= -B_r(\bar{\Omega}_r, \bar{V}_e, \bar{\beta}) \cdot \hat{\Omega}_r + k_{r,V_e}(\bar{\Omega}_r, \bar{V}_e, \bar{\beta}) \cdot \hat{V}_e + K_{r,\beta}(\bar{\Omega}_r, \bar{V}_e, \bar{\beta}) \cdot \hat{\beta} \end{aligned} \quad (4-2)$$

Where the bar ($\bar{\cdot}$) sign and the hat ($\hat{\cdot}$) sign over the variables, respectively denotes the steady-state (equilibrium) value and the variation around that steady-state value. From the above expression the aerodynamic partial derivatives also referred as sensitivity coefficients are given by:

$$\begin{aligned} B_T(\bar{\Omega}_r, \bar{V}_e, \bar{\beta}) &= \left. \frac{\partial F_T}{\partial \Omega_r} \right|_{(\bar{\Omega}_r, \bar{V}_e, \bar{\beta})} & B_r(\bar{\Omega}_r, \bar{V}_e, \bar{\beta}) &= \left. \frac{\partial T_r}{\partial \Omega_r} \right|_{(\bar{\Omega}_r, \bar{V}_e, \bar{\beta})} \\ k_{T,V_e}(\bar{\Omega}_r, \bar{V}_e, \bar{\beta}) &= \left. \frac{\partial F_T}{\partial V_e} \right|_{(\bar{\Omega}_r, \bar{V}_e, \bar{\beta})} & k_{r,V_e}(\bar{\Omega}_r, \bar{V}_e, \bar{\beta}) &= \left. \frac{\partial T_r}{\partial V_e} \right|_{(\bar{\Omega}_r, \bar{V}_e, \bar{\beta})} \\ k_{T,\beta}(\bar{\Omega}_r, \bar{V}_e, \bar{\beta}) &= \left. \frac{\partial F_T}{\partial \beta} \right|_{(\bar{\Omega}_r, \bar{V}_e, \bar{\beta})} & k_{r,\beta}(\bar{\Omega}_r, \bar{V}_e, \bar{\beta}) &= \left. \frac{\partial T_r}{\partial \beta} \right|_{(\bar{\Omega}_r, \bar{V}_e, \bar{\beta})} \end{aligned} \quad (4-3)$$

The turbine is operating according the operating curve, which is specified in Figure 4-3. The equilibrium values for the pitch angle and rotor speed can be addressed through only the wind speed. This implies that the linearization of the aerodynamic model is described by scheduling around the \bar{V}_e , e.g. $\bar{\Omega}_r(\bar{V}_e)$ and $\bar{\beta}(\bar{V}_e)$ ([Mohammadpour and Scherer, 2012](#)). The scheduling around a wind speed will be used in Section 4-3 for obtaining multiple linear models.

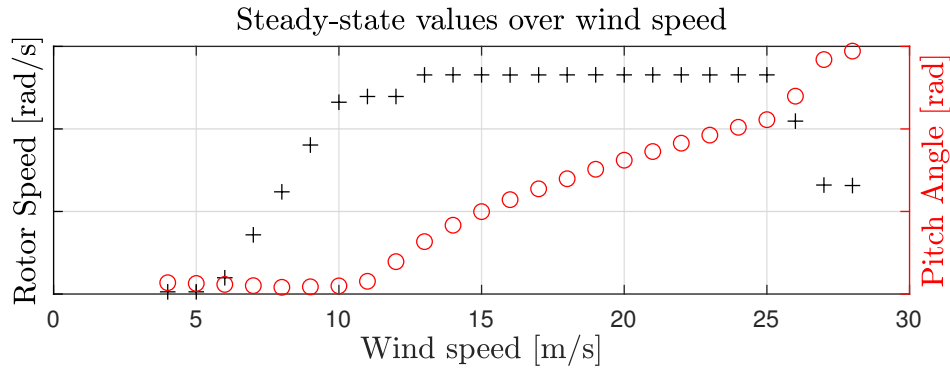


Figure 4-3: Nominal operating trajectory of the 8MW turbine obtained from BHAWC simulations. With the mean rotor speed (+) and the collective pitch angles (o) over increasing wind speeds [m/s]. By the courtesy of SGRE.

From Figure 4-3 the control strategy with respect to the trajectory of rotor speed and pitch angle can be determined. The wind turbine starts operating at the cut-in wind speed of 3 [m/s]. The turbine is shut down at the cut-out wind speed of 28 [m/s] protecting the turbine for high induced aerodynamic loading. The rated wind speed is 12 [m/s]. The cut-in and cut-out wind speeds provide the boundaries of the normal operational region. Between this regions, different control methods are used for increasing the power production and at the same time reducing the loads exerted on the turbine. These so-called control regions are already explained in Chapter 1, but for ease will be repeated with the use of Figure 4-3:

- The region between cut-in and the rated speed. In this region, the turbine is operating in partial-load condition. In order to extract maximum power from the wind, the pitch angle is kept constant at its optimum as shown in Figure 4-3. because of the low wind speeds the rotor speed is below the rated value. Furthermore, the generator torque T_g is used as a control input. By using the generator torque as input, the fluctuations in the drive-train can be mitigated. As a consequence the loads on the drive-train are reduced.
- The region between rated and the cut-out speed. In this region, the turbine uses the pitch angle as control input: by pitching in and out of the wind, the rotor speed is held at the rated level. Furthermore, the turbine operates with a direct-drive configuration, implying that the rotor torque equals the generator torque.

The operating points of the 8.0MW wind turbine are now explained. From the expressions for the aerodynamic model of Equation (4-2), the use of the torque C_Q and force coefficients C_T are mentioned. These analytical expressions are not available for the 8.0MW wind turbine model. Therefore, the thrust and torque magnitude are approximated directly from thrust and torque curves in the following section.

Thrust and torque curves

The aerodynamic model for the 8MW turbine is determined with the help of the in-house aero-elastic code BHAWC, provided by SGRE. From a control perspective, it is preferred to have a linearized state-space model of the wind turbine, where the mechanical and aerodynamic model of the turbine are combined. However, these linearized state-space models cannot be obtained directly from BHAWC. Fortunately, the thrust and torque curves as a function of pitch, rotor speed and wind are available through look-up tables. The dependence on three variables makes visualization of these curves difficult. Therefore, the thrust and torque is linearized around a wind speed of 18 [m/s] and a rotor speed of 1.1 [rad/s]. The resulting curves are shown in Figure 4-4.

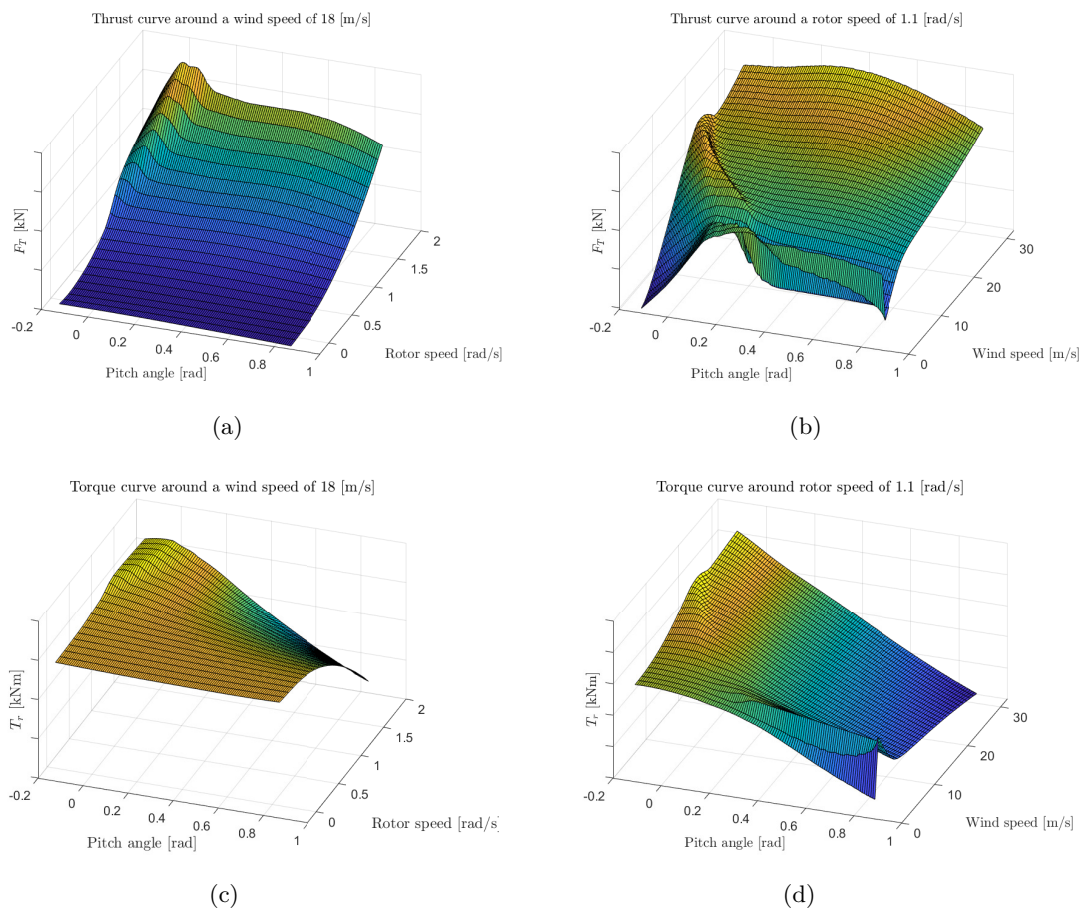


Figure 4-4: Aerodynamic thrust F_T and torque T_r curves of 8.0MW SGRE wind turbine depending on pitch angle, rotor speed and wind speed. The curves are linearized around a wind speed or a rotor speed. The data is obtained from BHAWC. By courtesy of SGRE.

From an analytical point of view, obtaining the C_Q and C_T coefficients for the linearization of Equation (4-2) is preferred. However, these coefficients are only directly usable for torsional-rigid blades. For the 8.0MW SGRE turbine the blades are flap-wise and twist coupled. Therefore, the coefficients become a function of wind speed, pitch and rotor speed. Hence, the

aerodynamic thrust and torque are used directly from simulations. Since these are available in a discrete manner, the aerodynamic gains are determined numerically, using finite difference principles as follows:

$$\begin{aligned}
 B_T(\bar{\Omega}_r, \bar{V}_e, \bar{\beta}) &= \left. \frac{\Delta F_T}{\Delta \Omega_r} \right|_{(\bar{\Omega}_r, \bar{V}_e, \bar{\beta})} & B_r(\bar{\Omega}_r, \bar{V}_e, \bar{\beta}) &= \left. \frac{\Delta T_r}{\Delta \Omega_r} \right|_{(\bar{\Omega}_r, \bar{V}_e, \bar{\beta})} \\
 k_{T,V_e}(\bar{\Omega}_r, \bar{V}_e, \bar{\beta}) &= \left. \frac{\Delta F_T}{\Delta V_e} \right|_{(\bar{\Omega}_r, \bar{V}_e, \bar{\beta})} & k_{r,V_e}(\bar{\Omega}_r, \bar{V}_e, \bar{\beta}) &= \left. \frac{\Delta T_r}{\Delta V_e} \right|_{(\bar{\Omega}_r, \bar{V}_e, \bar{\beta})} \\
 k_{T,\beta}(\bar{\Omega}_r, \bar{V}_e, \bar{\beta}) &= \left. \frac{\Delta F_T}{\Delta \beta} \right|_{(\bar{\Omega}_r, \bar{V}_e, \bar{\beta})} & k_{r,\beta}(\bar{\Omega}_r, \bar{V}_e, \bar{\beta}) &= \left. \frac{\Delta T_r}{\Delta \beta} \right|_{(\bar{\Omega}_r, \bar{V}_e, \bar{\beta})}
 \end{aligned} \tag{4-4}$$

The linearization of the aerodynamic model is performed by using the expression of Equation (4-4). This expression is assumed to be valid when the curves show linear behavior in the applied operating region. The validity is checked by plotting the derived aerodynamic gains with respect to increasing wind speed. The results are shown in Figure 4-5. From these results, it is shown in the region of the above rated wind speeds the aerodynamic gains show no abrupt changes in sign or magnitude. Therefore, it can be concluded that the linearization of the aerodynamic model is valid and, therefore can be used for the wind turbine model.

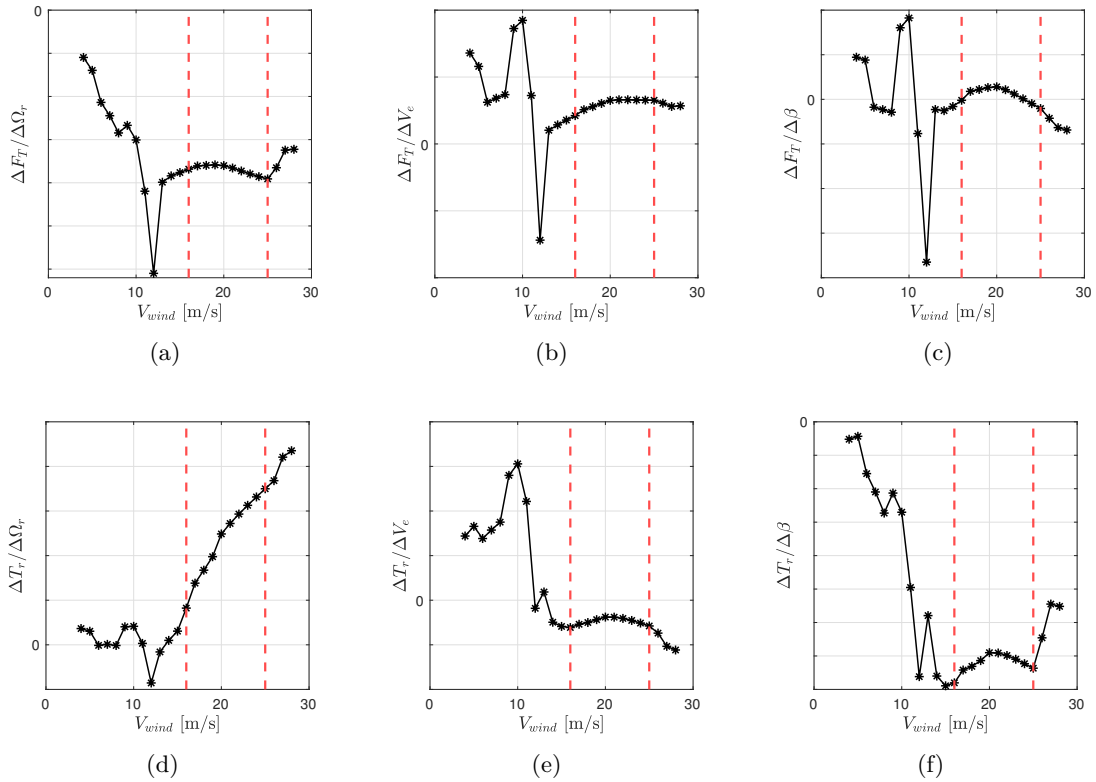


Figure 4-5: Aerodynamic gains of the 8.0MW SGRE turbine. (a) from rotor speed to thrust. (b) from effective wind speed to thrust. (c) from pitch angle to thrust. (d) from rotor speed to torque. (e) from effective wind speed to torque. (f) from pitch angle to torque. The sensitivities of interest are given in the above rated region (---).

4-2 Mechanical model

In this section, the mechanical model will be discussed. The mechanical model consists of the rotor and the support structure. First, the rotor model and the pitch model will be explained, which translates the aerodynamic torque \hat{T}_r to a rotor speed. Thereafter, the support structure is discussed. The support structure is excited by the aerodynamic thrust force \hat{F}_T which causes a Fore-Aft acceleration. Furthermore, the support structure involves coupling of foundation, tower and Rotor Nacelle Assembly. The aerodynamic inputs and resulting output relations for the mechanical model are depicted in Figure 4-6.

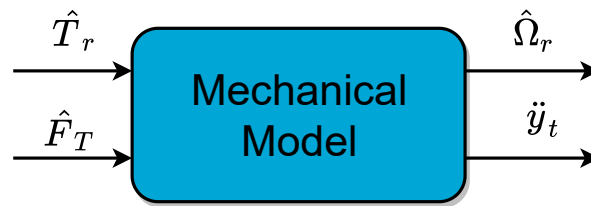


Figure 4-6: A schematic representation of the mechanical model inputs and outputs.

Rotor Model

First of all, it should be mentioned that the physical coupling of the structure and the aerodynamic model is based on the Simplified Low Order Wind turbine model of Sandner et al. (2012). This model introduces the interaction between the wind and the structure. The structure can be described by mass, stiffness and damping terms, which is excited by the aerodynamic thrust force F_T . Furthermore, the aerodynamic torque T_r is working on the rotor of the turbine. These relations can be expressed with the following Ordinary Differential Equations (ODEs):

$$\begin{aligned} \hat{T}_r - \hat{T}_{gen} &= J_r \dot{\Omega}_r \\ M_c \ddot{x}_c + D_c \dot{x}_c + K_c x_c &= b \hat{F}_T \end{aligned} \quad (4-5)$$

where x_c stand for the nodes of the support structure, which will be explained in the upcoming sections. The \hat{T}_{gen} stands for the variation of generator torque. In order to prevent the rotor from abrupt speed changes, the inertia of the rotor J_r is included. The subscript c represents the structural matrices (M_c, D_c, K_c) for the whole support structure, which is assembled in the upcoming sections. Section 4-2 describes a linear mechanical model of the wind turbine and only operates in above-rated wind speeds. In that particular case, it can be assumed that the variation of the generator \hat{T}_{gen} equals zero. Therefore, results in the following expression:

$$\begin{aligned} \hat{T}_r &= J_r \dot{\Omega}_r \\ M_c \ddot{x}_c + D_c \dot{x}_c + K_c x_c &= b \hat{F}_T \end{aligned} \quad (4-6)$$

Pitch mechanism model

When the 8.0MW wind turbine is operating in above rated conditions, only the pitch angle is used as control input. It is chosen to incorporate a pitch actuator model into the wind turbine model. The pitch actuator can be modelled as a first-order time delayed dynamical system (Bianchi et al., 2006). The pitch model is assumed to operate linearly and is expressed as follows:

$$\dot{\beta} = -\frac{1}{\tau}\beta + \frac{1}{\tau}\beta_d \quad (4-7)$$

where β is the pitch angle, β_d the demanded or desired pitch angle and τ is the time delay. The time delay is parameterized as $\tau = 0.3$ [s], which is adopted from 8.0MW BHAWC model of SGRE. For this work, the pitch model of Equation (4-7) is used for control design. However, in reality, the pitch actuation is constrained by saturation levels, maximum pitch angles and rates. For the controller synthesis in Chapter 5, these saturation levels are taken into account through the weight design of the rotor speed controller. For future work, it is interesting to investigate the possibilities of including these dynamic constraints into the control design framework of Chapter 5.

Tower model

The tower section of the 8.0MW turbine is modelled by SGRE using finite element modelling approaches. The elements are connected to form the overall tower structure. These elements can be represented by a thin walled cylinders ($t \ll r$) corresponding to a tower section, where t stands for the wall thickness and r for the radius of an element. From now on the elements are referred as shells. The used tower model of the 8.0MW turbine consists of a total of 40 shells each with varying wall thickness t_i , diameter D_i , as shown in Figure 4-7. The subscript i stands for the position of the shell. The different properties for normal and thin walled cylinders are given in Table 4-1. The structural properties and specifications, e.g. radius and length per shell, are presented in Appendix B.

Table 4-1: Physical properties cylinders and thin walled cylinders ($t \ll r$)

Symbolic expression	Cylinder	Thin walled cylinder
A cross sectional area	$\pi(r_o^2 - r_i^2)$	$2\pi r t$
I_z Second moment of inertia	$\frac{\pi}{4}(r_o^4 - r_i^4)$	$\pi r^3 t$
r_o, r_i Outer and inner radius	r_o, r_i	$r_o \approx r_i$

These shell elements are based on general beam theories like Euler-Bernoulli and Timoshenko, which are widely used by the industry for support structure design (Arany et al., 2015). The main difference between the two theories originates from when the beam is bent by a applied force. When a Timoshenko beam is bent, it allows for a rotation between the cross section and the bending line, which is not the case for the Euler-Bernoulli beam theory. This inclusion of rotation is illustrated in Figure 4-8. It can be seen that the Euler-Bernoulli beam is perpendicular to the bending line.

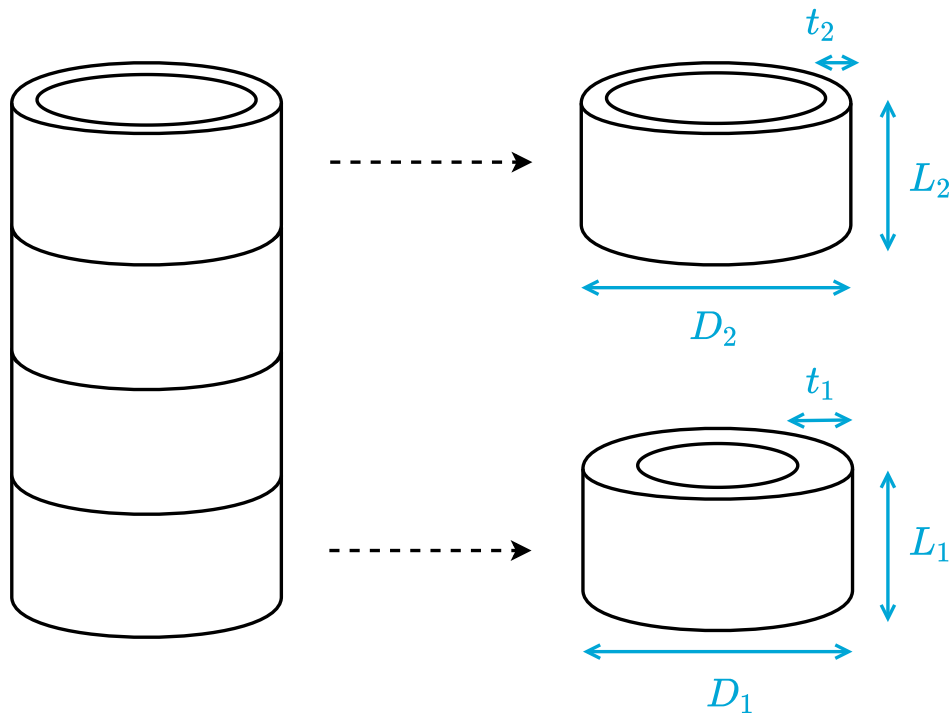


Figure 4-7: The tower consists of a finite number of shells. Each shell can be described by corresponding diameter D_i , length L_i and wall thickness t_i . Where i stands for the number of shells.

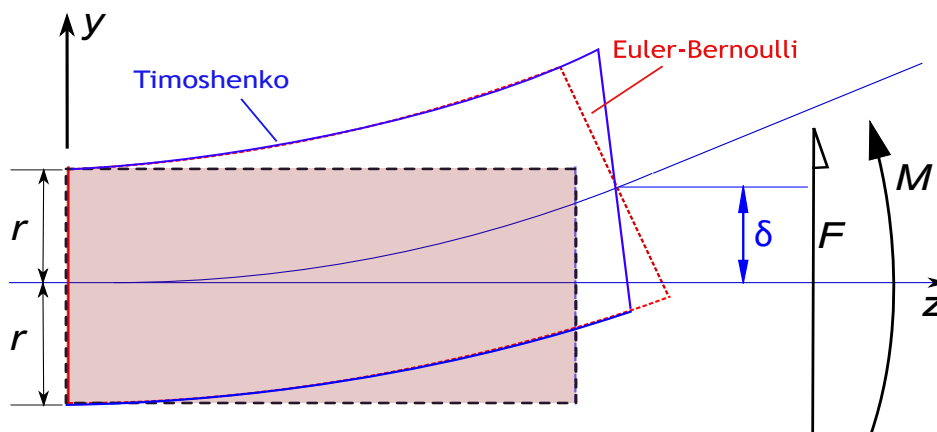


Figure 4-8: Deformation of a Timoshenko beam (blue) compared with an Euler-Bernoulli beam (red) under an applied shear force F and moment M . The total displacement is given by δ .

Therefore, the Euler-Bernoulli beam shows less flexible behavior than the Timoshenko beam. It is chosen to model the tower of the support structure as Euler-Bernoulli beams with 3 Degrees of Freedom (DoF) per node $(u_{y,z}, \theta_y)$. Thus a beam can move in the y - and z -direction and rotate around the y -axis. The reason for modeling the tower with Euler-Bernoulli beams is because the differences between the beam theories are negligible for representing a wind turbine tower (less than 0.1%) (Arany et al., 2016). This can be explained by looking at the

related shear deformation:

$$\phi_y = \frac{12EI_z k_y}{AGL^2} \quad (4-8)$$

This shear component is included for Timoshenko beams and for Euler-Bernoulli beams it is assumed to be zero. As long as the surface area A over length L is large enough, the shear deformation is approximately zero. Furthermore, this can be specified more in the case of the used thin walled cylinders. Namely, using Table 4-1 the expression of Equation (4-8) can be reduced to the ratio of (r^2/L^2) . This ratio implies that for larger length over radius r ($L \gg r$) the use of Euler-Bernoulli over Timoshenko beams is justified. However, this is not the case for each individually element of the tower of the 8.0MW turbine. The main reason that Euler-Bernoulli beams are still used is due to the linear dependency through the wall thickness as shown in Appendix B. This cannot be done for the Timoshenko beams, and therefore is not applicable for the proposed framework of extending the system description as in Chapter 3. The resulting less flexible behavior of the tower model is noticed in Section 4-3, as well. The Euler-Bernoulli beam and the coupling of the elements is briefly discussed below. The theory is obtained by using the notes and work of Panzer et al. (2009); Gavin (2014). Only the resulting structural matrices will be presented. For an extensive overview of the first principles of Euler-Bernoulli beam theory, the work of the aforementioned authors is recommended.

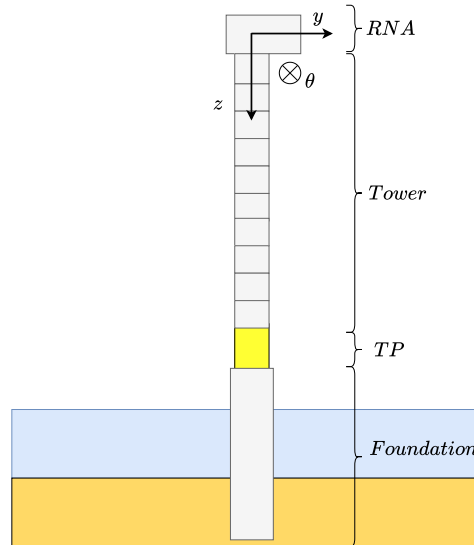


Figure 4-9: Schematic representation of a lumped mass model of the 8.0MW SGRE wind turbine with corresponding coordinates.

The tower model is represented by Figure 4-9, which consists out of a total of 40 shell elements. The total number of elements is provided by the dimension of the tower model, which consisted out of 40 evenly distributed elements. For each single beam element the nodes are defined as $x = [u_{z_1} \ u_{y_1} \ \theta_1 \ u_{z_2} \ u_{y_2} \ \theta_2]^T$. These coordinated are related to the transnational directions in z and y of the turbine model, as shown in Figure 4-9. The formulation of mass and stiffness matrices are presented in Appendix B for Euler-Bernoulli beams. Furthermore, it is shown in Appendix B that for thin walled cylinders, the structural matrices are linearly

dependent on the wall thickness parameter. For ease of notation, the simplified form of the structural matrices are as follows:

$$M = \left[\begin{array}{c|c} M_{11}^e & M_{12}^e \\ \hline M_{21}^e & M_{22}^e \end{array} \right] \quad K = \left[\begin{array}{c|c} K_{11}^e & K_{12}^e \\ \hline K_{21}^e & K_{22}^e \end{array} \right] \quad (4-9)$$

The notation and partitioning of matrices in elements as M_{ij}^e and K_{ij}^e is used for stacking the shell together. Furthermore, the superscript e stands for the number of shell element used in the overall tower structure. The i , and j corresponds to the node positions within each shell element. To be more precise, each shell element is formed by two consecutive nodes within the overall tower structure.

The principle of stacking the multiple shell elements in order to obtain the tower model of the 8.0MW turbine is obtained from [Panzer et al. \(2009\)](#). The primal formulation is given for the sub-structuring technique of coupling structural elements ([Klerk et al., 2008](#)). It makes use of so-called interface nodes and unique nodes. The former are present in both the yet to be coupled element dynamics and the latter as singularities between the coupled element dynamics. In order to explain the coupling of the shell elements, an example of stacking three shell elements is presented. The same partitioning of Equation (B-1) is used. The resulting assembly of the stiffness and mass matrix for three elements is given by:

$$M = \left[\begin{array}{cccc} M_{11}^1 & M_{12}^1 & 0 & 0 \\ M_{21}^1 & M_{22}^1 + M_{11}^2 & M_{12}^2 & 0 \\ 0 & M_{21}^2 & M_{22}^2 + M_{11}^3 & M_{12}^3 \\ 0 & 0 & M_{21}^3 & M_{22}^3 \end{array} \right] \quad K = \left[\begin{array}{cccc} K_{11}^1 & K_{12}^1 & 0 & 0 \\ K_{21}^1 & K_{22}^1 + K_{11}^2 & K_{12}^2 & 0 \\ 0 & K_{21}^2 & K_{22}^2 + K_{11}^3 & K_{12}^3 \\ 0 & 0 & K_{21}^3 & K_{22}^3 \end{array} \right]$$

This stacking principle is executed for the whole tower structure by assembling all 40 elements parameterized for the initial 8.0MW SGRE tower design. For the initial design, the shells are characterized by a different thickness, diameter and length. Furthermore, the parameterization of different beam elements is provided by SGRE. Hence, the resulting mass and stiffness matrices for the tower are given by M_t and K_t .

The Rotor Nacelle Assembly

The RNA of the 8.0MW SGRE turbine is modelled as an equivalent mass with corresponding rotational inertia terms. The properties of the turbine model are stated in Appendix C. The blades are not explicitly taken into account. This work focuses on the first bending modes of the turbine model and the blade dynamics only appear at high frequencies ([Osgood, 2001](#)). The RNA is coupled with the top node of the tower model by adding the RNA mass to the transnational nodes (u_y, u_z) and the parallel axis theorem is needed for describing the rotational node (θ_y). The assumption is made that adding the RNA does not influence the stiffness of the total system. The corresponding mass matrix of the RNA is described as follows:

$$M_{RNA} = \left[\begin{array}{ccc} m_{RNA} & 0 & 0 \\ 0 & m_{RNA} & 0 \\ 0 & 0 & I_{yy} + z_{\Delta cog}^2 m_{RNA} \end{array} \right] \left[\begin{array}{c} u_z \\ u_y \\ \theta_y \end{array} \right] \quad (4-10)$$

where the I_{yy} is the inertial term of the RNA and the $z_{\Delta cog}$ is the offset in center of gravity between the tower and the RNA.

Rayleigh damping

In order to finalize the expression of describing the dynamic behavior of the tower, the structural damping is still missing. The most effective way is to treat the damping as Rayleigh damping for large structural systems:

$$D_t = \alpha_t M_t + \beta_t K_t \quad (4-11)$$

where α_t and β_t are arbitrary constant coefficients. These coefficients weight the tower mass matrix M_t and the tower stiffness matrix K_t , which each contribute to the overall structural damping D_t . The advantage of using Rayleigh damping over other methods, is that it has no influence on the modeshapes and the eigensolutions. By using Rayleigh damping, the calculated response of the structure is greatly simplified (Liu and Gorman, 1995). Furthermore, the derived damping matrix is only applicable for the tower. The resulting damping ratio of the tower is validated against the BHAWC model in the Section 4-3 and it will be concluded that the overall damping of the structure is approximately the same. Since the tower and RNA are discussed, the overall Ordinary Differential Equation (ODE) of the tower is:

$$M_t \ddot{x}_t + D_t \dot{x}_t + K_t x_t = b F_T \quad (4-12)$$

where M_t , D_t and K_t are respectively the resulting tower mass, damping and stiffness matrix. The dimensions of these matrices follow from the total number of coupled shells and the number of DOFs. Therefore, the dimensions of each matrix are given by $N_{DOF}(N_{Shells} + 1) \times N_{DOF}(N_{Shells} + 1)$.

Foundation model

The foundation model for the 8.0MW turbine is provided by SGRE. The model consists of a monopile and a Transition Piece (TP). The assembly of these two is called the foundation structure. The foundation structure is modelled using the same principles as the tower. In addition to the normal structural dynamics, a linear soil model is added, such that soil and structural dynamics are coupled. The linear soil is modelled using linear springs and leads to a contribution of stiffness G_{soil} in the differential equation. The foundation model can be described by the following ODE:

$$M_f \ddot{x} + D_f \dot{x} + (K_f + G_{soil})x = b_f F_{ext}(t) \quad (4-13)$$

In order to couple the foundation with the tower, the aforementioned primal principle of substructuring is used from Klerk et al. (2008). Hence, the coupling of the tower and foundation is done as follows:

$$\underbrace{\begin{bmatrix} M_t & 0 \\ 0 & M_f \end{bmatrix}}_{:=M_c} \underbrace{\begin{bmatrix} \ddot{x}_t \\ \ddot{x}_f \end{bmatrix}}_{\ddot{x}_c} + \underbrace{\begin{bmatrix} D_t & 0 \\ 0 & D_f \end{bmatrix}}_{:=D_c} \underbrace{\begin{bmatrix} \dot{x}_t \\ \dot{x}_f \end{bmatrix}}_{\dot{x}_c} + \underbrace{\begin{bmatrix} K_t & 0 \\ 0 & K_f \end{bmatrix}}_{:=K_c} \underbrace{\begin{bmatrix} x_t \\ x_f \end{bmatrix}}_{x_c} = \underbrace{\begin{bmatrix} b_t \hat{F}_T \\ b_f F_{ext} \end{bmatrix}}_{:=b \hat{F}_t} \quad (4-14)$$

where the subscripts t , f , c stand for respectively the structural matrices of the tower, foundation and coupled model. All the individual parts of the structure are discussed and the structure is only excited by the thrust force of the aerodynamic model. Additionally, the rotor starts

rotating due to applied aerodynamic torque. Hence, by coupling the interface nodes of the tower and foundation, the final ODE of the OWT structure is obtained:

$$M_c \ddot{x}_c + D_c \dot{x}_c + K_c x_c = b \hat{F}_T \quad (4-15)$$

Due to the coupling of the different finite element based structural matrices, the resulting support structure model is described by high-order matrices. These matrices are not preferred in the case of computation time or simulations. Therefore, the resulting structural model is reduced in the following section.

Reduced mechanical model

The modal reduction method presented in Chapter 3 is used for the model reduction of the wind turbine model. The full system model of Equation (4-15) can be reduced by computing the eigenfrequencies and corresponding modeshapes. The frequency response from thrust force F_T to nacelle acceleration \ddot{y}_t is depicted in Figure 4-10. From the frequency response, it is deduced that the first two eigenfrequencies are the most dominate due to the high peak gains and are less damped than the other modes. Therefore, the reduction is done by only selecting the first two eigenmodes of the support structure. The first mode ϕ_1 causes the FA bending motion and the second mode ϕ_2 the is second tower bending mode. The corresponding frequencies are given in Table 4-2. The reduced system is determined by approximating the reduced system response, which is as follows

$$\begin{aligned} x_c(t) &= \begin{bmatrix} \phi_1 & \phi_2 \end{bmatrix} \eta(t) \\ x_c(t) &\approx \tilde{V}_r \eta(t) \end{aligned} \quad (4-16)$$

By using the reduced system response of the tower, the system description of Equation (4-15) is expressed as:

$$\underbrace{\tilde{V}_r^T M_c \tilde{V}_r}_{:=\tilde{M}_r} \ddot{\eta}(t) + \underbrace{\tilde{V}_r^T D_c \tilde{V}_r}_{:=\tilde{D}_r} \dot{\eta}(t) + \underbrace{\tilde{V}_r^T K_c \tilde{V}_r}_{:=\tilde{K}_r} \eta(t) = \underbrace{\tilde{V}_r^T b \hat{F}_T(t)}_{:=\tilde{b}_r} \quad (4-17)$$

The resulting reduced system of the support structure is depicted in Figure 4-10 as well. What can be noticed is that for the frequencies below the chosen two resonance frequencies the curves overlap perfectly. The resonances occurring at higher frequencies at the full scale model do not significantly influence the behavior of the original system response. Hence, the assumption can be made that the reduced model preserves the most predominant dynamics.

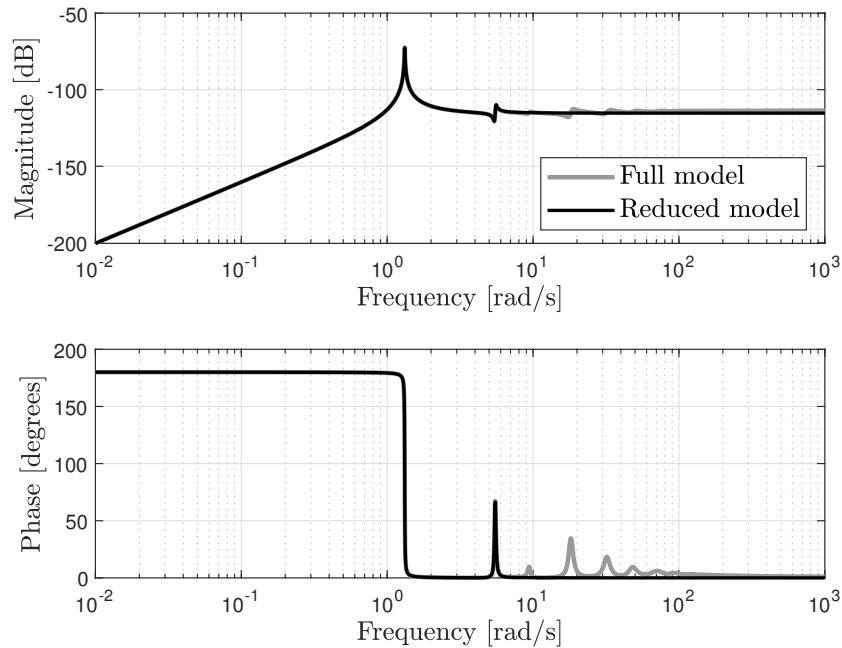


Figure 4-10: Frequency response from thrust force at tower top tower F_T to acceleration \ddot{y}_t for the structural model of the wind turbine. Both the reduced and full model description is depicted.

Since the reduced structural model represents the original structural model reasonably well. Therefore, it is chosen to interconnect the reduced structural model with the linearized aerodynamic model in the next section.

4-3 The complete OWT model

In the introduction of this chapter, the schematic representation of wind turbine model has been discussed shortly. In this section, the aerodynamic model of Section 4-1 and the mechanical model of Section 4-2 are interconnected as depicted Figure 4-1. First, the resulting wind turbine is linearized around the different operating conditions obtaining multiple linear models. These models are evaluated and analysed in the frequency domain. Thereafter, one model of interest is chosen and the resulting behavior is analysed for the aerodynamics and structural dynamics. The latter is done by comparing time domain simulations executed with the BHAWC model and the derived wind turbine model.

Multiple linearized wind turbine models

It is assumed that the turbine is operating in above rated conditions, multiple linear models can be determined by using the steady-state values as depicted in Figure 4-3. As mentioned, the Controller Structure Optimization (CSO) application on the wind turbine will be performed for above rated wind speed as well. Therefore, the aerodynamic model is linearized in a range from the rated wind speed at 16 [m/s] until the cut-out wind speed at 28 [m/s]. In

order to assess the control design from pitch actuation and small deviations of rotor speed, the wind speeds of interest are defined as $V_{wind} \in [16 \ 28]$ [m/s]. The linearized aerodynamic model is coupled with the mechanical model of the wind turbine according to Figure 4-1. Figure 4-11 shows the frequency response of multiple linearized wind turbine systems for two different inputs. The response for each sub-figure will be analysed in more detail next.

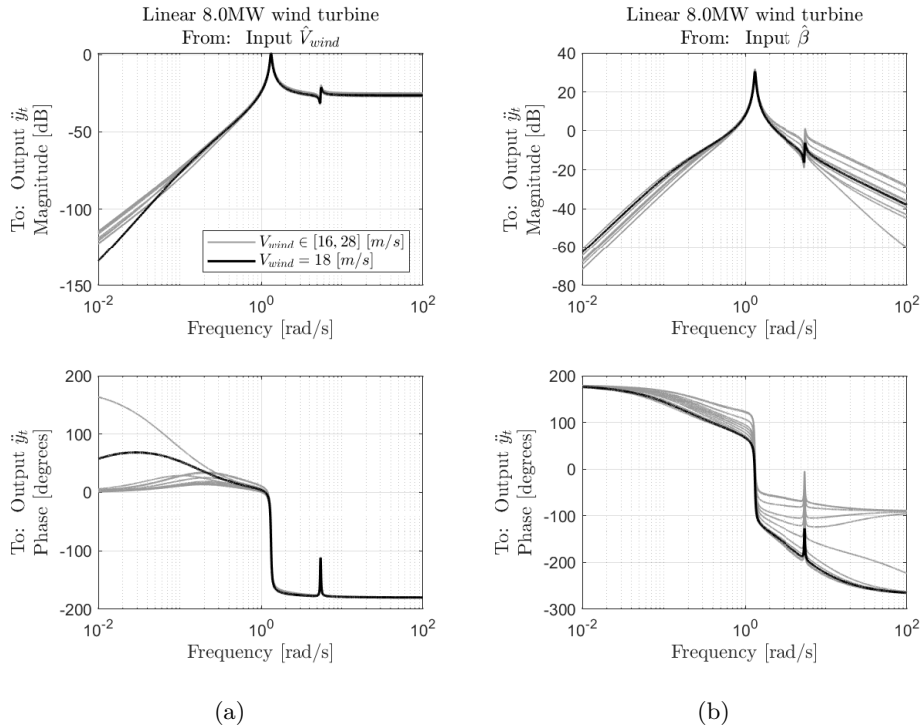


Figure 4-11: Frequency response of multiple wind turbine models linearized around above-rated wind speeds (—). The indicated linear model of interest at 18 [m/s] (—). (a) shows the response from wind V_e to tower top acceleration \hat{y}_t . (b) shows from pitch angle $\hat{\beta}$ to tower top acceleration \hat{y}_t

Figure 4-11a depicts the transfer function from wind speed V_e to tower top acceleration \hat{y}_t . Notice that for low frequencies (<0.1 [rad/s]) small deviations in both magnitude and phase are visible. For higher wind speeds, the magnitude at lower frequencies get higher. As a consequence, the phase at lower frequencies drops for higher wind speeds. Furthermore, the first and second resonance peak do not differ for the different wind speeds. Therefore, it can be concluded that one single linear model is sufficient for describing the entire cut-in and cut-out region from wind speed to rotor speed.

Figure 4-11b shows the transfer function from pitch angle $\hat{\beta}$ to tower top acceleration \hat{y}_t . Looking at graphs, the opposite behavior with respect to Figure 4-11a is noticed. For higher wind speeds, the magnitude drops at low frequencies while the phase increases. Moreover, the height of the resonance peaks fluctuate over different linearized points, where the first resonance peak is of interest for obtaining a load reducing controller. This resonance peak is responsible for the amplification of the FA tower motion. Therefore, the aim is to attenuate

this peak in the transfer function and the procedure achieving this will be presented in Chapter 5. Furthermore, due the slight variation in magnitude for the first resonance peak, the lowest and highest peak should be analysed. Then it can be determined whether the variation significantly influences the magnitude of the tuned controller parameters.

Table 4-2: Damping of the first two modes of the 8.0MW SGRE wind turbine model. For only the mechanical model and for the overall model including the aerodynamic damping.

Frequency ω [rad/s]	Mechanical model		Overall model	
	Pole	Damping ζ	Pole	Damping ζ
1.32	$-0.00461 \pm 1.319i$	0.0035	$-0.0277 \pm 1.32i$	0.021
5.55	$-0.0733 \pm 5.5459i$	0.0132	$-0.0741 \pm 5.5458i$	0.0134

Note that, due to the coupling of the structural model with the aerodynamic models additional damping is added to the modeshapes of the wind turbine system. This additional damping is referred as the aerodynamic damping and originates directly from the interaction of the wind flow with the wind turbine structure. Since, the wind turbine of Figure 4-1 uses the effective wind speed $V_e = V_{wind} - \dot{y}_t$, the aerodynamic damping is taken into account. The ratio between the structural and aerodynamic damping is determined by comparing the frequency response of only the structural model (Figure 4-10) with the overall model (Figure 4-11). When only the structural model is taken into account, the first FA tower mode has a damping ratio of $\zeta_1 = 3.5 \times 10^{-3}$ at the eigenfrequency of $\omega_1 = 1.32$ [rad/s]. The second tower mode has a eigenfrequency of $\omega_2 = 5.55$ [rad/s] and corresponding damping ratio of $\zeta_2 = 1.32 \times 10^{-2}$. The resulting overall model including the additional aerodynamic damping is presented in Table 4-2.

When the system is operating in normal conditions and remains stable, the damping increases on both tower modes. Subsequently, by using the RNA velocity as feedback to the effective wind speed, the damping on both modes increases. It can be seen that the effect of aerodynamic damping is more significant on the first mode then on the second. The damping for the first tower mode increases to $\zeta_1 = 2.1 \times 10^{-2}$, making the overall damping ratio for including the aero-elasticity $\zeta_{structural}/\zeta_{incl.Aero.} \approx 6$.

Behavior of the derived wind turbine

The wind turbine is modelled using in-house specifications of the 8MW SGRE turbine resulting in the derived low-fidelity model. The behavior of the resulting linearized models are evaluated whether the behavior represents the physical turbine. Firstly, the structural behavior of the wind turbine is validated against the high-fidelity 8MW turbine of BHAWC. Thereafter, the system is excited by a step in the pitch angle and the resulting behavior of the rotor speed is analysed.

Resulting structural behavior

To confirm the correctness of the coupled support structure, two verification studies are performed. The verification focuses on exerting the tower top in FA direction with a force F_T . For the validation, the tower is assumed to be clamped. The reason for clamping the tower instead of the foundation originates from the fact that the foundation model is directly obtained from SGRE. By clamping the tower, the structural behavior originates only from the tower model.

For the first analysis, the natural frequency and damping of the tower is obtained from a decay test. The location of the first natural frequency should, at least for the linear model, fit with the nonlinear BHAWC model. The analysis is performed by exerting the tower top with a ramp input F_T , with an amplitude of 1200 [kN] and slope of 12 [kN/s]. After 100 [s] the excitation force is released. This results in a vibration of the support structure in its first eigenmode as visualized in Figure 4-12 for the nonlinear BHAWC model and linear model.

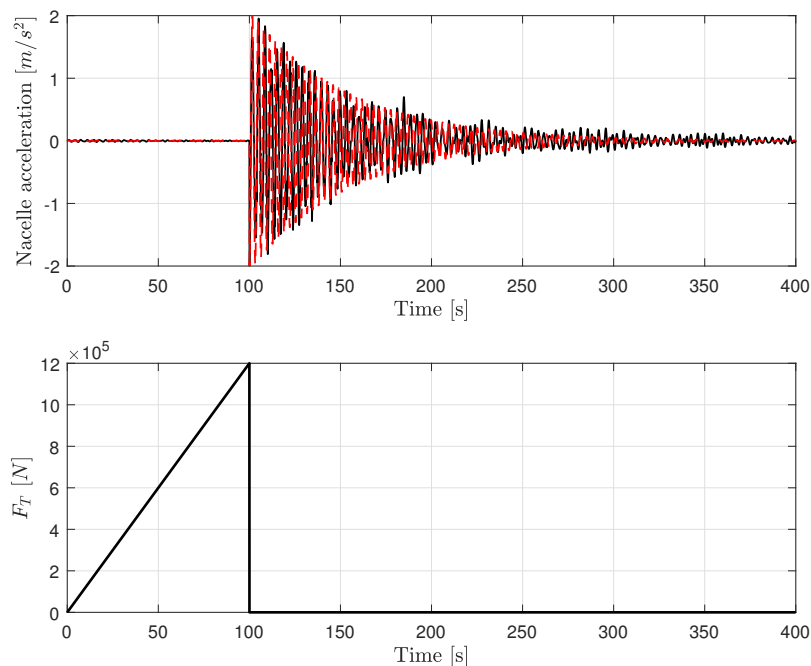


Figure 4-12: Time domain simulation of the tower acceleration (above) excited by temporarily thrust force F_T (below). Response is shown for the high-fidelity BHAWC model (---) and the derived linear wind turbine model (—).

From this figure, the natural frequency and damping is determined by using logarithmic decrements method for free vibrations according to [Inman \(2017\)](#). Using this method for the nonlinear model a damping ratio of $\zeta_{BHAWC} = 0.0081$ is found. For the linear, model a damping of $\zeta_{lin} = 0.0092$ is founded. Furthermore, the first natural frequency is approximately 0.28 [Hz] for the nonlinear model and for the linear model 0.31 [Hz]. The difference is caused by the thin-walled cylinder approach for the Euler-Bernoulli beams making the structure stiffer. Resulting in a slightly higher first natural frequency, this should be taken into account for the controller design whether the first-eigenfrequency forms a driving factor, and subsequently be adjusted for that.

For the second analysis, the tower top is excited to a sinusoidal harmonic force in FA direction. In this case, the force F_T is expressed as:

$$F_T(t) = A \cdot \sin(f(t) \cdot t) \quad (4-18)$$

where A is the amplitude of the periodic force, with a value of 1200 [kN]. Furthermore, the $f(t)$ is a function of varying frequency over time. The varying frequency goes through a region around the first eigenfrequency (f_0) of the turbine. Figure 4-13 depicts the function $f(t)$. It depicts the variation of the frequency between 0.18 [Hz] and 0.22 [Hz] over the total time interval.

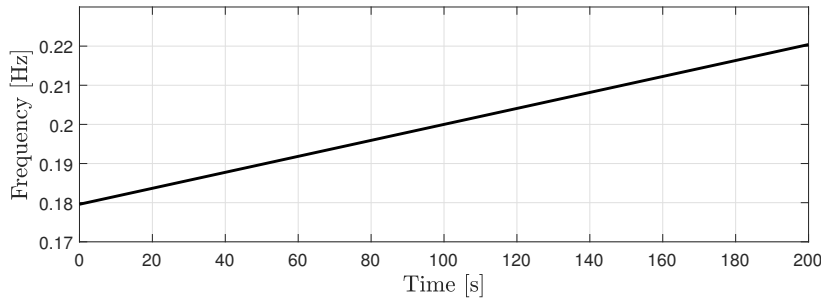


Figure 4-13: Varying frequency $f(t)$ over time for Equation (4-18).

Furthermore, the periodic excitation sweep is applied on the tower top and the resulting response in terms of tower top acceleration is depicted in Figure 4-14. From this figure, it can be deduced that for the first 30 seconds the models differ quite substantially. This originates from the initialization time and the BHAWC model moves in multiple directions (FA and Side-Side (SS)). However, the linear model does not capture this multi-axial movement. After 100 seconds, it can be seen that the behavior of the linear model resembles the response of the BHAWC. This is due to, the most predominant movement becomes then in FA direction. In order to validate the linear model with respect to the high-fidelity BHAWC model, the response of both systems are compared in terms of Variance Accounted For (VAF) ([Verhaegen and Verdult, 2007](#)). The VAF is often used to verify the correctness of the model by comparing the real output (BHAWC) and the estimated output (linear model). In this particular case, the calculated VAF is 61.9%. This is mainly due to the highly nonlinear behavior, which is not captured in the linear model. Hence, the structural behavior of the derived linear model resembles the high-fidelity BHAWC model. As already mentioned the models do not fit perfectly, this originates from the difference in tower eigenfrequency. Furthermore, for the

high-fidelity BHAWC, model gravitational and inertial loadings are taken into account, which results in nonlinear behavior and, subsequently, not a perfect fit in terms of VAF. However, the derived linear wind turbine model shows satisfactory behavior and therefore is suitable for performing a wall thickness reduction.

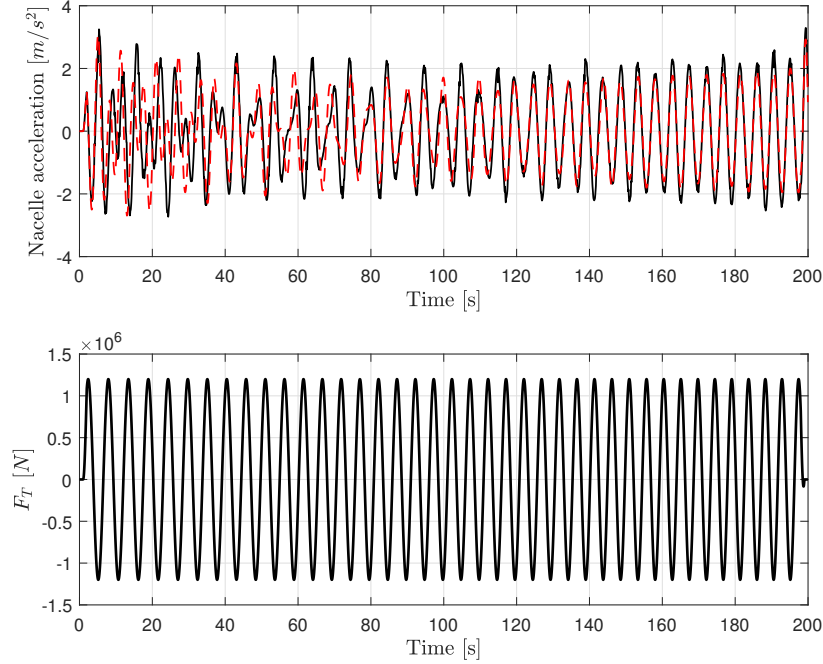


Figure 4-14: Time domain simulation of the tower acceleration (above) excited by a periodic force F_T (below). The periodic force has a frequency of 0.2 [Hz] and variation of 10% over the total duration. Response is shown for the high-fidelity BHAWC model (—) and the derived linear wind turbine model (- - -).

Resulting rotor behavior

For the following analysis, the derived wind turbine model is subjected to a step in the pitch angle under constant operation of $V = 18$ [m/s]. By suddenly changing the pitch angle, the rotor speed will be influenced. Due to the operating conditions, the wind turbine model is linearized around a wind speed of $\bar{V} = 18$ [m/s]. Subsequently, the states of the linear model are in terms of variations around the steady-state operating points. Therefore, for simulation purposes the actual input and output are compensated for in the following manner:

$$\begin{aligned}\beta_{actual} &= \hat{\beta} + \bar{\beta}(\bar{V}) \\ \Omega_{r,actual} &= \hat{\Omega}_r + \bar{\Omega}_r(\bar{V})\end{aligned}\tag{4-19}$$

Furthermore, the resulting response is obtained by only looking at the open-loop transfer function from pitch angle β to rotor speed Ω_r . The reason for only looking at the open-loop response is based on excluding the feedback loops of controllers. Therefore, solely verifying the

rotor dynamics. The resulting behavior of the rotor for a pitch input is shown in Figure 4-15 for the high-fidelity BHAWC model and the derived wind turbine model.

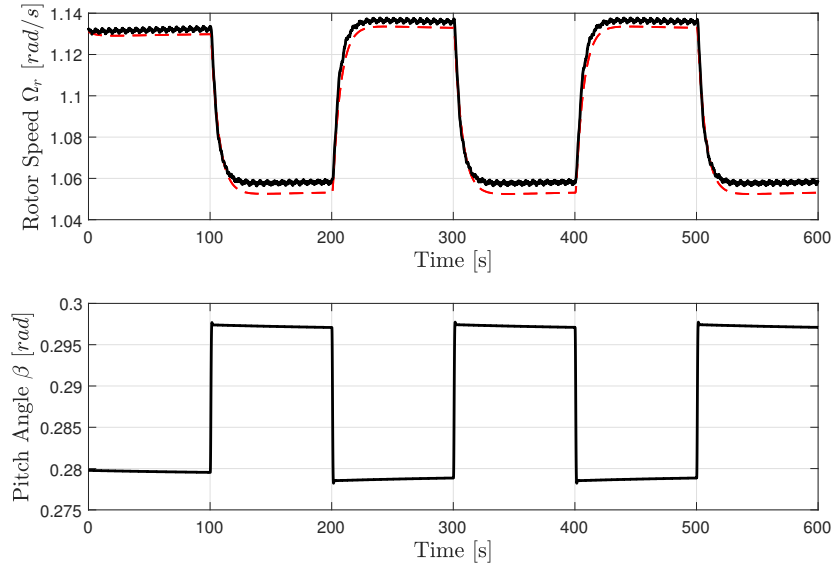


Figure 4-15: Open-loop step response for the pitch angle β as applied input (below). The resulting rotor speed response of the high-fidelity BHAWC model (—) and the derived linear wind turbine model (---) are shown (above).

What can be noticed is the critical damped response for both models. This implies that control methods are needed for mitigating the over-damped rotor deviations. Figure 4-16 shows the relative error between the two simulated models. The trajectory of the error shows a steady-state offset. This is due to the linearization of the linear model in steps of 1 [m/s] and the high-fidelity model has more steady-state operating points. Moreover, it should be mentioned that this validation only works in the above rated regime, due to the fact that the variation of generator torque is assumed to be equal to zero.

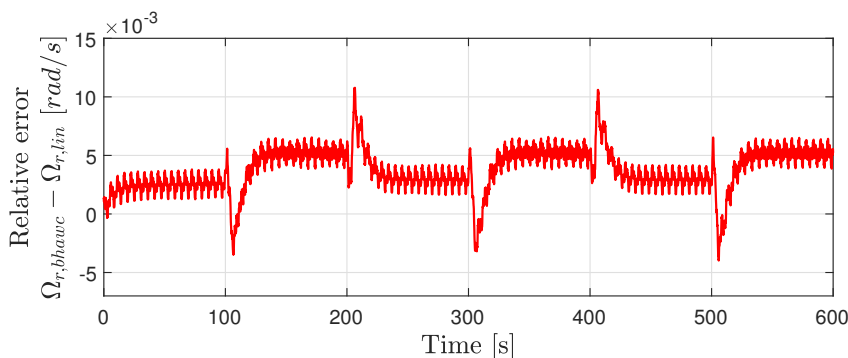


Figure 4-16: Relative error between the response of BHAWC model and the derived linear model for rotor speed

4-4 Summary

The goal of this chapter was to derive a suitable wind turbine model for integral support structure and controller design. Therefore, the goal is twofold. Firstly, the most important dynamics of the 8.0MW SGRE offshore wind turbine should be captured by the derived linear model. Secondly, the possibility of extracting structural parameters for the support structure should be included. Therefore, the modelling approach makes use of characteristics of the real 8.0MW SGRE turbine. This is done by using the aerodynamic thrust and torque curves of the real turbine. Further, the mechanical model is modeled by using a finite element based approach. Thereby, the real dimensions of the support structure are implemented

After coupling the overall structure, the resulting matrices are of high order. Therefore, the original derived model is reduced by only selecting the most dominant modes. In the case of this thesis, the first two modes are selected. The reason for this is that they cause the FA motion, which is to be suppressed in the following chapter. It is shown that the structure is well described by the reduced model approach presented in this chapter.

Referring to the support structure, it is shown that the wall thickness can describe the mass and stiffness matrix linearly for the tower section. By doing so, the wall thickness can be available as structural perturbation. In the next chapter, it is shown that the wall thickness can be changed by using the aforementioned eigenfrequency and eigenmode of Chapter 3 sensitivities.

The resulting wind turbine model represents the 8.0MW SGRE turbine by combining the aerodynamic and mechanical model. The resulting behavior of the derived model is verified by performing time domain simulation. The model shows similar behavior as the high-fidelity BHAWC model. Therefore, the derived model is well-suited for control design purposes. Moreover, due to the linear structural dependency, the model is applicable for the CSO in the next chapter.

Preliminaries for the CSO

Everything up to this point has focused on analysing and obtaining a suitable wind turbine model for the integral support structure and controller design framework. The next step is to formalize the different \mathcal{H}_∞ control design problems. The formalization heavily depends on the subject of the different controller or structural objectives. Therefore, the main goal of this chapter is:

"Provide a framework for simultaneous structured controller design and tunable plant optimization through frequency-based optimization"

For the attentive reader, this goal is adopted from one of the subgoals stated in Chapter 1. The 8.0MW wind turbine model presented in the previous chapter is used to formalize the framework for Controller Structure Optimization (CSO). The framework makes use of the frequency-domain optimization, which involves the multi-variable \mathcal{H}_∞ control design framework as presented in Chapter 2 and Chapter 3. In order to map the design space of simultaneous controller structure optimization different design cases are presented in this chapter. The complete overview of the structure of this chapter is given by the flowchart of Figure 5-1. It provides an insight in the controller design scheme. The actual controller calculations are done in Chapter 6.

The chapter is built up according to the flowchart. Firstly, the controller design objectives are presented in Section 5-1. Furthermore, it tackles the objectives with an initial control design for the Rotor Speed Controller (RSC) and Active Tower Damper (ATD). Subsequently, in Section 5-2, the wind turbine model is extended with additional inputs to the system description involving the eigenfrequency sensitivity of different tower sections. From the controller and structural objectives, different design cases are formalized, which in consecutive order is subjected to one additional formulated objective. In Section 5-3, these different design cases are presented, where three different generalized plants are formulated with the corresponding derivation of the weighting functions. Finally, the chapter is summarized in Section 5-4.

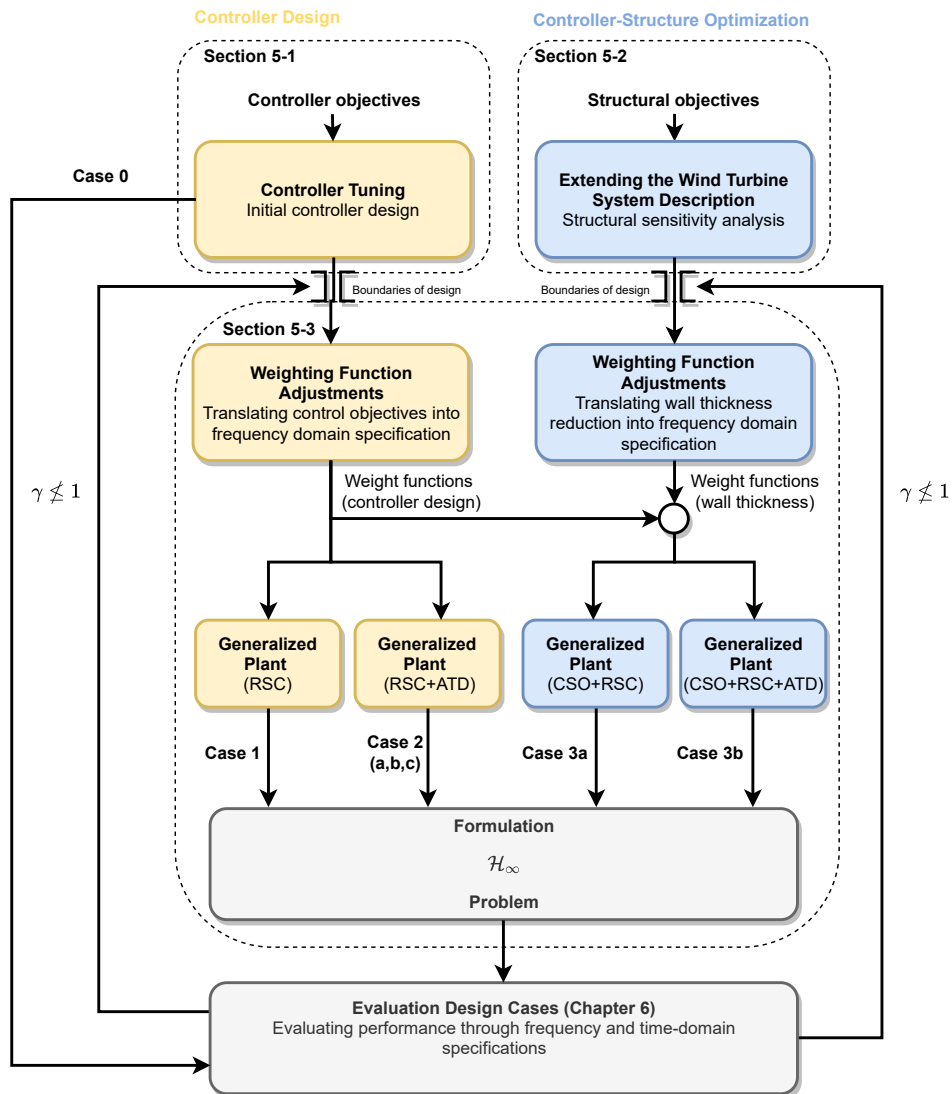


Figure 5-1: Flowchart of the structure of Chapter 5. The yellow boxes are the controller design involving the design of the RSC and ATD. In blue the CSO including the wall thickness perturbations. The resulting design cases are depicted as well. Furthermore, the resulting performance index γ is a measure for ensuring nominal performance $\gamma < 1$.

5-1 Controller design

In this section, the control design is presented by designing an RSC that provides rotor speed control while the Fore-Aft (FA) tower oscillations are mitigated. First, the controller objectives are itemized. Then, an initial controller design is presented in order to meet these requirements.

The controller objectives

As stated in Chapter 2, the goal of the designed controller is to have adequate fast response of minimizing the rotor deviations. Therefore, the designed controller should have the capability of tracking the reference rotor speed. Due to the fact that the turbine is operating in above-rated conditions, the reference rotor speed equals the rated speed. This makes the objective a speed tracking problem for which regular PI-controllers are suitable according to [Shan \(2018\)](#). The 8.0MW turbine allows for quick adjustments of the pitch angle of the rotor blades. The possibility to quickly influence the aerodynamic thrust force acting on the blades allows for additional pitch control objectives concerning fatigue load reduction. In this case, this can be achieved through active damping of the FA tower top accelerations. Since the fatigue of the tower is driving for above-rated wind speeds. As a consequence, it is interesting to incorporate this as an objective for the designed controller [Leithead and Dominguez \(2006\)](#). The designed controller is designed for the full-load region. The control problem regards a disturbance rejection problem. The controller objectives can be summarized in the following general way:

- Rotor speed error: the designed controller should minimize the rotor speed error $\Delta\Omega_r$ between the reference rotor speed $\Omega_{r,ref}$ and the output rotor speed $\hat{\Omega}_r$. This implies that the $\Delta\Omega_r$ should be as small as possible. Furthermore, the bandwidth of the RSC is in principle limited to frequencies well below the first eigenfrequency of the turbine. Additionally, the maximum achievable bandwidth is restricted by the pitch system limitations and time-delay.
- Active tower damping: in order to reduce the tower fatigue loads, the FA tower top acceleration \ddot{y}_t should be minimized by actively increasing the damping at the first tower bending mode. The active tower damping should only be active in the region of the first tower bending mode, otherwise it influences the performance of the rotor speed controller.
- Limited conditions: the limits of the pitch actuators should be taken into account, e.g. maximum pitch speed and accelerations, when applicable.

With the controller objectives mentioned, an initial control design framework can be proposed. In the next section, this initial control design is presented, which takes the aforementioned objectives into account.

Initial controller design

The initial control design is based on the work of [Perrone and Kühn \(2015\)](#). The controller framework is represented by Figure 5-2, which addresses the controller objectives. From Figure 5-2, it can be seen that the centralized feedback is responsible for the rotor speed control, which uses the collective pitch angle β . The output is the measured rotor speed variation $\hat{\Omega}_r$ which is fed through and subtracted by the reference rotor speed $\Omega_{r,ref}$. For this case, the reference rotor speed equals zero, due to the use of the variation around the steady-state value.

Furthermore, the controller combines a decentralized feedback loop, employing the tower top

accelerations \ddot{y}_t as a measured signal. The output of this feedback loop will be represented as an additional collective pitch angle input $\delta\beta$ in order to mitigate the \ddot{y}_t . The actuation is additional to the standard collective pitch action of the rotor speed controller (Bossanyi, 2000). First, the initial controller design for the rotor speed controller is discussed. After that, the tower control loop is presented.

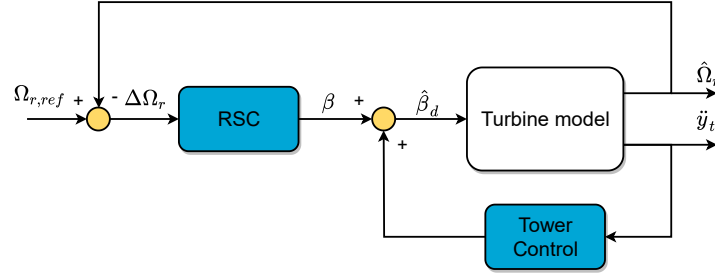


Figure 5-2: Rotor Speed Controller combined with Active Tower Damping. The inner-loop is responsible for the cancellation of the first tower bending mode. The outer-loop is responsible for the rotor tracking of the reference rotor speed $\Omega_{r,ref}$, which is, in this case, equals to zero.

Initial Rotor Speed Controller

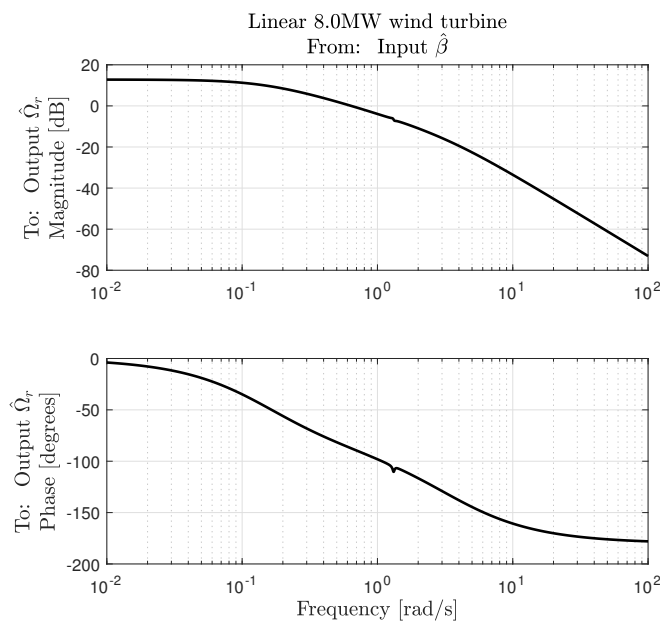
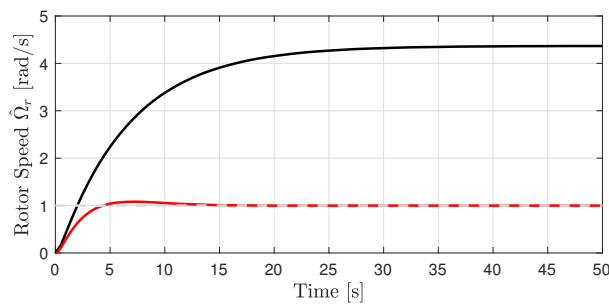
The goal of the controller is to guarantee adequate rotor speed track performance and have a fast response. In order to track the rotor speed, the frequency response of the desired pitch angle β of the rotor speed variations $\hat{\Omega}_r$, as shown in Figure 5-3, is of interest. The shape of the frequency response can be explained from the Open-Loop (OL) poles and zeros stated in Table 5-1. First, the phase drop of -90 [degrees] is caused by the first pole. After that an additional -180 [degrees] drop due to the pole pair at the first eigenfrequency of the structure ($\Omega_1 = 1.33$ [rad/s]). Normally, this pole pair will result in a resonance peak, which limits the controller design. However, a zero pair is located near the first eigenfrequency, the -180 [degrees] is counter-effected by the 180 [degrees] introduced by this zero pair. This explains the small sudden peak behavior in the magnitude plot at 1.33 [rad/s] as shown in Figure 5-3. Still, it should be mentioned that, for the real system the distance between these poles and zeros can be larger. Resulting in a frequency response which is restricted by the first tower mode.

Furthermore, it can be noticed that the Closed-Loop (CL) system remains stable due to the phase not crossing the -180 [degrees] and there is a phase margin of 92.6 [degrees] at the crossover frequency of $\omega_c = 0.64$ [rad/s]. The controller chosen for achieving higher performance and tackles the objective is a PI-controller as Equation (5-1). The PI-controller is capable of a fast response to a disturbance on the system response. It corrects the trajectory when it wants to drift off due to an applied disturbance. The controller design is performed by applying a step response on the reference signal and looking at the CL response. Figure 5-4 shows the resulting step response for which the PI-controller is parameterized with $K_{p,in} = 0.67$ and the $K_{i,in} = 0.19$, which originates from the original Bonus Horizontal Axis Wind turbine Code (BHAWC) rotor speed controller.

$$K_{CPC}(s) = \frac{K_{p,in}s + K_{i,in}}{s} \quad (5-1)$$

Table 5-1: Locations of the OL poles and zeros for the subsystem $G_{\hat{\beta} \rightarrow \hat{\Omega}_r}$.

OL poles	Frequency [rad/s]	OL zeros	Frequency [rad/s]
-0.153	0.153	$-0.0271 \pm 1.32i$	1.33
$-0.0274 \pm 1.31i$	1.33		
-3.33	3.33	$-0.0741 \pm 5.55i$	5.55
$-0.0741 \pm 5.55i$	5.55		

**Figure 5-3:** Open-loop frequency response of subsystem $G_{\hat{\beta} \rightarrow \hat{\Omega}_r}$ from the variation in pitch angle $\hat{\beta}$ as input to the variation of the rotor speed $\hat{\Omega}_r$ as output.**Figure 5-4:** Time domain simulation of applying a step input on the CL subsystem $G_{CL, \hat{\beta} \rightarrow \hat{\Omega}_r}$ without control (—) and with control (—).

Initial Active Tower Damper

The proposed tower control algorithm arises from the dynamic behavior of the support structure. For simplicity the model be recasted to a single Degrees of Freedom (DoF) system. The dynamics in FA direction of the tower top can be approximated by:

$$M\ddot{y}_t + D\dot{y}_t + Ky_t = F_T + \delta F_T \quad (5-2)$$

where y_t represents the displacement in the longitudinal direction, F_T is the thrust force exerted by the wind and δF_T stands for an additional thrust action caused by the pitch actuation. In principle, the additional thrust action is proportional to the first time derivative of the tower top. Therefore, it is possible to magnify the damping of the overall system by introducing an additional driven pitch action as follows:

$$\delta F_T = -D_p \dot{y}_t = \left(\frac{\delta F_T}{\delta \beta} \right) \delta \beta \quad (5-3)$$

$$\delta \beta = - \underbrace{\frac{D_p}{\delta F_T / \delta \beta}}_{=K_{D_p}} \dot{y}_t \quad (5-4)$$

where $\delta \beta$ is the additional pitch actuator and D_p is the additional damping. The additional damping can be included by using the velocity of the tower top \dot{y}_t as measurement. Due to the interaction with the RSC and preventing unwanted feedback of other terms, a band-pass filter G_{bf} centered at the first natural frequency is included in the feedback loop.

$$G_{bf}(s) = \frac{2\zeta\omega_n s}{s^2 + 2\zeta\omega_n s + \omega_n^2} \quad (5-5)$$

where $\zeta = 0.8$ and ω_n is set on the first tower bending frequency. In practice, there is an uncertainty of the first tower frequency of $\pm 10\%$ making the use of a band-filter not that attractive. However, from online tower accelerations measurements, the natural frequency can be estimated, and subsequently, the band-pass filter can be adapted for that measured frequency as in the work of [Pascu et al. \(2017\)](#). The frequency response of the OL subsystem $G_{\hat{\beta} \rightarrow \ddot{y}_t}$ is depicted in Figure 5-5. Moreover, the CL subsystem is shown as well for $K_{D_p} = -0.25$. What is noticed is that the introduction of a control function considerably dampens the peak relative to the first tower bending mode in FA direction.

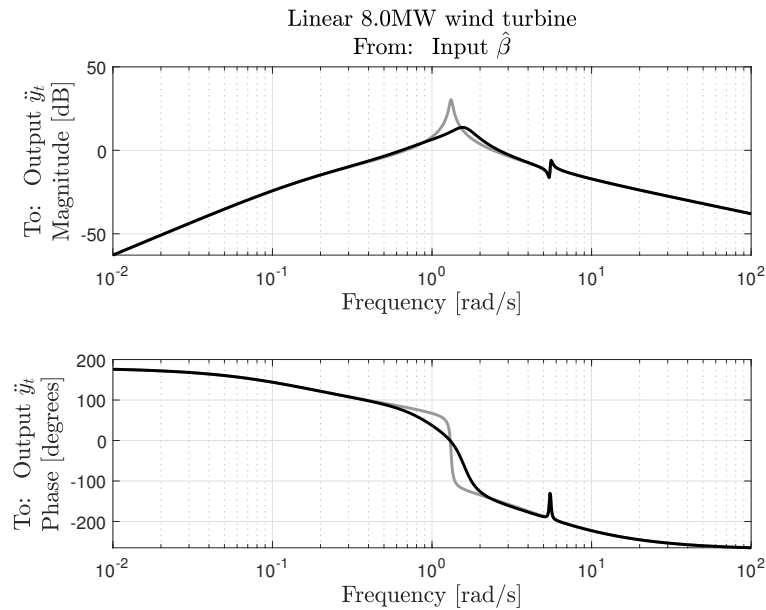


Figure 5-5: Frequency response of both the magnitude and phase for the initial tower control loop: Open-loop (—) versus the closed-loop (—).

Figure 5-6 demonstrates how the initial tower feedback control performs under excitement by a step response. This technique dampens the tower accelerations for the initial open-loop response, which leads to reducing the loads on the structure. Furthermore, the CL system has a settling time of 16.5 [s] and initially, the OL system has a settling time of 143 [s]. The only drawback of this method is the additional pitch activity according to [Bossanyi \(2000\)](#).

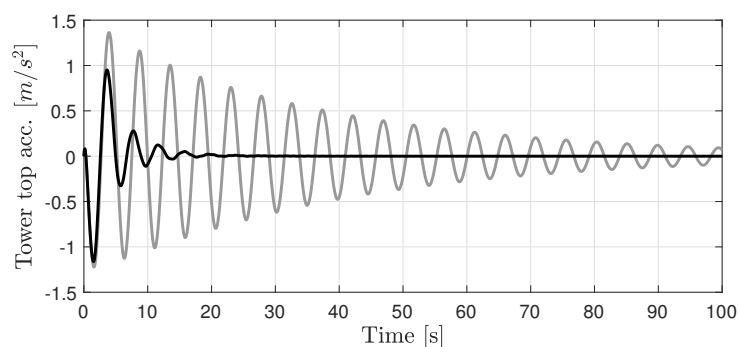


Figure 5-6: Step response of an additional pitch actuation to tower acceleration. The open-loop (—) and the effect of including tower feedback control (—).

With the initial control design and the controller objectives explained, the next step is to evaluate the structural design and extend the system description of the wind turbine model.

5-2 Structural design

The controller objectives are summed up in the previous section. The next step is to tackle the main objective of this thesis, namely the CSO application on the wind turbine model. The goal of including the structural part is to reduce the wall thickness of the support structure. Therefore, the structural objective can be seen as a mass minimization by reducing the wall thickness. The proposed integral support structure and controller procedure makes use of an extended wind turbine model, which is presented in the next section. By doing so, the RSC can be adjusted with the wall thickness of the support structure simultaneously. After that, the eigenfrequency and sensitivity are determined, which form the basis for the structural design part.

Extending the system description

The extension method is based on the sensitivity of perturbing structural parameters, resulting in a change of the eigenfrequency of the system. The extension is done through the same working principles, as the method explained in Chapter 3. Therefore, the mechanical model of the wind turbine model can be extended as follows:

$$M\ddot{x} + D\dot{x} + Kx = \begin{bmatrix} -\sum_{n=1}^{t_N} \frac{\partial M}{\partial t_n} \Delta t_n & -\sum_{n=1}^{t_N} \frac{\partial K}{\partial t_n} \Delta t_n & \tilde{V}_r b \end{bmatrix} \begin{bmatrix} \ddot{x} \\ x \\ F_T(t) \end{bmatrix} \quad (5-6)$$

Recall, that for the overall mechanical model a reduced description is used, as presented in Chapter 4, and for ease is repeated here below:

$$\underbrace{\tilde{V}_r^T M_c \tilde{V}_r}_{:=\tilde{M}_r} \ddot{\eta}(t) + \underbrace{\tilde{V}_r^T D_c \tilde{V}_r}_{:=\tilde{D}_r} \dot{\eta}(t) + \underbrace{\tilde{V}_r^T K_c \tilde{V}_r}_{:=\tilde{K}_r} \eta(t) = \underbrace{\tilde{V}_r^T b}_{:=\tilde{b}_r} \hat{F}_T(t) \quad (5-7)$$

Therefore, the expression of Equation (5-6) is recasted into:

$$\tilde{M}_r \ddot{\eta} + \tilde{D}_r \dot{\eta} + \tilde{K}_r \eta = \begin{bmatrix} -\sum_{n=1}^{t_N} \tilde{V}_r^T \frac{\partial M}{\partial t_n} \tilde{V}_r \Delta t_n & -\sum_{n=1}^{t_N} \tilde{V}_r^T \frac{\partial K}{\partial t_n} \tilde{V}_r \Delta t_n & b \end{bmatrix} \begin{bmatrix} \ddot{\eta} \\ \eta \\ F_T(t) \end{bmatrix} \quad (5-8)$$

Through the above expression, the elements of the tower section are individually accessible for the structural optimization. However, it is desired to have an overall wall thickness reduction. Therefore, the tower elements are bundled together. By reducing the wall thickness the overall pole and zero locations of the system will change. In order to bundle the correct number or positions of the tower elements, the eigenfrequency sensitivity of all tower elements is determined in the next section.

Eigenfrequency sensitivity for different tower sections

The wall thickness perturbation of the tower section is performed by using the preceding eigenvalue sensitivity. The theory is presented in Appendix A. Through this method, the sensitivity of changing the wall thickness for the first two eigenvalues of the support structure are determined. These eigenvalues correspond to the structural modes, which are present in the reduced model as well. Recall from the mechanical model in Section 4-2, that the eigenvalues of interest are given by $s \in [\omega_{1st} \ \omega_{2nd}]^T$. Subsequently, the tower model consist out of a total of 40 elements and corresponding wall thickness per element is given by $t_n = [1, 2, \dots, N_{Tower}]$ where $N_{Tower} = 40$.

For every tower element, the corresponding mass and stiffness matrices are differentiated from the wall thickness parameter t_n . The derivatives are computed element-wise for each element n . These matrices are given by $M_{\Delta t}$ and $K_{\Delta t}$. The elements are expressed linearly through the wall thickness as Equation (B-1) and Equation (B-2). As a consequence, the derivatives can be reduced as follows:

$$M_{\Delta t} = \frac{\partial M}{\partial t_n} = \frac{M}{t_n} \quad K_{\Delta t} = \frac{\partial K}{\partial t_n} = \frac{K}{t_n} \quad (5-9)$$

The next step is to compute the sensitivity of changing the wall thickness t_n per tower element for the two eigenvalues. The expression for the eigenfrequency sensitivity is given by:

$$\frac{\partial \omega_s^2}{\partial t_n} = \frac{\phi_s^T (K_{\Delta t} - \omega_s^2 M_{\Delta t}) \phi_s}{\phi_s^T M \phi_s}, \quad \text{with } s = 1, 2 \quad (5-10)$$

where the sensitivity of the eigenvalue for the thickness is denoted as $\frac{\partial \omega_s^2}{\partial t_n}$ and ϕ_s is the corresponding eigenmode. The resulting sensitivities are shown in Figure 5-7 for respectively the first (a) and the second (b) eigenvalues of the tower structure. The number of tower elements is shown on the vertical axis, starting with zero representing the tower top and goes down to -40 which represents the tower bottom. The wall thickness perturbation can be seen as an absolute quantity. Therefore, by comparing Figure 5-7(a) and Figure 5-7(b) with one and other. It can be seen that the second eigenvalue is far more susceptible for a wall thickness perturbation than the first eigenvalue, due to higher order of magnitude. By further studying, the figure, it is noticed that between some positions (e.g. -30 and -31) the sensitivity suddenly goes to zero. This implies that the support structure is not sensitive to changes in wall thickness. This insensitivity is due to the installed flanges at those tower elements. Moreover, the length of these elements are smaller concerning the rest of the tower elements. As a consequence, these flange elements have higher stiffness values resulting in the insensitive response for wall thickness perturbations. The resulting higher stiffness can be deducted from the Euler-Bernoulli matrices stated in Equation (B-1).

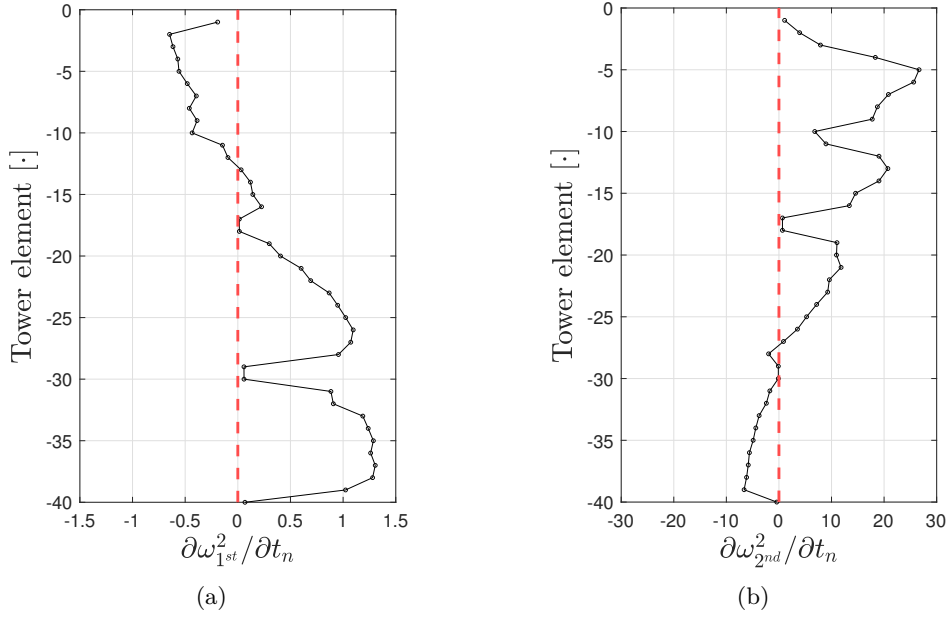


Figure 5-7: Eigenfrequency sensitivity for the two tower modes with respect to the vertical tower element number. (a) shows for the eigenvalue ω_{1st}^2 (b) shows for the eigenvalue ω_{2nd}^2 .

It is shown that the wall thickness influences the eigenfrequency of the support structure. Furthermore, it can be seen that the sensitivities are positively or negatively correlated for different tower elements. By partitioning the elements with similar magnitude in sensitivity, it can be assumed that the sum over these partitioned elements times the amplitude of the sensitivity will result in changing the overall eigenfrequency. Therefore, the tower is partitioned in two sections taking the transitions between positive and negative correlations into account.

- The tower elements $n \in [1, \dots, 9]$ are stacked together. Due to the negative correlation for the first eigenfrequency (Figure 5-7a) and the positive correlation for the second eigenfrequency (Figure 5-7b).
- The tower elements $n \in [10, \dots, 30]$ are partitioned, namely there are for both the first and second eigenfrequency positively correlated.

The tower is divided into two sections and, subsequently, the perturbations per partitioning are defined as Δt_1 and Δt_2 , for respectively the first and second tower section. This partitioning with corresponding perturbations is substituted in Equation (5-8) resulting in the following extended system description of the wind turbine model.

$$\tilde{M}_r \ddot{\eta} + \tilde{D}_r \dot{\eta} + \tilde{K}_r \eta = \begin{bmatrix} -\tilde{V}_r^T M_{\Delta t_1} \tilde{V}_r \Delta t_1 & -\tilde{V}_r^T M_{\Delta t_2} \tilde{V}_r \Delta t_2 & -\tilde{V}_r^T K_{\Delta t_1} \tilde{V}_r \Delta t_1 & -\tilde{V}_r^T K_{\Delta t_2} \tilde{V}_r \Delta t_2 & \tilde{V}_r b \end{bmatrix} \begin{bmatrix} \dot{\eta}_1(t) \\ \dot{\eta}_2(t) \\ \eta_1(t) \\ \eta_2(t) \\ F_T(t) \end{bmatrix} \quad (5-11)$$

where $M_{\Delta t_1} = \frac{\partial M}{\partial t_1}$ ($K_{\Delta t_1} = \frac{\partial K}{\partial t_1}$) integrate the derivative mass and stiffness matrices of the first partitioning $n = [1, \dots, 9]$. The same reasoning is followed for $M_{\Delta t_2} = \frac{\partial M}{\partial t_2}$ ($K_{\Delta t_2} = \frac{\partial K}{\partial t_2}$), where the second partitioning $n = [10, \dots, 30]$ is integrated. In order to make the wall thickness perturbation available for the optimization, they are recasted into controllable inputs as follows:

$$\begin{aligned} F_{M_{\Delta t_1}} &= \Delta t_1 \ddot{\eta}_1(t) \\ F_{M_{\Delta t_2}} &= \Delta t_2 \ddot{\eta}_2(t) \\ F_{K_{\Delta t_1}} &= \Delta t_1 \eta_1(t) \\ F_{K_{\Delta t_2}} &= \Delta t_2 \eta_2(t) \end{aligned} \quad (5-12)$$

The above stated input definitions $F_{M_{\Delta t_1}}$, $F_{M_{\Delta t_2}}$, $F_{K_{\Delta t_1}}$ and $F_{K_{\Delta t_2}}$ are substituted in Equation (5-11). The final extended form for the controller synthesis is obtained. The extended form is coupled with the aerodynamic model, as explained in Chapter 4. The final extended turbine description is as follows:

$$\begin{aligned} \hat{T}_r &= J_r \dot{\Omega}_r \\ \tilde{M}_r \ddot{\eta}(t) + \tilde{D}_r \dot{\eta}(t) + \tilde{K}_r \eta(t) &= \dots \\ \left[\begin{array}{cccc|c} -\tilde{V}_r^T M_{\Delta t_1} \tilde{V}_r & -\tilde{V}_r^T M_{\Delta t_2} \tilde{V}_r & -\tilde{V}_r^T K_{\Delta t_1} \tilde{V}_r & -\tilde{V}_r^T K_{\Delta t_2} \tilde{V}_r & \tilde{V}_r b \end{array} \right] \begin{bmatrix} F_{M_{\Delta t_1}} \\ F_{M_{\Delta t_2}} \\ F_{K_{\Delta t_1}} \\ F_{K_{\Delta t_2}} \\ F_T(t) \end{bmatrix} \end{aligned} \quad (5-13)$$

Equation (5-13) is then recasted into state-space formulation and coupled with the aerodynamic model. The difference between the original and extended wind turbine model is that the latter has four more inputs than the original system. One can imagine when the eigenfrequencies change due to a wall thickness perturbation, the corresponding eigenmodes will change as well. The eigenmode sensitivity will be analysed in the next section, in order to see whether the new perturbed modeshape is significantly different.

Eigenmode sensitivity

In order to be sure that the wall thickness stays in the bound of changing the fundamental eigenmodes of the structure, the eigenmode sensitivity is consulted (Gérardin and Rixen, 2014). The modeshape sensitivity is calculated by using the method presented in Appendix A. Therefore, it follows the same procedure as in Chapter 3 for the mass-spring-damper system. The first step is to compute the perturbed modeshape which is added to the original modeshape ϕ_c , which provides a updated modeshape ϕ_{new} using:

$$\phi_{new} = \mu \frac{\partial \phi}{\partial t_i} + \phi_c \quad (5-14)$$

The computed sensitivities are used to give an absolute change in the wall thickness over a selected number of elements. Recall the assembled mass and stiffness matrices of Section 5-2. Thus the matrices are differentiated per element. After that, the derivatives of the mass and stiffness of every element are stacked in the overall derivative matrices. The matrices M^{n*} and

K^{n*} , corresponds to the element n , for which $M^{n*} = K^{n*} = 0$ corresponds to no adjustments in wall thickness. The derivative matrices follow the same coupling principles, as explained in Chapter 4 (Panzer et al., 2009). The following example illustrates how the differentiation of the mass matrix per element is executed (K^* follows the same principle):

$$M^* = \begin{bmatrix} M_{11}^{1*} & M_{12}^{1*} & 0 & \dots & 0 \\ M_{21}^{1*} & M_{22}^{1*} + M_{11}^{2*} & M_{12}^{2*} & \dots & 0 \\ 0 & M_{21}^{2*} & M_{22}^{2*} + M_{11}^{3*} & \dots & 0 \\ \vdots & \vdots & \vdots & \ddots & \vdots \\ 0 & 0 & 0 & & M_{22}^{N_{tower}^*} \end{bmatrix}$$

The change of wall thickness to the elements are varied with the same constant value of Δt . It is interesting to see what the influence is of different wall thickness perturbations on every tower element. Therefore, the influence of an additional thickness of 1 [mm] and 10 [mm] to every tower element is computed in Equation (5-14) by using respectively $\mu = 1 \cdot 10^{-3}$ and $\mu = 10 \cdot 10^{-3}$. The resulting modeshape of the perturbed system is compared to the nominal case is depicted in Figure 5-8. It can be seen that by changing the wall thickness by $\Delta t \in [-10, 10]$ [mm] will influence the modeshapes. For the case of changing the wall thickness by $\Delta t \in [-1, 1]$ [mm], for the modeshapes, a significant difference is not noticed. The Modal Assurance Criterion (MAC) values are stated in Table 5-2 for both cases. By consulting the MAC values of the original and perturbed mode-shapes for both cases no remarkable difference is noticed for the most two dominant mode-shapes. Therefore, nonlinear behavior is not expected. However, by changing the wall thickness by 10 [mm], the second tower bending will increase in response when excited, due to the higher normalized deflection for the tower top.

Table 5-2: MAC values for different wall thickness perturbations.

MAC value	$\frac{\phi_1}{t_n}$	$\frac{\phi_2}{t_n}$
$\Delta t = [-1, 1]$	1.00	1.00
$\Delta t = [-10, 10]$	0.9984	0.9997

Given the result that the eigenmodes are not strongly influenced by a perturbation of the structural parameter of interest, the reduction method is assumed to be valid when changing the structural parameters. Therefore, the method of extending the system with tunable elements seems a logical approach. The CSO can use this extension method and now with the preliminaries discussed, the weighting functions and general plants can be formulated. In the next section, the different design case are formulated, where each individual design case will address different objectives in order to make a fair comparison.

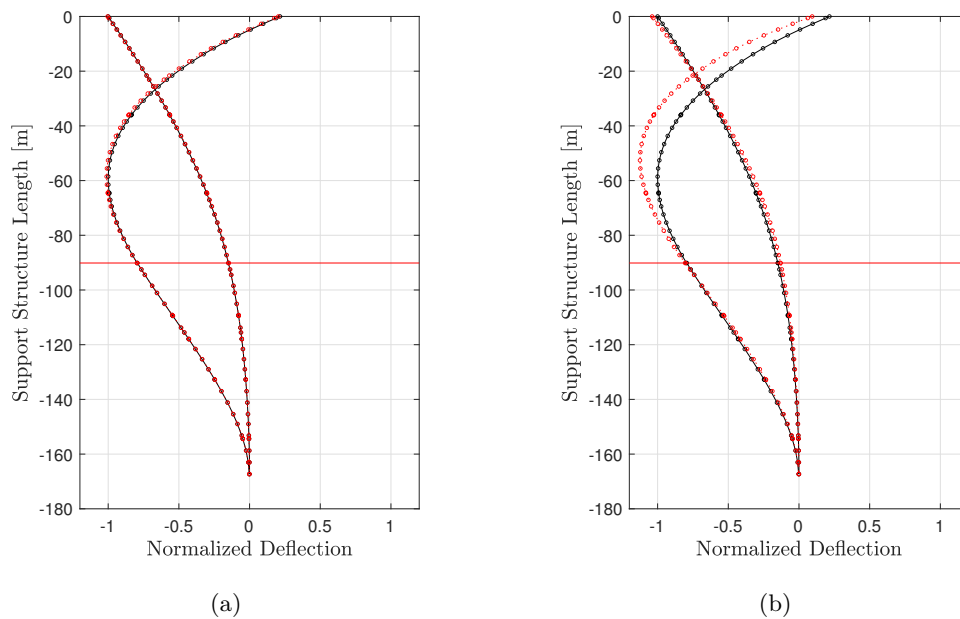


Figure 5-8: Modeshape sensitivity of different perturbations of wall thickness namely $\Delta t = [-1, 1]$ [mm] (a) and $\Delta t = [-10, 10]$ [mm] (b) for the first and second tower bending mode. The original modeshapes are shown in black. The updated modeshapes are shown in red.

5-3 The resulting design cases

In the previous sections, the controller and structural objectives are mentioned. The main goal of this section is to recast these objectives into frequency domain specifications. This is done through shaping the closed-loop functions of the turbine model in the desired shape through weighting functions. By means of suitable weight functions and generalized plant configurations, it is possible to define an upper bound on the closed-loop transfer functions as shown in Chapter 2. The complete scheme of defining the cases is shown in Figure 5-1. Therefore, three general design cases are defined to show the influence of addressing several objectives in the multi-variable design approach, which are as follows:

- Case 1: the rotor speed controller with nominal performance and will serve as a benchmark. For this control loop the measured rotor speed should track the reference rotor speed of 10.8 [rpm] while repressing the disturbance introduced by the wind.
- Case 2: the derived rotor speed controller including the fatigue load reduction. This is achieved by bounding the tower top accelerations \ddot{y}_t with a weight. For this case, three different sub-cases are defined, one to show the use of a separate control-loop including the active tower damper approach of Section 5-1 (case 2a) and one where the tower top accelerations are induced by the rotor speed disturbance (case 2b/c).
- Case 3: the controller structure optimization for the extended wind turbine system. For this case, the structural objective of minimizing the wall thickness is included. Two

different sub-cases are defined, for which the rotor speed controller design is combined with the wall thickness perturbations (case 3a) and one with an additional constraint on the tower top accelerations (case 3b).

The three design cases will be defined in consecutive order. The generalized plants and corresponding weight functions are presented as well. Each case concludes with the corresponding optimization, which is the formalization of the \mathcal{H}_∞ -norm minimization.

Case 1: Rotor Speed Controller design

With the basic initial control design discussed in Section 5-1, it is time to use these principles in the \mathcal{H}_∞ -control design framework as presented in Chapter 2. For the reference tracking capability of the rotor speed, the sensitivity function is of interest, $S(s) = \frac{1}{1+L(s)}$, where the loop-gain is given by $L(s) = K_{rsc}(s)G_{\hat{\beta}_d \rightarrow \hat{\Omega}_r}(s)$. Therefore, analyzing the sensitivity of the rotor error $\Delta\Omega_r$ to disturbances w_1 on the signal will be of special interest for obtaining a controller with adequate reference tracking capabilities. By introducing a suitable weighting function on this sensitivity function, it possible to shape the closed-loop transfer function in the desired shape.

Weight design for rotor speed

The design of the weight function is based on the step response with corresponding control gains for the RSC obtained from Section 5-1. The weight functions makes use of two first order functions, where the parameterization is given in Table 5-3. The resulting weight function is given by Equation (5-15).

Table 5-3: Parameters for the weight design of $W_{p,rsc} = \text{series}(W_{p,1}, W_{p,2})$

	$M_{p,i}$	$A_{p,i}$	$\omega_{B,i}$
$W_{p,1}(s)$	8	$1 \cdot 10^{-5}$	0.15
$W_{p,2}(s)$	0.15	0.5	5

$$W_{p,i}(s) = \frac{s/M_{p,i} + \omega_{B,i}}{s + A_{p,i}\omega_{B,i}} \quad (5-15)$$

$$W_{p,rsc}(s) = \text{series}(W_{p,1}, W_{p,2})$$

The parameters are selected by knowing the limitations of the real pitch system of the 8.0MW turbine system. Figure 5-9 depicts the performance weight design by combining the initial first-order weights. In general, maximizing the $\omega_{B,i}$ yields a small rise time which is useful in terms of performance. However, one drawback of a high bandwidth is that it could result in a system which is sensitive to noise.

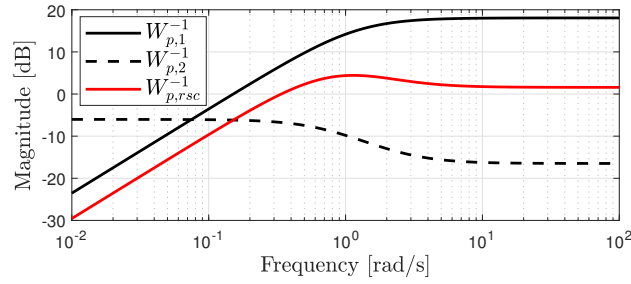


Figure 5-9: Inverse weight design of $W_{p,1}$ and $W_{p,2}$, which in series forms the final weight design $W_{p,rsc}$.

The weight is placed on the sensitivity function and is defined as the transfer function $T_{w_1 \rightarrow \Delta\Omega_r}(s)$ between the disturbance w_1 to the rotor speed error $\Delta\Omega_r$. The effect of varying the control gains K_p and K_i on the sensitivity function is shown in Figure 5-10. It is shown that for higher K_p values, the cross-over at -3 line [dB] is increased. This results in a higher bandwidth for the system. Furthermore, the increase in control gains shows that the peak gain of the sensitivity function increases and, therefore, violates the bound of the performance weight. The weight involves a trade-off between the fast response and does not allow for obtaining too aggressive control gains, which are within the provided limits of the controller gains in BHAWC.

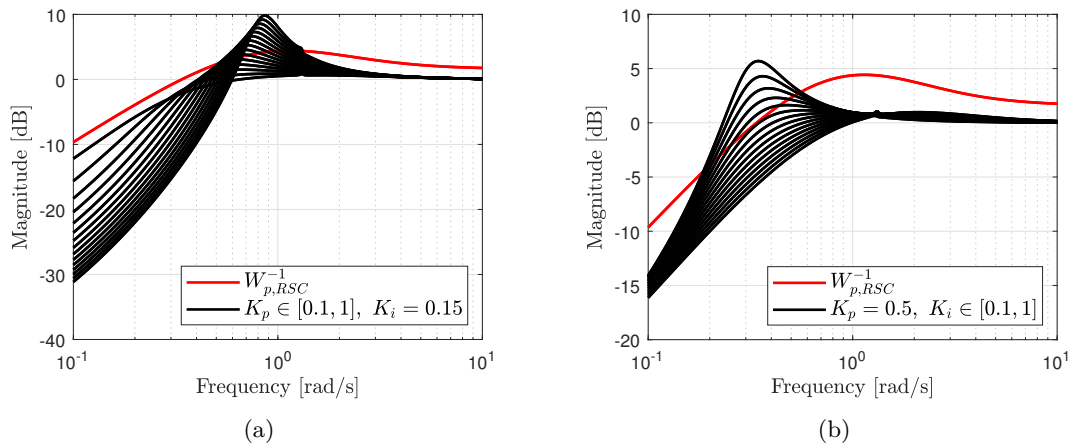


Figure 5-10: Sensitivity plot of different CL system using different controller parameters for the RSC. It is shown that for multiple setting the bound on the sensitivity is violated. The settings are given by (a) $K_p \in [0.1, 1]$ and $K_i = 0.15$ and (b) $K_p = 0.5$ and $K_i \in [0.1, 1]$.

Generalized plant configuration

The schematic representation of the control design combined with the weighting function is shown in Figure 5-11. The chosen weighting function is $W_{p,rsc}$, which imposes the sensitivity function of the rotor speed. This weight is needed to address the controller objective for adequate rotor speed tracking. The corresponding sensitivity of the closed-loop system is

bound by the inverse of this weight $1/W_{p,rsc}$. From the generalized plant configuration in Figure 5-11, it is noticed that the inputs wind speed \hat{V}_{wind} and rotor speed $\hat{\Omega}_{ref}$ to the wind turbine model. These inputs were introduced in Figure 4-1 and are from now on seen as redundant inputs. Therefore, these inputs are not included for controller design.

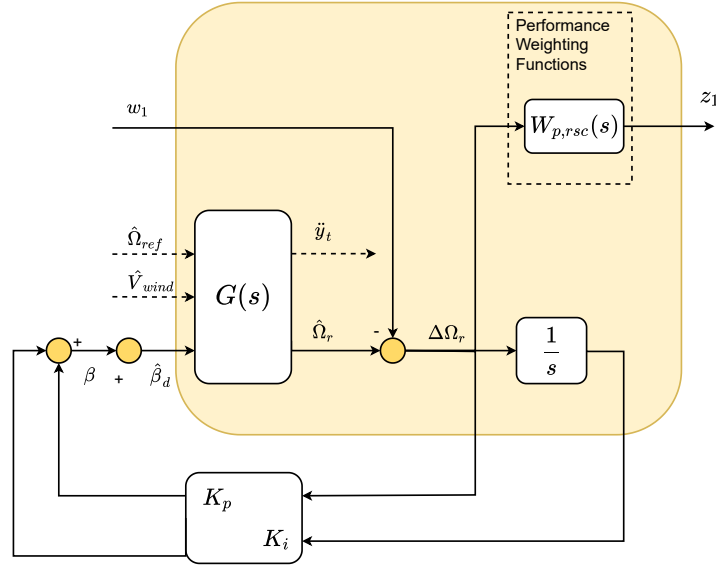


Figure 5-11: Generalized plant description (yellow area) of the proposed \mathcal{H}_∞ problem for case 1. The wind turbine system is given by $G(s)$. The disturbance is given by w_1 on the rotor speed introduced by the wind. The performance channel is given by z_1 . The weighting function is given by $W_{p,rsc}$ for rotor tracking. The controller is a fixed-structured controller as $K = \text{diag}(K_p, K_i)$. The controller output provides the desired pitch actuation $\hat{\beta}_d$.

Now with the weighting functions and generalized plant discussed, the resulting optimization for case 1 is shown in Equation (5-16) and will be used in Chapter 6.

$$\begin{aligned} \min_{s.t.} \quad & \gamma \\ & \|W_{p,rsc}S\|_\infty < \gamma \end{aligned} \quad (5-16)$$

where γ is the performance index and it should satisfy $\gamma < 1$ in order to guarantee closed-loop performance of the designed \mathcal{H}_∞ rotor speed controller. Furthermore, it is clear that for case 1 only the rotor speed error objective is taken into account. Therefore, the upcoming case will incorporate the active tower damping by using the tower top acceleration \ddot{y}_t as a controllable input.

Case 2: The Rotor Speed Controller and Active Tower Damper

For the second case, an additional objective of active tower damping is added to the \mathcal{H}_∞ -control design problem. Therefore, the case will address both the controller objectives, namely reducing the rotor speed error and mitigating the tower top accelerations. The generalized plant description of Figure 5-11 will be altered by including the tower top accelerations as a controllable input, as explained in Section 5-1. Subsequently, the band-pass filter of

Equation (5-5) is used, where $\zeta = 0.8$ and ω_n equals the first tower bending frequency at 1.33 [rad/s]. Furthermore, it is interesting to see how the outcome of the previous section is influenced by addressing this multi-variable design. It is expected that the attenuation of the first tower bending mode will interact with the parameters and performance of the RSC. The RSC is designed with the same second order weight $W_{p,rsc}$ in Equation (5-15) with the corresponding parameters stated in Table 5-3. In order to attenuate the peak of the subsystem $G_{\beta \rightarrow \ddot{y}_t}$, for ease the notation of G_2 is used, the following weight function will be introduced.

Weight design for tower top acceleration

For tower top acceleration, a simple constant gain $k_{\ddot{y}_t}$ is used as inverse weighting function $1/W_{p,\ddot{y}_t}$. The aim of using only a simple gain is to attenuate the peak in the subsystem from pitch angle $\hat{\beta}_d$ to tower top acceleration \ddot{y}_t , which then corresponds to active damping of the first tower bending mode. The working principle is illustrated in Figure 5-12. It can be seen that by using a simple constant gain, the peak of the closed-loop transfer function should be lowered, this principle is shown in the work of Shan (2018) as well. Furthermore, it is noticed that the proposed method follows the same reasoning as the control design of the initial tower feedback loop in Section 5-1.

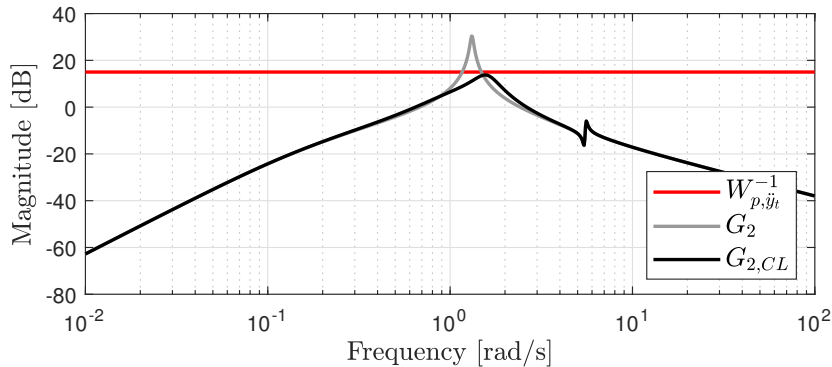


Figure 5-12: Weight design of $1/W_{p,\ddot{y}_t}$, the OL system and CL subsystem for the initial control design is shown as well.

For this case, the same weighting function on the sensitivity function of the rotor speed is used. Therefore, two weighting function parameters have been presented, which are related to the control objectives. These weighting functions represents a problem specific parameterization of the control design. Due to the conflicting nature of the control objectives, the overall problem is dependent on several parameters. The weight functions are included in a new generalized plant configuration, which will be presented in the next section.

Generalized plant configuration

The schematic representation of Figure 5-11 is modified to include the ATD control-loop. In this problem, the following controller parameters (K_p, K_i, K_{D_p}) are sought, such that the

required performance criteria are satisfied. The chosen weighting functions are $W_{p,rsc}$ and W_{k,\ddot{y}_t} , which are respectively the weight function for the rotor speed sensitivity and the tower top accelerations. These weight are needed to address the controller objectives as mentioned earlier in control design. The resulting generalized plant used for the design case 2 is depicted in Figure 5-13.

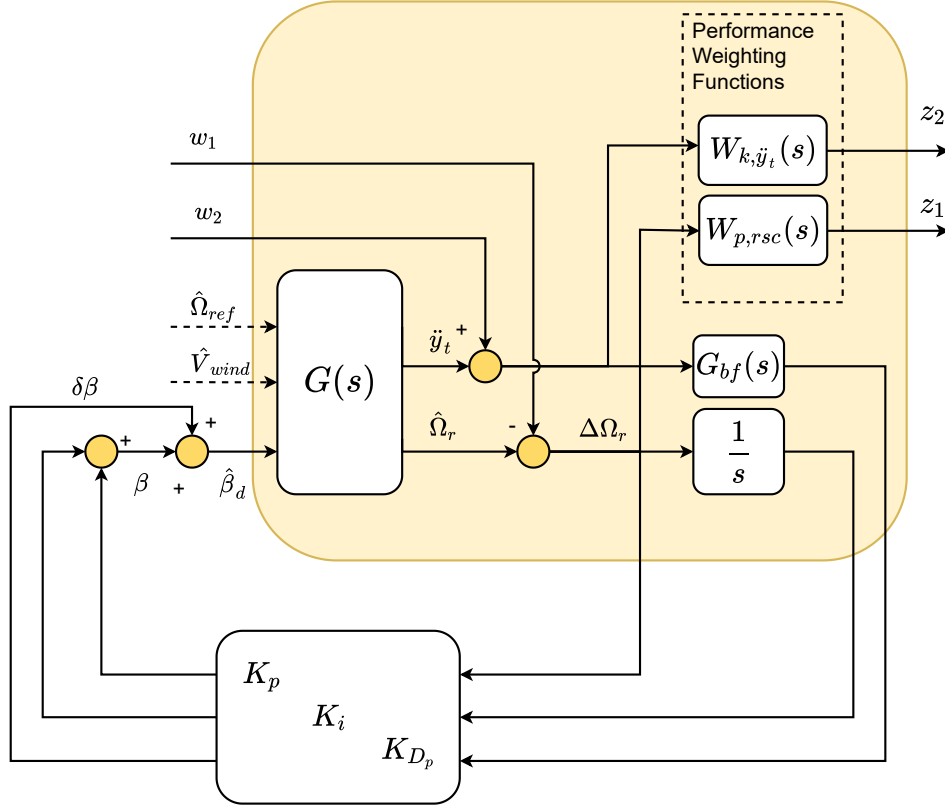


Figure 5-13: Generalized plant description (yellow area) of the proposed multi-objective problem of case 2. The wind turbine system is given by $G(s)$ and the band-pass filter is given by $G_{bf}(s)$. The disturbances are given by w_1 on the rotor speed, and w_2 on the tower top accelerations \ddot{y}_t . The corresponding performance channels are z_1 and z_2 . The weighting functions are given by $W_{p,rsc}$ and W_{k,\ddot{y}_t} . The controller is a fixed structure controller as $K = \text{diag}(K_p, K_i, K_{D_p})$. The controller output is the pitch actuation β provided by the RSC and the additional pitch actuation $\delta\beta$ by the ATD.

The resulting optimization for case 2 can be formalized as follows:

$$\begin{aligned} \min_{s.t.} \quad & \gamma \\ & \left\| \begin{array}{c} W_{p,rsc} S \\ W_{k,\ddot{y}_t} G_{w_2 \rightarrow \ddot{y}_t} \end{array} \right\|_{\infty} < \gamma \end{aligned} \quad (5-17)$$

The proposed method is applied to find the controller parameters for K_p , K_i and K_{D_p} such that the performance condition of Equation (5-17) ($\gamma < 1$) is satisfied. It is found in Chapter 6 that using the separate ATD control-loop in combination with the proposed band-pass filter and fixed gain resulted in unstable simulations for the verification part. This is due to

the underestimated aerodynamic damping in the linear derived wind turbine model. This underestimation causes a higher obtained damping value for K_{D_p} . Therefore, two sub-cases are proposed, where the RSC is derived by taken a different approach. The rotor speed disturbance w_1 induces the tower top accelerations as well. As a consequence, the a load reducing RSC can be derived by placing a fixed gain on the tower top acceleration and removing the applied disturbance w_2 , resulting in different control gains (K_p, K_i) for the RSC. It should be mentioned for those sub-cases no separate ATD control-loop is included. For these particular cases, Equation (5-17) is rewritten into the following optimization:

$$\begin{aligned} \min_{s.t.} \quad & \gamma \\ & \left\| \begin{array}{c} W_{p,rsc} S \\ W_{k,\ddot{y}_t} G_{w_1 \rightarrow \ddot{y}_t} \end{array} \right\|_{\infty} < \gamma \end{aligned} \quad (5-18)$$

The weight selection for all the second subcases are defined in Table 5-4.

Table 5-4: Weight selection for case 2.

Weight function	Case 2a	Case 2b	Case 2c
Applied channel	$G_{w_2 \rightarrow \ddot{y}_t}$	$G_{w_1 \rightarrow \ddot{y}_t}$	$G_{w_1 \rightarrow \ddot{y}_t}$
W_{k,\ddot{y}_t}	0.18	0.01	0.05

Case 3: Controller Structure Optimization

In this section, the CSO case will be defined for the extended wind turbine system. The first generalized plant of Figure 5-11 is not suitable anymore and modified for including the weights for the structural perturbations. Therefore, the section starts with the weight functions followed by the adjusted generalized plant description. The case is divided into two subcases, where one subcase takes the tower top accelerations into account whether the other not.

Weight design for the CSO

The weights for the controller structure optimization are defined as follows:

- $W_{p,rsc}$ is the weight design for the rotor speed and is for the CSO case the same as Equation (5-15) in the previous section.
- W_{k,\ddot{y}_t} is a simple constant gain and is placed on the tower top accelerations, which are caused by the disturbance on the rotor speed leading to a tower top motion. Therefore, no additional loop is needed for the active tower damper.
- $W_{p,\Delta t_1}$ is a weight for imposing the wall thickness to change for the tower top section. By enforcing the wall thickness to minimize, a new signal is created, by summation of the signal η_1 before and after the multiplication with the perturbation Δt_1 as shown in Figure 5-14. By doing so, a new signal is created ($\eta_1 + \Delta t_1 \eta_1$). Minimizing this signal with the weight will result in a minimization of the wall thickness.

- $W_{p,\Delta t_2}$ follows the same reasoning as the previous item. The weight imposes a bound on the wall thickness of the bottom tower section. The summation is applied as well as enforcing the minimization. The new signal is defined by the summation of the signals ($\eta_2 + \Delta t_2 \eta_2$).

Generalized plant configuration

The generalized plant configuration of Figure 2-7 is modified to include the wall thickness perturbations Δt_1 and Δt_2 . Thus, in this problem, the following controller parameters (K_p , K_i , Δt_1 , Δt_2) are sought, such that required performance criteria are satisfied. Note that, for the controller structure design case no separate tower control-loop is included. This exclusion is because the number of control parameters heavily influence the minimization of the non-smooth optimization method. Additionally, by taking the tower accelerations into account for the RSC design, the tower accelerations can also be reduced according to Shan (2018). There will be a total of four weight placed on different signals. These weights should perform a wall thickness reduction and at the same time, capture the performance criteria on the RSC design. The generalized plant description used for the CSO case is shown in Figure 5-14.

The weighting functions are applied on the signals as described in the generalized plant configuration. The input to the system is the disturbance channel w_1 acting on the rotor speed. The performance channels are z_1 , z_2 , z_3 , z_4 for respectively, the rotor speed, tower accelerations, wall thickness tower top and wall thickness tower bottom. What is already mentioned is that this case is divided into two subcases. Firstly, no weight will be placed on the tower top accelerations. After that, for the second case, this weight will be included. Therefore, the resulting optimization for case 3 can be formalized as follows:

$$\begin{aligned}
 & \min_{s.t.} \gamma \\
 & |\Delta t_1| < 1 \cdot 10^{-2}, \quad |\Delta t_2| < 1 \cdot 10^{-2} \\
 & \left\| \begin{array}{l} W_{p,rsc} S_{w_1 \rightarrow \Delta \Omega_r} \\ W_{k,\ddot{y}_t} G_{w_1 \rightarrow \ddot{y}_t} \\ W_{p,\Delta t_1} G_{w_1 \rightarrow \eta_1 + \Delta t_1 \eta_1} \\ W_{p,\Delta t_2} G_{w_1 \rightarrow \eta_2 + \Delta t_2 \eta_2} \end{array} \right\|_{\infty} < \gamma
 \end{aligned} \tag{5-19}$$

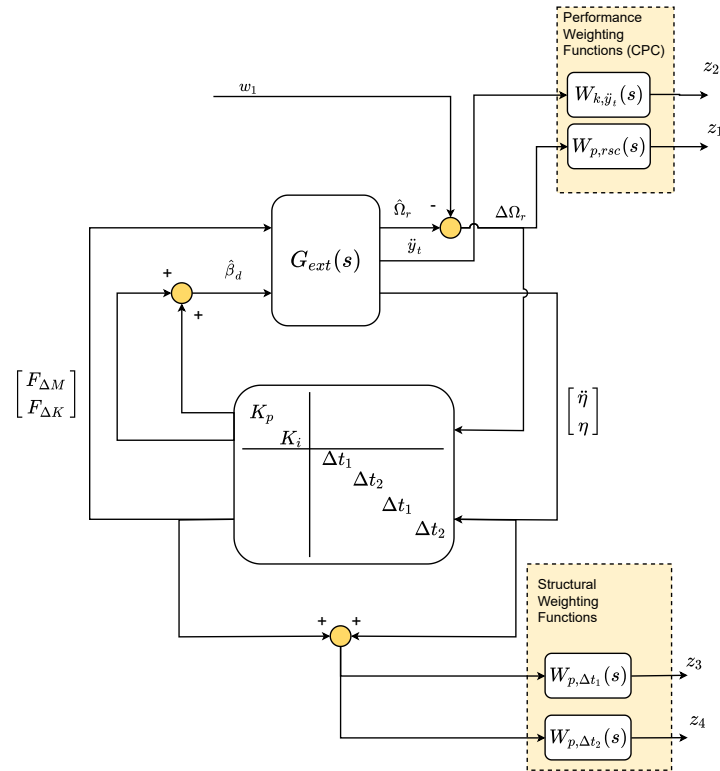


Figure 5-14: Generalized plant configuration of the proposed CSO problem. The extended wind turbine system is given by $G_{ext}(s)$. The disturbance signal w_1 is acting on the rotor speed. The performance channels are given by z_1 and z_2 for the controller design part. The performance channels of the plant alterations are given by z_3 and z_4 .

The weight selection for the cases is stated in Table 5-5, which are manually tuned to perform a wall thickness minimization. This manual tuning process is the same as for the W_{k,\dot{y}_t} . The weight is increased up to the point that it does not provide different results. The influences $W_{\Delta t_1}$ and $W_{\Delta t_2}$ are weighted simultaneously, to lower the sum of the wall thickness change $\Delta t_1 + \Delta t_2$. Furthermore, by including weight on the tower top accelerations, the rotor speed disturbance forces a tower top acceleration, and therefore the controller is obliged to change the gains. In comparison to case 3a, the additional weight to the \mathcal{H}_∞ -norm reduction will narrow the solution space. It is expected that the controller gains of the designed RSC for case 3b will differ from case 3a. The results of the two subcases will be presented in the next chapter.

Table 5-5: Weight function design input values for the static constants.

Weight function	Case 3a	Case 3b
W_{k,\dot{y}_t}	0	0.01
$W_{p,\Delta t_1}$	0.01	0.01
$W_{p,\Delta t_2}$	0.015	0.015

5-4 Summary

The main goal of this chapter is as follows:

"Provide a framework for simultaneous structured controller design and tunable plant optimization through frequency-based optimization"

The wind turbine model, as presented in Chapter 4, is extended by using the sensitivity of changing the eigenfrequencies by a wall thickness perturbations. It was seen that changing the wall thickness along the tower length, influences the eigenfrequencies to shift negatively or positively. Therefore, these positive and negative correlated tower sections are partitioned together with the corresponding sign. Therefore, allowing to alter an entire tower section. The rotor speed controller is designed by using a simple PI-controller. The RSC controller is extended with an active tower control-loop, this resulted in the mitigation of the FA acceleration of the tower top for the initial controller design case.

For proving the effectiveness of the proposed framework, four different cases are defined in this chapter, which addresses different controller or structure design scenarios. For each design case, a \mathcal{H}_∞ -norm minimization was formulated while using weights on different performance channels. The following general design cases are defined in this chapter:

- Case 0: rotor speed controller and an active tower damper control-loop through loop-shaping principles. The control gains of the rotor speed controller correspond with the initial controller used in BHAWC.
- Case 1: rotor speed controller through fixed-structured \mathcal{H}_∞ control design
- Case 2: rotor speed controller and active tower damper through fixed-structured \mathcal{H}_∞ control design.
- Case 3: the CSO of the extended wind turbine description involving wall thickness perturbations and rotor speed control.

In the next chapter, the different cases will be simulated and the results will be presented.

Chapter 6

Simulation Results

In this chapter, the results of the defined cases of the multi-objective controllers discussed in Chapter 5 will be presented. The following design cases are simulated and presented in consecutive order:

- Case 1: the Rotor Speed Controller (RSC) with nominal performance. For this control case the measured rotor speed should track the reference rotor speed.
- Case 2: the RSC combined with load reducing properties.
- Case 3: the controller structure optimization of the extended wind turbine description.

The main goal of this chapter is:

"Apply the controller-structure optimization to prove its effectiveness on the linear 8.0MW SGRE wind turbine model, while achieving wall thickness reduction and rotor tracking performance"

The goal originates from one of the subgoals stated in Chapter 1. The chapter is built up as follows. Firstly, the controller design cases are presented from Section 6-1 till Section 6-3. After that, the resulting design cases are compared with one another in Section 6-4. In Section 6-5, the found controller parameters and an updated tower of the 8.0MW turbine are verified with the high-fidelity Bonus Horizontal Axis Wind turbine Code (BHAWC) model. Finally, the chapter conclusions are presented in Section 6-6.

6-1 Case 1: The Rotor Speed Controller

In the first case, the optimization framework is used for only the control design of the RSC through \mathcal{H}_∞ -norm minimization. The RSC makes use of classical PI-controller design for tracking the rotor speeds. The controller parameters (K_p, K_i) are placed on the diagonal to maintain the diagonal controller structure. The resulting optimization for case 1 is shown in Equation (6-1).

$$\begin{aligned} \min_{s.t.} \quad & \gamma \\ & \|W_{p,rsc}S\|_\infty < \gamma \end{aligned} \quad (6-1)$$

The optimization of Equation (6-1) is executed with the *Robust Control Toolbox* using the non-smooth optimization method *Hinfstruct*, which allows for fixed-controller design. The weight $W_{p,rsc}$ is as presented in Section 5-3 and imposes a bound on the sensitivity function S . The results of this optimization are shown below.

Results of case 1

The problem statement of Equation (6-1) implies a Single-Input Single-Output (SISO) problem due to the consideration of only controlling and using the rotor speed signal. The results are shown in Figure 6-1 for both the frequency response and time-domain simulation. The proposed norm reduction gives a satisfactory result of $\|W_{p,rsc}S\|_\infty = 0.833$ with the found controller parameters $K_p = 0.646$ and $K_i = 0.275$. Therefore, the desired response of the rotor speed controller is obtained. Figure 6-1a shows the resulting sensitivity function of case 1 and compared to case 0. It can be seen that the resulting sensitivity function does not violate the imposed bound. Figure 6-1b shows the step response for both case 1 and case 0 (initial design). For the rotor speed controller through \mathcal{H}_∞ analysis, the settling time equals 11 [s], and the peak amplitude is 1.16 [rad/s]. The resulting step response for the initial design has a settling time of 13.35 [s]. An improvement of 2.35 [s] is noticed. Subsequently, comparing the rise time between the two controller design cases is 2.40 [s] and 2.88 [s] for respective case 1 and case 0. Thus, the derived rotor speed controller through \mathcal{H}_∞ will have a faster response.

This case only tackles the rotor tracking control objective and will be verified in the high-fidelity BHAWC model and compared with the control gains of the other cases in Section 6-5. Furthermore, all the characteristics of the found parameters are summarized along with the upcoming cases in Section 5-4.

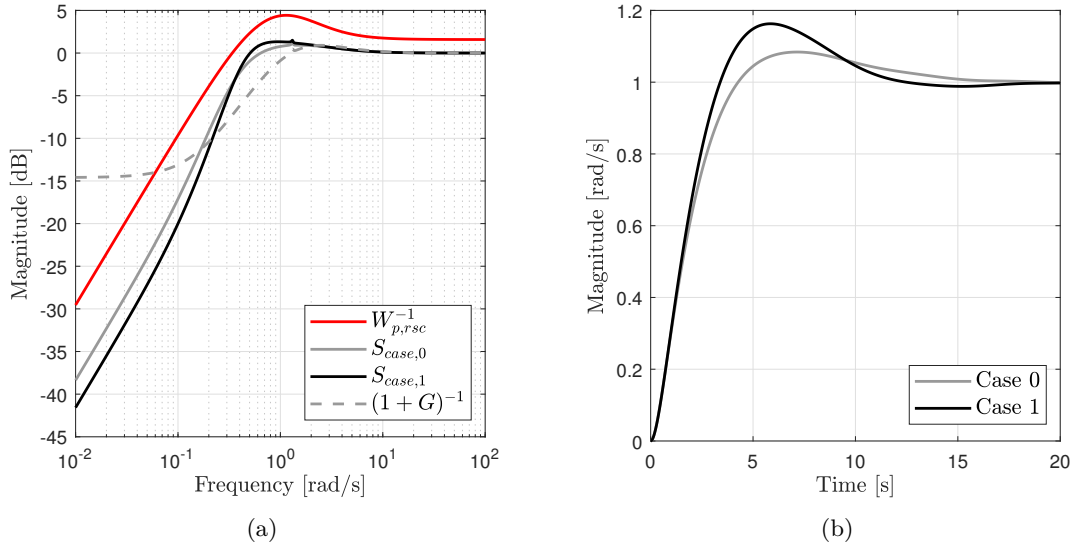


Figure 6-1: (a) shows the bode magnitude plots of the initial sensitivity function (—) and the sensitivity function obtained with the optimized controller (—) is shown. The inverse of the performance weight $W_{p,rsc}$ (—) is shown as well. (b) shows the step responses from the pitch angle to the rotor speed for both the case 0 (—) and case 1 (—).

6-2 Case 2: The Rotor Speed Controller and Active Tower Damper

In this section, an additional objective of active tower damping is added to the \mathcal{H}_∞ control design problem. This case will address reducing the rotor speed error and mitigating the tower top accelerations. It is expected that the attenuation of the first tower bending mode interacts with the parameters and performance of the RSC. The subsystem $G_{\beta \rightarrow \ddot{y}_t}$ contains a Right-Half-Plane (RHP) zero and perhaps limits the performance of the problem. The weights are selected as follows:

- The RSC is designed with the same second order weight $W_{p,rsc}$ of Equation (5-15) with the corresponding parameters stated in Table 5-3.
- The tower top acceleration is imposed by weight W_{k,\ddot{y}_t} , which is a simple constant $k_{\ddot{y}_t}$. The gain was initialized at a value of 6 [dB], which resulted in violations of the performance index. Therefore, the gain was slowly increased up to a point, the performance index $\gamma < 1$ was satisfied. Additionally, it was found by only relaxing the weight for achieving $\gamma < 1$ resulted in aggressive additional damping for the tower bending. As a consequence, the corresponding step responses of the Closed-Loop (CL) are analyzed even further to relax the weight W_{k,\ddot{y}_t} .

The resulting optimization for case 2a can be formalized as follows:

$$\begin{aligned} \min_{s.t.} \quad & \gamma \\ & \left\| \begin{array}{c} W_{p,rsc} S \\ W_{k,\ddot{y}_t} G_{w_2 \rightarrow \ddot{y}_t} \end{array} \right\|_\infty < \gamma \end{aligned} \quad (6-2)$$

The optimization for case 2b and case 2c is slightly different, namely $G_{w_2 \rightarrow \ddot{y}_t}$ in Equation (6-2) is replaced by $G_{w_1 \rightarrow \ddot{y}_t}$. The proposed method is applied to find the controller parameters K_p , K_i and K_{D_p} such that the performance condition is satisfied. The results of case 2b and case 2c are only for designing RSC gains (K_p, K_i) by including a weight on the tower top acceleration, as explained in Chapter 5.

Results of case 2

The problem involves a multi-variable approach and as a consequence, it becomes harder to tune the system weights. This results from the reduced design space, due to the additional constraints. The results are shown in Figure 6-2 and Figure 6-3 for respectively, the RSC design and the Active Tower Damper (ATD) design. The solution with the lowest \mathcal{H}_∞ -norm was found to be 0.833, which is the same as in the previous case. The controller parameters found for the implemented controller are $K_p = 0.528$, $K_i = 0.158$ and $K_{D_p} = 0.159$ for case 2a.

The resulting performance will be discussed in the following itemization. Firstly, analyzing the resulting sensitivity function $S_{w_1 \rightarrow \Delta\Omega_r}$. Thereafter, the influence of the active tower damper on the closed-loop system is discussed.

- Figure 6-2a shows the resulting sensitivity functions (Case 1, 2) and the inverse of the performance weight, from which it can be seen that the sensitivity function remains below this weight. By comparing case 1 and case 2a with one another, the small pit at the first eigenfrequency (1.33 [rad/s]) is striking. This pit originates from the interaction between the tower feedback loop and the rotor speed controller. That is the reason why the pit is centred at the first tower bending mode. Moreover, the band-pass filter influences the size of the pit through the damping value of ζ . The damping should stay in the bounds of $0 < \zeta < 1$, for which a larger damping value means a larger width of the dip. Therefore, the active tower control-loop only operates in a region around the placed frequency. By looking at the step response depicted in Figure 6-2b. The multi-variable approach of case 2a has a higher settling time of 15.1 [s], but lower peak amplitude of 1.09 [rad/s] compared to the previous case. The slightly worse reference tracking abilities pales with respect what is gained at the mitigating of tower top accelerations, as will be explained next. Furthermore, the lower peak responses are noticed for case 2b and 2c, respectively 1.07 [rad/s] and 1.05 [rad/s]. The settling time for both cases (2b and 2c) are higher with 13.6 [s] and 19.2 [s] as well. This implies that these rotor speed controllers are less aggressive than case 1. As a consequence, the induced loads due to aggressive pitching are reduced for these cases.
- Figure 6-3a shows the inverse weight W_{k, \ddot{y}_t} along with the open-loop system $G_{w_2 \rightarrow \ddot{y}_t}$ and the closed-loop system incorporating the proposed ATD. It can be seen, that using a band-pass filter and a single control gain K_{D_p} does the job perfectly of increasing the damping in the fore-aft direction. The closed-loop function remains below the inverse weight function, and the resulting attenuation of the peak is visible. Figure 6-3b shows the response of the tower top acceleration by a step input. It can be concluded that the implemented technique is capable of increasing the tower damping substantially. For the closed-loop system, the settling time equals 17.2 [s] with a maximal amplitude of 0.677 [m/s^2].

Hence, all the characteristics and values are summarized in the upcoming Section 6-4. This controller approach is verified in the high-fidelity BHAWC model as well.

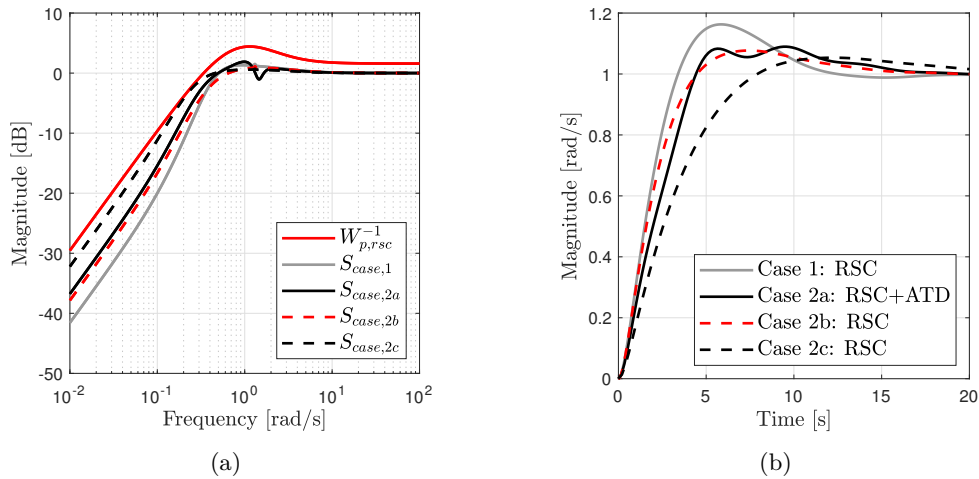


Figure 6-2: (a) bode magnitude plots of the sensitivity function for case 1 (—) and the sensitivity function obtained with the multi-variable problem (—) is shown. The inverse of the performance weight $W_{p,cpc}^{-1}$ (—) is shown as well. (b) step responses from the pitch angle to the rotor speed for both case 1 (—) and case 2 are depicted.

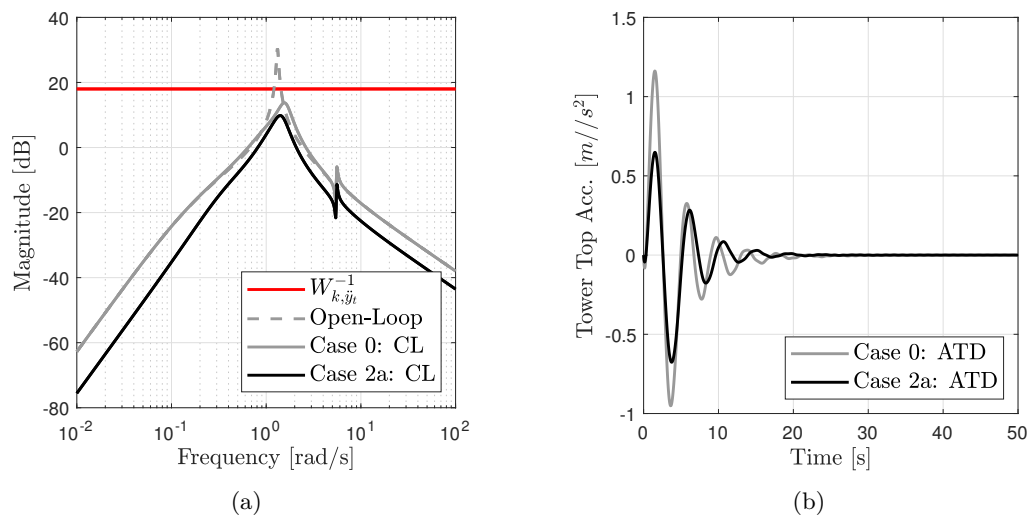


Figure 6-3: (a) bode magnitude plot of the tower control loop, the open-loop (—) versus closed-loop system (—) is given. The inverse weight $W_{k,yt}^{-1}$ (—) is shown as well. (b) step response of an additional pitch actuation to the tower top acceleration, the initial ATD (—) versus case 2a (—) is depicted.

The next step is to investigate the influence of including structural optimization into the controller design synthesis.

6-3 Case 3: Controller Structure Optimization

In this section, the results of the controller structure optimization will be discussed. The generalized configuration of Figure 5-14 is used for this design case. Recall from Chapter 5, that two design cases are proposed. Case 3b includes weight on the tower top accelerations, the rotor speed disturbance forces a tower top acceleration, and therefore the controller is obliged to change the gains. In comparison to case 3a, the additional weight to the \mathcal{H}_∞ -norm reduction will narrow the solution space. It is expected that the controller gains of the designed RSC for case 3b will be lower than case 3a. The resulting optimization for case 3 is repeated below:

$$\begin{aligned} \min_{s.t.} \quad & \gamma \\ & |\Delta t_1| < 1 \cdot 10^{-2}, \quad |\Delta t_2| < 1 \cdot 10^{-2} \\ & \left\| \begin{array}{l} W_{p,rsc} S_{w_1 \rightarrow \Delta \Omega_r} \\ W_{k,\ddot{y}_t} G_{w_1 \rightarrow \ddot{y}_t} \\ W_{p,\Delta t_1} G_{w_1 \rightarrow \eta_1 + \Delta t_1 \eta_1} \\ W_{p,\Delta t_2} G_{w_1 \rightarrow \eta_2 + \Delta t_2 \eta_2} \end{array} \right\|_\infty < \gamma \end{aligned} \quad (6-3)$$

In the upcoming sections, the results of case 3a and case 3b are presented. Thereafter, the grid search results are shown for varying wall thickness weights.

Results case 3a

The problem statement of Equation (6-3) allows for simultaneously changing the controller and support structure design of the extended wind turbine system. It should be mentioned that the weight design for the wall thickness is troublesome. The natural behavior of the system is to decrease the wall thickness for Δt_1 and increase the Δt_2 . This is due to the eigenfrequency sensitivity correlations, for which the former is negative, and the latter is positive. Therefore, the weights are tuned in order to obtain a mass minimization. The weights are stated in Table 5-5. At the same time, the \mathcal{H}_∞ -norm should not differ from the other design cases.

Figure 6-4 depicts the results for respective, the sensitivity function of the RSC design and the wall thickness perturbations functions. The solution which resulted in the lowest \mathcal{H}_∞ -norm of 0.833 is provided by the controller parameters $K_p = 0.649$ and $K_i = 0.255$. Simultaneously the structural perturbations are found to be $\Delta t_1 = -5 \cdot 10^{-4}$ [m] and $\Delta t_2 = -1.7 \cdot 10^{-3}$ [m]. The wall thickness reduction leads to a mass reduction of $12.1 \cdot 10^3$ [kg] of the selected tower sections. The change of the wall thickness shift the pole-zero locations of the system. As a consequence, the eigenfrequencies of the system change as well. This modified eigenfrequency can be noticed in Figure 6-4b, where the resonance peak of $S_{case,3a}$ is slightly different concerning the initial system. The resulting performance will be discussed in the following summation. Firstly, the overall performance of the sensitivity function is discussed. Thereafter, the wall thickness perturbations are presented.

- Figure 6-4a shows the resulting sensitivity function along with the sensitivity function from case 1. The resulting function stays below the imposed bound of the inverse

performance weight. It can be seen that the eigenfrequency is shifted from $\omega_{1,case1} = 1.33$ [rad/s] to $\omega_{1,case2} = 1.34$ [rad/s]. Furthermore, due to the lower K_i gain for this case 3a, the cross-over frequency is slightly higher and the resonance peak is lower than for case 1. This results in a lower peak response and higher settling time, as shown in Figure 6-4c. The closed-loop system achieves nominal performance $\gamma = 0.833$, which is the same for the other cases. Hence, the structure and controller can be simultaneously varied, and subsequently, nominal performance is still guaranteed.

- Figure 6-5a and Figure 6-5b show by bounding the transfer functions $G_{w_1 \rightarrow \eta_1 + \Delta t_1 \eta_1}$ and $G_{w_1 \rightarrow \eta_2 + \Delta t_2 \eta_2}$ results in a change in wall thickness. By comparing the original extended transfer function with the perturbed function $G_{w_1 \rightarrow \eta_1 + \Delta t_1 \eta_1}$, the influence of the decrease in wall thickness Δt_1 is visualized. The same method is used for a decrease of Δt_2 . The wall thickness reduction leads to a newly updated tower section, which has a mass reduction of $12.1 \cdot 10^3$ [kg]. For simplicity, the two perturbations are summed in order to simplify the overall minimization of the wall thickness ($\Delta t_1 + \Delta t_2$). It was found that a larger thickness reduction was rather difficult to obtain by manually tuning the weight. It was noticed by increasing the weights on the wall thickness channels, the performance criteria $\gamma < 1$ was no longer guaranteed.

The next step is to investigate the behavior of the wall thickness reduction by introducing an additional weight on the tower top accelerations.

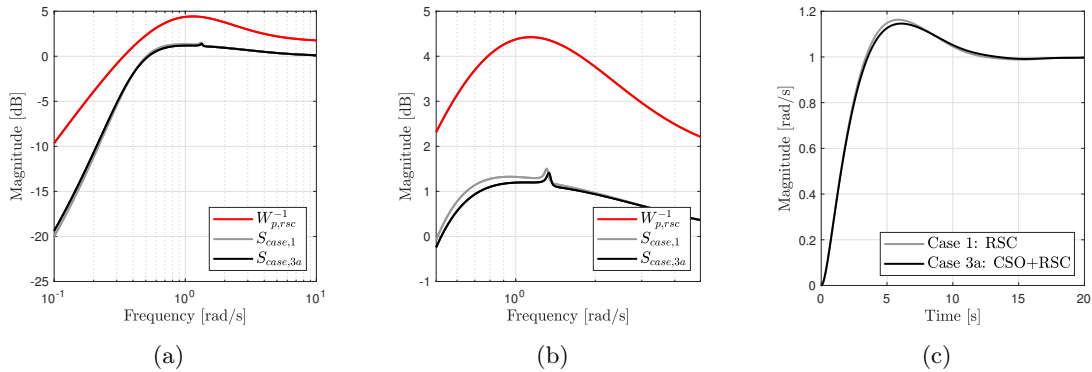


Figure 6-4: (a) bode magnitude plots of the sensitivity plot of case 1 (—) and the sensitivity obtained from the CSO (—) is shown. The inverse of the performance weight (—) is shown as well. (b) the zoomed magnitude plot. (c) the step response of case 1 versus case 3a is shown.

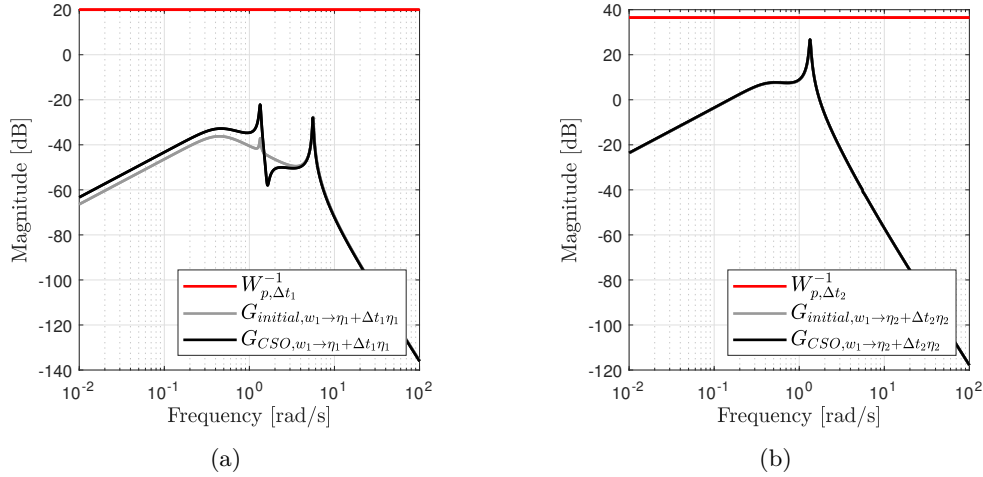


Figure 6-5: Bode magnitude plots for the perturbations channels are shown (a,b). The inverse weighting function of the static gain is shown as well.

Results case 3b

In the previous case, it is shown that by including suitable weights on the wall thickness channels in the \mathcal{H}_∞ -problem formulation, the CSO is able to redesign the controller and structural parameters simultaneously. For this subcase, an additional weight is introduced on the tower top accelerations.

The resulting behavior of this CSO case is depicted in Section 6-3 and the corresponding wall thickness perturbations are shown in Figure 6-7. The \mathcal{H}_∞ -norm is not affected by the additional requirement, namely the lowest norm found is 0.833. Consequently, the obtained controller and structural gains are different. For the RSC, the following control gains are obtained, $K_p = 0.567$ and $K_i = 0.215$. These gains are lower than for case 3a, therefore will be less aggressive in pitching. Subsequently, the obtained wall thickness reduction is $\Delta t_1 = -2 \cdot 10^{-4}$ [m] and $\Delta t_2 = -1.5 \cdot 10^{-3}$ [m]. This leads to mass reduction of $10.2 \cdot 10^3$ [kg] for the selected tower elements. The resulting performance will be discussed in the following bullet points:

- The resulting sensitivity function is affected by the additional constraint compared to case 1 and case 3b, as shown in Section 6-3a/b. It can be seen that the updated eigenfrequency resembles the same shift as for case 3a to the right ($\omega_{1,case3b} = 1.34$ [rad/s]). Furthermore, it is noticed that the crossover-frequency is a lower for case 3b. As a consequence, the step response in Section 6-3c shows that the settling time of case 3b is higher than case 3a. Moreover, the peak response is lower as well. This implies that the obtained controller is less aggressive than case 3a.
- The mass reduction is $1.9 \cdot 10^3$ [kg] less than compared to case 3a. Figure 6-7 shows the transfer relations for the wall thickness perturbations. By taking the tower top accelerations into account for the CSO, the wall thickness reduction is less.

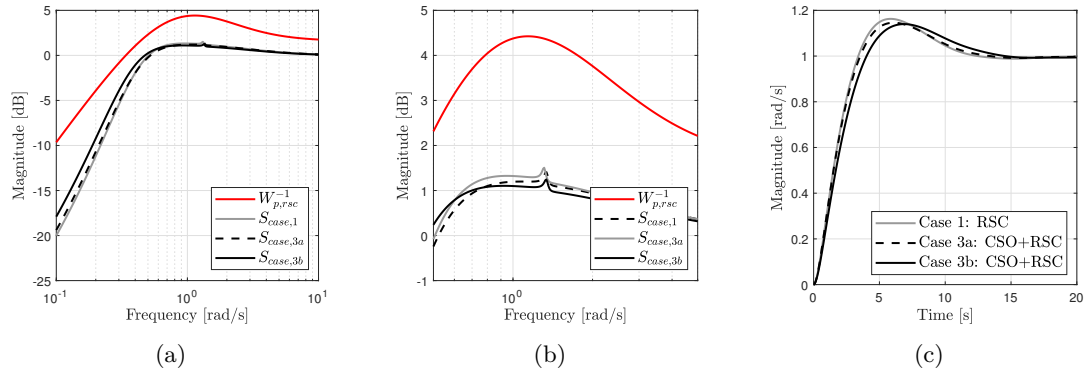


Figure 6-6: (a) bode magnitude plots of the sensitivity plot of case 1 (—) and the sensitivity obtained from the CSO case 3b (—) is shown. The inverse of the performance weight (—) is shown as well. (b) the zoomed magnitude plot. (c) the step-response of case 3b versus the previous cases is shown.

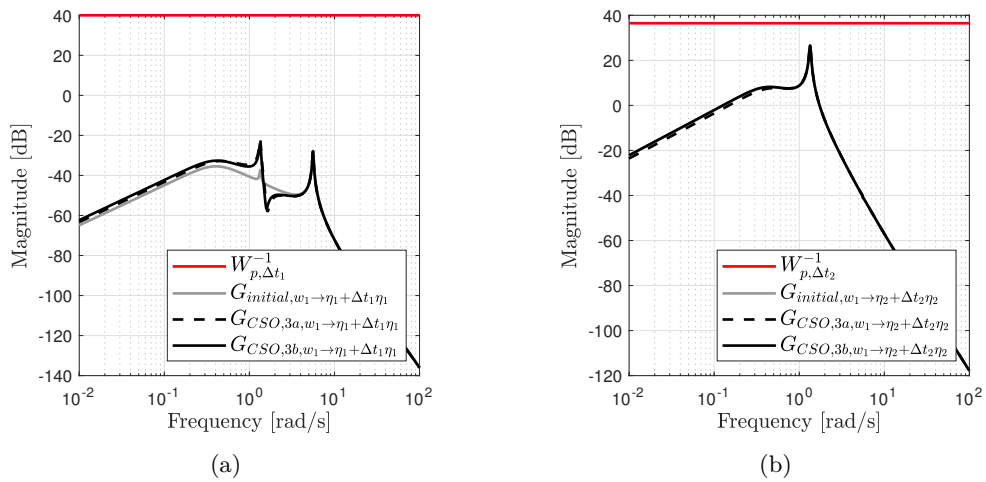


Figure 6-7: Bode magnitude plots for the perturbations channels are shown (a,b), the inverse weighting function of the static gain is shown as well.

Grid search for wall thickness weights

It was found that tuning the wall thickness weights W_{p,Δ_1} and W_{p,Δ_2} without affecting the performance was somewhat troublesome. In order to show the behavior of tuning the weights on the wall thickness parameters, a grid search is performed. The weights are varied in the following step:

- Weight on Δt_1 is $W_{p,\Delta t_1} = [0.01 : 0.02 : 2]$
- Weight on Δt_2 is $W_{p,\Delta t_2} = [0.001 : 0.001 : 0.1]$

The optimization problem, as proposed in Equation (5-19), is executed by fixing the controller gains. The results of changing the weights on the performance index γ is shown Figure 6-8a. In Figure 6-8b, the summation of the wall thickness over the two tower sections is shown for various weights on the perturbation channels. It can be seen that the correlations of the different weights are of influence on the overall wall thickness reduction. When the weights on both the function are zero, no wall thickness reduction is noticeable. Still, the performance is below $\gamma < 1$, due to the controller gains. By increasing the weight on $W_{p,\Delta t_1}$, the wall thickness is reduced. However, by increasing the weight on $W_{p,\Delta t_2}$ results in an opposite effect, as shown Figure 6-8c/d. Higher values increase the overall wall thickness for $W_{p,\Delta t_2}$. This can be explained by the correlations of the eigenfrequencies of the tower sections, which are opposite in magnitude. Therefore, the wall thickness perturbations interact with one another.

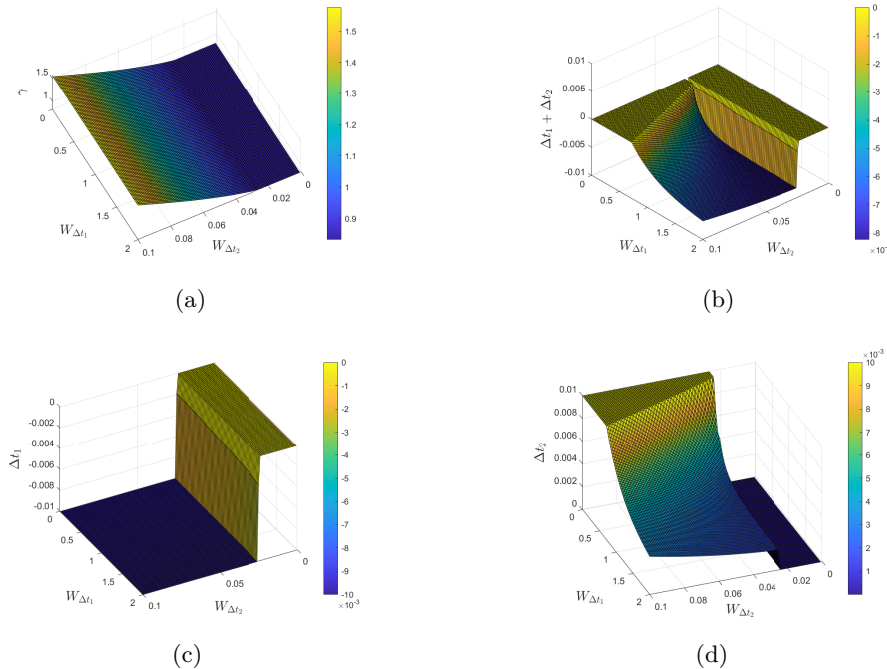


Figure 6-8: (a) surface plot is shown of the resulting γ values for varying the weights $W_{p,\Delta t_1}$ and $W_{p,\Delta t_2}$. (b) surface plot is shown for the summation of $\Delta t_1 + \Delta t_2$ for various weights. (c) and (d) are the surface plots of the individual wall thickness perturbations

6-4 Summary of the cases

In this section, the results of the different design cases are briefly summarized. All the optimized parameters are presented in Table 6-1. Notice, for all these cases closed-loop performance is guaranteed. It was found that implementing the controller of case 2 in the BHAWC model leads to an unstable system. This is due to the fixed gain K_{D_p} , which resulted into infeasible high pitch actuation. The reason for this is the underestimation of the aerodynamic damping in the linear model. As a consequence, the gain K_{D_p} is overestimated. Therefore, two different cases for incorporating the attenuation of the tower accelerations in the RSC design are performed. This is done by using the Equation (5-19) and excluding the structural deformations. The weight on the tower top acceleration is initialized with 0.01 and 0.05, for respectively case 2b and case 2c.

Furthermore, looking at the values of the gains of the designed RSC for case 1 and 2. It can be seen that by taking the tower top accelerations in account, the resulting controller gains are relaxed. This relaxation is as expected, because more aggressive control gains are good for fast rotor speed control. However, it increases the movement of the tower top. Comparing the CSO cases with the results of the nominal case 1, it can be seen that the controller gains are not really different. This is due to the reduction of the wall thickness, which lead to slightly different pole-zero locations of the closed-loop system. The CSO cases compensate for this shift ,through changing the controller gains of the RSC design. Therefore, the CSO is proven to be effective in addressing multiple design criteria. By changing the weights in frequency domain, the criteria of the designer can be met.

Table 6-1: Summary of the different design cases throughout this chapter

Parameter	Case 1	Case 2a	Case 2b	Case 2c	Case 3a	Case 3b
K_p	0.646	0.528	0.659	0.384	0.650	0.567
K_i	0.275	0.158	0.179	0.0935	0.255	0.215
K_{D_p}	-	0.159	-	-	-	-
Δt_1 [m]	-	-	-	-	$-5 \cdot 10^{-4}$	$-2 \cdot 10^{-4}$
Δt_2 [m]	-	-	-	-	$-1.7 \cdot 10^{-3}$	$-1.5 \cdot 10^{-3}$
Mass reduction [kg]	-	-	-	-	$12.1 \cdot 10^3$	$10.2 \cdot 10^3$
γ	0.833	0.833	0.833	0.833	0.833	0.833
ω_1 [rad/s]	1.33	1.33	1.33	1.33	1.34	1.34
ω_2 [rad/s]	5.55	5.55	5.55	5.55	5.58	5.59

6-5 Verification with nonlinear simulations

For verification of the control design of the different cases in Chapter 5, nonlinear high-fidelity have been carried out for validation purposes. The nonlinear simulations are done with in-house wind turbine simulation tool of Siemens Gamesa Renewable Energy (SGRE) called BHAWC. It includes a structural dynamics module based on the same finite element method approach as explained in Chapter 4. The aerodynamics are modeled based on a state-of-the-art Blade-Element-Momentum theory. Due to the simplicity of the linear model used for the controller synthesis in this work, it should be mentioned that the high-fidelity model includes additional filters in the RSC-loop. These filters are the following:

- Notch filters: one placed on the tower frequency, one on the blade passing frequency (3P) and one placed on edgewise synchronous and drive-train frequencies of the wind turbine.
- Low-pass filter: to remove the high frequency noise.

It is assumed that these filters do not interfere with the derived controllers from this chapter. The filters are placed before the measured speed enter the PI-controller. Since all of the verified cases will include these filters, they can be compared with one another. The simulation is based on the following set-up. A mean wind speed of 18 [m/s] with a turbulence intensity of 10%. The proposed above-rated wind speed will lead to considerable deviations from the steady-state operating point of 18 [m/s] for the wind turbine model. A single turbulence seed with a duration of 600 [s] is simulated. The effectiveness of the proposed controller is measured by looking at the driving factors. Firstly, it is interesting to look at the rotor speed deviations and the corresponding collective pitch actuation. Secondly, the bending moment at tower bottom $M_{fa,b}$ and tower top $M_{fa,t}$ are analysed. This is done in order to see whether the controllers are mitigating the loads of the tower. Finally, the pitch bearing damage is the last driving factor of interest. This is a combination of the edgewise and flap-wise moment at the blade root combined with the total pitch traveled. The following cases are simulated and compared:

- Case 1: the rotor speed controller with nominal performance will serve as a benchmark. For this control-loop, the measured rotor speed should track the reference rotor speed of 10.8 [rpm] while suppressing the disturbance introduced by the wind.
- Case 2(b/c): the derived rotor speed controller with a weight on the tower top accelerations \ddot{y}_t . The weight W_{k,\ddot{y}_t} is respectively 0.01 and 0.05. Resulting in different controller gains for the RSC. The separate ATD control-loop (case 2a) was simulated as well. However, due to the fixed gain K_{D_p} and band-pass filter the simulations went unstable. This is due to the underestimated aerodynamic damping in the derived wind turbine model. This underestimation causes a higher obtained damping value for K_{D_p} .
- Case 3(a/b): the tower is updated with the proposed wall thickness reduction within the BHAWC model. The model is simulated with the found control gains of respectively case 3a and case 3b.
- Case 0: the initial controller design for the RSC through loop-shaping.

The results of the time-simulation is only presented for the first 200 [s]. Figure 6-9 shows the time-domain simulation for the RSC design in gray (Case 1) and the load reducing RSC design from case 2b in black. What can be noticed from Figure 6-9c, that case 1 has more oscillating pitch deflections then case 2b. This leads in less rotor speed deviations as shown in Figure 6-9b for case 2b. As a consequence, the tower bottom moment has lower deviations due to the slower pitch actuation for case 2b then for case 1. This is in line with the expectation, that the control objectives of speed tracking and reducing loads conflict with one another. By taking the tower top accelerations into account for the controller design of the RSC it is possible to reduce the loads, and subsequently, relax the importance of the rotor speed tracking objective.

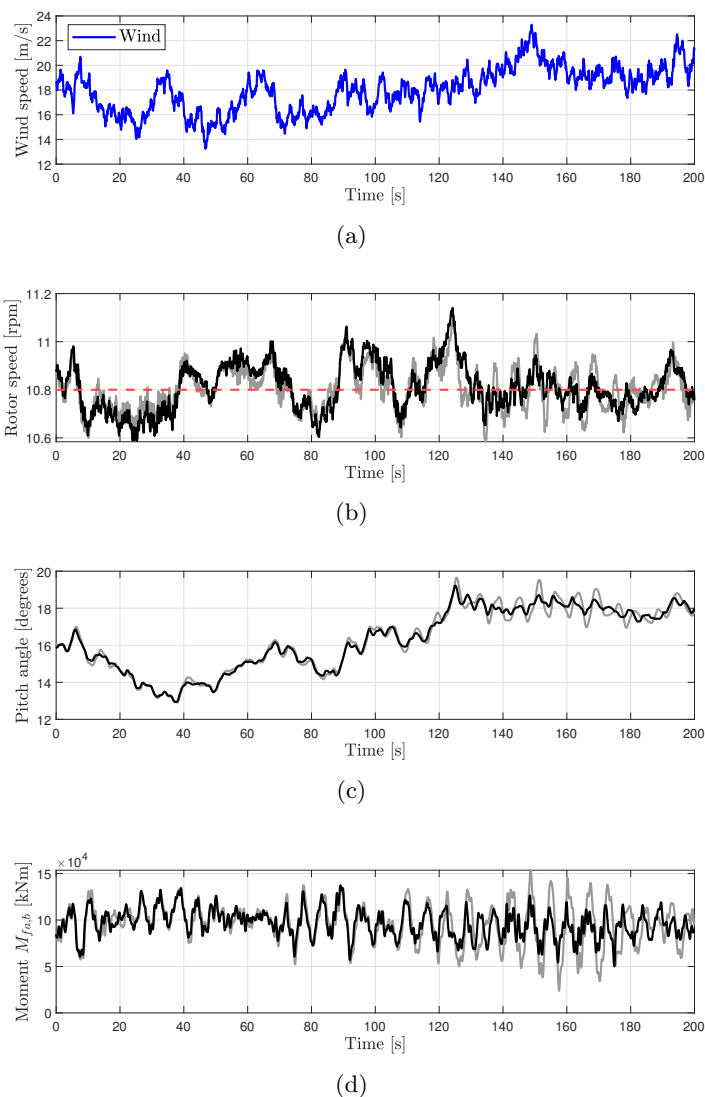


Figure 6-9: Time domain simulation of applying a mean wind speed of 18 m/s with a turbulence intensity of 10%. The rated rotor speed is given by 10.8 [rpm] (---). Controller design case 1 (—) and controller design case 2b (—) are shown.

Comparison of the verification

In order to compare the relevant effects on the driving factors the full 600 [s] spectrum of the simulations are used. From these simulations, a fatigue analysis is performed by means of rainflow counting, for respectively the support structure and the pitch bearings. The method of calculating the fatigue from time-domain simulations is shown in Appendix C. The resulting damage is shown in Figure 6-10 for the design cases. The overall comparison is given by Table 6-2. It is seen that for the load reducing controllers of case 2b/c the tower moments are lower, due to the lower pitch activity. This results in less sudden deviations of the aerodynamic thrust exerting on the tower top, and therefore a less aggressive RSC design. For the cases including the structural optimization (case 3a/b), it can be seen that the loads are higher for the tower moments. This implies that for future work, it is interesting to see whether a load analysis of the tower can be included in the optimization. The design case 1 has the best rotor speed tracking abilities. By introducing multiple objectives, this is relaxed and it is possible to reduce the loads by introducing a weight on the tower top accelerations. For the CSO case (3b) which includes the weight on tower top accelerations, it can be seen that the loads for tower bottom can be reduced. However, the tower top bottom moment has higher damage, due to the wall thickness reduction, a more flexible tower is obtained.

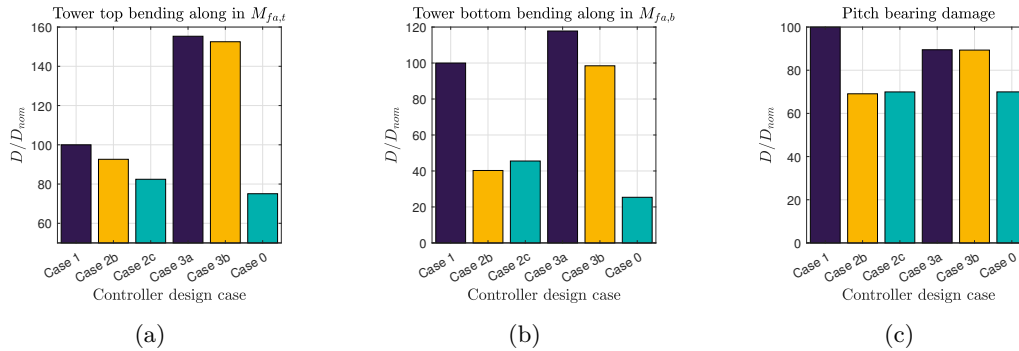


Figure 6-10: Calculated damage for the tower top moment (a), the tower bottom moment (b) and pitch bearing damage (c) for the different control designs.

Table 6-2: Comparison of the different control design cases simulated with the high-fidelity 8.0MW BHAWC model normalized with respect to case 1.

Specification	Case 1	Case 2b	Case 2c	Case 3a	Case 3b	Case 0
Max(Ω_r) [rpm]	1.0	+0.30%	+0.49%	-0.01%	+0.02%	+0.28%
Standard deviation Ω_r [rpm]	1.0	+14%	+20%	+1.0 %	+2.0 %	+13 %
Tower top bending along DEL [·]	1.0	-7.0%	-18%	+55 %	+52%	-25%
Tower bottom bending along DEL [·]	1.0	-60 %	-54%	+18%	-2.1%	-75%
Pitch bearing damage [·]	1.0	-31%	-30%	-11%	-11%	-30%
Pitch travel [·]	1.0	-26%	-27%	-8.0%	-12 %	-25%

6-6 Conclusion

The main goal of this chapter is as follows:

"Apply the controller-structure optimization to prove its effectiveness on the linear 8.0MW SGRE wind turbine model, while achieving wall thickness reduction and rotor tracking performance"

For proving the effectiveness of the proposed method, three different cases were presented, which addressed different controller or structure design scenarios. For each design case, a \mathcal{H}_∞ -norm minimization was formulated while using weights on different performance channels. By doing so, a rotor speed controller with satisfactory behavior is derived and the structural design of the wind turbine is altered while keeping the overall performance index γ constant. The cases are summarized as follows:

- The designed RSC through \mathcal{H}_∞ -norm reduction can meet the rotor tracking abilities. In the verification study, the rotor tracking abilities surpass the other cases. However, the higher loading is inevitable due to the more aggressive pitch controller gains.
- For the designed RSC with load reducing components, a decrease in the loads of the previous item is observed. It is concluded that by implementing a weight on the tower top accelerations, the capability of lowering the obtained controller gains. Consequently, the fatigue of the tower is reduced over time.
- The extended system description is used for the CSO case. It used bounds on the following transfer relations $G_{w_1 \rightarrow \eta_1 + \Delta t_1 \eta_1}$ and $G_{w_2 \rightarrow \eta_2 + \Delta t_2 \eta_2}$ by a static weight $W_{p, \Delta t_1}$ and $W_{p, \Delta t_2}$, forcing the wall thickness to change. The weights are used in combination with the performance weight on the sensitivity function. This resulted in simultaneously varying the controller and the structural design of the wind turbine model. The weights on the perturbation channels are tuned in such a way an effective mass reduction was achieved of $10.2 \cdot 10^3$ [kg] for the best performing case.

It was found by tuning the weights of the wall thickness perturbations. Then, different values for the wall thickness reduction were obtained. Therefore, a grid search is performed with varying the weights on the wall thickness perturbations. It was noticed by taking high weights the nominal performance ($\gamma < 1$) was not guaranteed anymore. Hence, this limits the design freedom for structural optimization.

Conclusions and Recommendations

This chapter will present the conclusions on the research objectives presented in Chapter 1. Furthermore, the recommendations for future work are provided based on the conclusions and the assumptions made throughout this thesis.

7-1 Conclusion

In order to reduce the Levelized Costs of Energy for Offshore Wind Turbine (OWT), the design of the offshore turbines should be further optimized. A large improvement can be obtained by looking at the design cycle of the wind turbine. Multiple teams of different disciplines are involved by designing an OWT each having their own design criteria. This can lead to conflicting criteria between the different teams, and therefore iteratively switching the designs. This results in a time-consuming design cycle. Therefore, it is vital to seek other methods of integrating the design criteria in one optimization routine.

Therefore, a framework is proposed for combining the objectives of the controller with the structural design. The goal of this thesis is formulated by the following main objective of this work:

"The main objective is to simultaneously optimize the integral support structure design and controller design for large scale offshore wind turbines."

This main objective can be divided into two parts, namely finding a suitable Controller Structure Optimization (CSO) method and the modelling of a large scale offshore wind turbine model. For the CSO, there are two effective ways of simultaneously designing the controller and the structure. These are the nested and direct design method. In Chapter 2, the use of direct design is suggested. The proposed CSO method makes use of nonsmooth \mathcal{H}_∞ synthesis with fixed-structured controllers. Through this method, tunable parameters of the system can be extracted for using them as input to the system description. The tunable parameters are

the structural parameters of the system. As a consequence, the tunable parameters are computed as perturbation and added to the controller block diagonal. The controller is designed by using the *Robust Control Toolbox* of *MATLAB*. The method provides an insightful and simple approach of including the structural parameters in a minimization of the closed-loop system performance using a performance weight on the sensitivity function.

In order to extract the tunable parameters, the system description makes use of a parameter-dependent state-space model. This is obtained by recasting the structural matrices from an Ordinary Differential Equation (ODE) into state-space form. This extraction is illustrated in Chapter 3. The structural parameters are extracted by making the system description linearly dependent on these parameters. Therefore, the overall structural change can be forced by perturbations (additional inputs). Furthermore, it is shown that the method works with model reduction methods. Therefore, the most dominant dynamics are preserved while reducing the order of the system. The proposed method for CSO is verified with a simple two-Degrees of Freedom (DoF) mass-spring-damper system. The eigenfrequencies were changed by forcing the system's mass and stiffness to alter. This was done by bounding the resonance peak of the sensitivity function by a performance weight. It was assumed that the coupling of the mass and stiffness resembles the same coupling for an OWT.

The second part of the main objective is formed by modelling a suitable OWT model for the application of the CSO. In Chapter 4, an OWT model of the 8.0MW Siemens Gamesa Renewable Energy (SGRE) wind turbine is derived. The possibility of extracting the structural parameters of the support structure is included. It was shown that the wall thickness of the tower describes the structural matrices linearly, and therefore is available for the optimization. The mechanical model is reduced for control purposes and coupled with a linearized aerodynamic model. It is shown that the derived model resembles the behavior of the Bonus Horizontal Axis Wind turbine Code (BHAWC) model for the rotor speed to pitch angle and the structural behavior as well. The derived linear 8.0MW wind turbine model is suitable for the CSO application.

The controller design imposed a Rotor Speed Controller (RSC), where the relation from pitch angle to rotor speed was chosen for analysis. Furthermore, it was of interest to seek the boundaries of conflicting objectives, e.g. a load reducing part. The RSC design is initialized by looking at the current design RSC in the BHAWC model in order to avoid extensive controller parameterization. The weight design combines the objectives of adequate rotor tracking abilities and active tower damping. It was found that the proposed multi-objective problem successfully obtains load-reducing controllers with adequate rotor tracking abilities through \mathcal{H}_∞ -norm reduction.

Furthermore, the wind turbine model is extended by using the linear dependency of the wall thickness parameters in the individual elements of the tower. It was found the resulting change in modeshapes bounds the change of the wall thickness parameter. The sensitivity of perturbing the wall thickness per tower element for the eigenfrequencies differ in correlation. Therefore, the tower elements with the same correlations are partitioned together. The wall thickness parameter is used to redesign the system while optimizing the controller parameters of the RSC. This is done by applying weight functions on the perturbation channels, and subsequently, change the overall wall thickness of the tower. Remarkably, the performance

index of the CSO-cases remained unchanged. This implies that for the current 8.0MW turbine, the structural design and controller design can be improved to one another. However, the difficulty of setting the right requirements for the \mathcal{H}_∞ -norm is still unspoken. Finding the correct weighting functions for the desired behavior is quite troublesome. It follows from the grid search that it is possible to tune the weights properly to obtain the highest wall thickness reduction. However, for this analysis, the controller parameters are fixed, and it should be investigated whether these are influenced as well. Finally, it was shown in the verification study, that through the \mathcal{H}_∞ controller design, multiple controllers objectives can be met concerning the driving factors.

Hence, the CSO framework is applicable for large scale wind turbine system. Therefore, the controller and structural can be simultaneously varied.

7-2 Recommendations

Based on the conclusions and the assumptions made in this work, recommendations for future work are presented in this section:

- From the verification study, it is shown that the induced loads for the CSO cases where higher than the other cases. For this design, the weights were placed on the tower top accelerations. It should be investigated whether the weights can be placed on the induced loading. This is to make sure the loads do not exceed critical levels.
- For the redesign of the tower only two tower sections are used. Therefore, two improvements can be achieved. First, multiple tower elements should be included of which the wall thickness is changed. Secondly, allow for more structural parameters to change along the support structure as length and diameter.
- The foundation used for the wind turbine model is monopile based. It would be interesting to look into different support structure models. For example, the design of jackets, these have higher eigenfrequencies and this results in the possibility of achieving a higher controller bandwidth. Therefore, the controllability of the rotor speed problem could be improved.
- It was assumed that the influence of structural changes on the modeshape is not that significant. This was the reason that the structural change remained linear to the original system description. However, when large structural changes are obliged, the updated system may no longer be a valid.
- In this work, the above-rated operating control region is investigated. The derived linear model for the controller synthesis is linearized around one operating wind speed. To incorporate the controllability over different wind speeds, the use of a linear parameter varying system description can be used. Then multiple diagonal controller can be derived simultaneously.
- The resembles between the 8.0MW wind turbine of BHAWC and the derived linear model can be improved. It is recommended to look into the possibility of linearizing the BHAWC model directly.

- The wall thickness is reduced from an existing tower design, which is already optimized for site-specific conditions. It could be interesting to test the wall thickness reduction method for a more conservative designed tower in order to see whether the reduction stays the same.
- The minimization of the wall thickness is done by bounding the modal amplitudes of the wind turbine description. Therefore, the wall thickness change corresponds with a certain structural mode. It could be interesting to look into the possibility of using other signals for the wall thickness reduction.

Appendix A

Preliminaries structural dynamics

This appendix provides the background principles of the structural derivations of the free vibration problem and the sensitivity analysis for respectively the eigenfrequencies and eigenmodes. The method is directly adopted from [Gérardin and Rixen \(2014\)](#).

A-1 Free vibration problem

The free vibration problem is used to determine the eigensolutions and the corresponding eigenfrequencies of the structure. For the free vibration problem it is assumed that the damping can be neglected. Therefore, the Ordinary Differential Equation (ODE) can be expressed as follows:

$$\begin{aligned} M\ddot{x}(t) + Kx(t) &= 0 \\ x(0) = x_0, \dot{x}(0) &= \dot{x}_0 \end{aligned} \tag{A-1}$$

where the solution of the resulting ODE of Equation (A-1) can be given by:

$$x(t) = \phi y(t) \tag{A-2}$$

where ϕ is a free linear mode of displacement and $y(t)$ is a function of time. Now it can be seen, if Equation (A-2) is substituted into Equation (A-1) and rearranged:

$$\left(M \begin{pmatrix} \ddot{y}(t) \\ y(t) \end{pmatrix} + K \right) \phi = 0 \tag{A-3}$$

This above expression holds only when the term $\begin{pmatrix} \ddot{y}(t) \\ y(t) \end{pmatrix}$ remains constant over time. This term can also be expressed or is known as the eigenvalue $-\omega_s^2$. Therefore, Equation (A-3) is equivalent to the solution of the generalized eigenvalue problem. Furthermore, each eigenfrequency and eigenmode can be determined as follows:

$$(-M\omega_s^2 + K)x_s = 0 \tag{A-4}$$

A-2 Eigenfrequency sensitivity

The eigenfrequency sensitivity provides quantitative information regarding the sensitivity of the structural eigenfrequencies to structural perturbations. In this work, it is supposed that the sensitivity relates to one physical design parameter denoted by p and the structural matrices (M, K) are a function of this parameter.

$$K = K(p) \quad M = M(p) \quad (\text{A-5})$$

Then the corresponding derivatives are denoted as:

$$K_p = \frac{\partial K}{\partial p} \quad M_p = \frac{\partial M}{\partial p} \quad (\text{A-6})$$

One can imagine that the eigensolutions and the eigenfrequencies will change by perturbing the parameter. At the same time the equation of calculating the eigensolutions and corresponding eigenfrequencies stays valid:

$$(K - \omega_s^2 M)x_s = 0 \quad (\text{A-7})$$

Therefore, Equation (A-7) is used for deriving the sensitivity with respect to parameter p as follows:

$$\left(\frac{\partial K}{\partial p} - \omega_s^2 \frac{\partial M}{\partial p} \right) x_s - \frac{\partial \omega_s^2}{\partial p} M x_s + (K - \omega_s^2 M) \frac{\partial x_s}{\partial p} = 0 \quad (\text{A-8})$$

By using the notation of Equation (A-6) and project this on the eigensolution x_s . Then Equation (A-8) can be recasted in the following form of Equation (A-9)

$$\frac{\partial \omega_s^2}{\partial p} = \frac{x_s^T (K_p - \omega_s^2 M_p) x_s}{x_s^T M x_s} \quad (\text{A-9})$$

From the above expression the following three things can be stated:

- The derivative of a given eigenvalue with respect to the parameter can be obtained in terms of the corresponding elementary sensitivity matrices since the products $K_p x_s$ and $M_p x_s$ can be performed element-wise.
- The derivative of an eigenvalue depends on the corresponding eigenvalue only.
- An increase of stiffness increases frequency, whereas an increase of mass reduces it. This of course the case for a free vibrations problem.

A-3 Eigenmode sensitivity

The eigenmode sensitivity follows directly from the procedure of calculating the eigenfrequency sensitivity. The first step is to compute the eigenvalue sensitivity $\frac{\partial \omega_s^2}{\partial p}$ presented in previous section (Equation (A-9)). The next step is to solve Equation (A-8) for the $\frac{\partial x_s}{\partial p}$ term as follows:

$$(K - \omega_s^2 M) \frac{\partial x_s}{\partial p} = \left(-K_p + \omega_s^2 M_p + \frac{\partial \omega_s^2}{\partial p} M \right) x_s \quad (\text{A-10})$$

It can be seen that the term $(K - \omega_s^2 M)$ is singular and x_s is the corresponding null-space. Moreover, the $\frac{\partial \omega_s^2}{\partial p}$ can be derived with Equation (A-9) and, subsequently the right hand side of Equation (A-10) is orthogonal to the null-space x_s . Implying that a solution exist. Hence, $(K - \omega_s^2 M)$ can be inverted by a pseudo inverse and it follows that Equation (A-10) can be recasted:

$$\frac{\partial x_s^o}{\partial p} = (K - \omega_s^2 M)^+ \left(-K_p + \omega_s^2 M_p + \frac{\partial \omega_s^2}{\partial p} M \right) x_s \quad (\text{A-11})$$

Thereafter, the general solution for the eigenmode sensitivity is given by:

$$\frac{\partial x_s}{\partial p} = \frac{\partial x_s^o}{\partial p} + x_s \alpha \quad (\text{A-12})$$

where α stands for an arbitrary amplitude. Within this work the arbitrariness is fixed by defining a unique eigenmode sensitivity analysis by linking it to keeping the modal mass constant ($x_s^T(p) M x_s(p) = \mu_s$). Therefore, α can be expressed as:

$$\alpha = -\frac{1}{x_s^T M x_s} \left(\frac{1}{2} x_s^T M_p x_s + x_s^T M \frac{\partial x_s^o}{\partial p} \right) \quad (\text{A-13})$$

The result shows two things:

- Unlike eigenvalue sensitivities, calculating an eigenmode sensitivity implies knowledge of all other eigensolutions.
- The sensitivity of mode x_s strongly depends on other modes having similar eigenfrequency, that is when $\omega_r^2 = \omega_s^2$

Appendix B

Definitions of the 8.0MW SGRE Wind Turbine

The 8.0MW Siemens Gamesa Renewable Energy (SGRE) is a variable-speed variable-pitch and bottom supported monopile offshore wind turbine. Within this thesis, the turbine is modelled as a lumped mass model, for which the blades are not explicitly modelled. The schematic overview of the lumped mass wind turbine model is depicted in Figure B-1. The numerical values for the wall thickness and radius along the tower is given in Figure B-2a and Figure B-2b, respectively. These parameters are used with the corresponding Euler-Bernoulli beam matrices.

The following tables offers the main specifications for the 8.0MW SGRE wind turbine subsystems in accordance with the presented information in Chapter 4. With the use of this information and the presented modeling principles in Chapter 4, the same mechanical subsystem can be derived.

Euler-Bernoulli beam

The tower model is represented by a total number of 40 beam elements because the provided specification on the dimension of the tower model consisted out 40 evenly distributed elements.

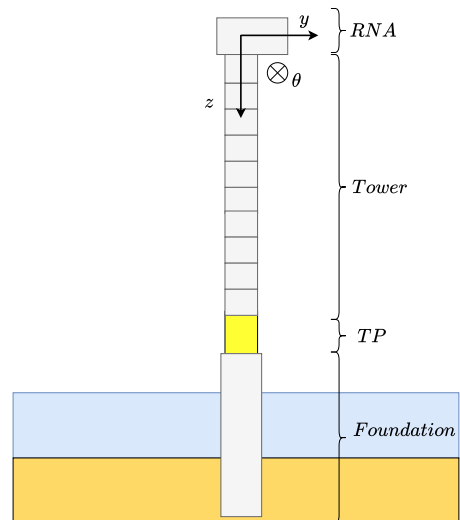


Figure B-1: Schematic representation of a lumped mass model of the 8.0MW SGRE wind turbine with corresponding coordinates.

For each single beam element the nodes are defined as $x = [u_{z_1} \ u_{y_1} \ \theta_1 \ u_{z_2} \ u_{y_2} \ \theta_2]^T$. These coordinates are related to the transnational directions in z and y of the turbine model presented in Appendix B. The formulation for the mass and stiffness matrices are respectively:

$$K = \left[\begin{array}{ccc|ccc} \frac{EA}{L_e} & 0 & 0 & -\frac{EA}{L_e} & 0 & 0 \\ 0 & \frac{12EI}{L_e^3} & \frac{6EI}{L_e^2} & 0 & -\frac{12EI}{L_e^3} & \frac{6EI}{L_e^2} \\ 0 & \frac{6EI}{L_e^2} & \frac{4EI}{L_e} & 0 & -\frac{6EI}{L_e^2} & \frac{2EI}{L_e} \\ \hline -\frac{EA}{L_e} & 0 & 0 & \frac{EA}{L_e} & 0 & 0 \\ 0 & -\frac{12EI}{L_e^3} & -\frac{6EI}{L_e^2} & 0 & \frac{12EI}{L_e^3} & -\frac{6EI}{L_e^2} \\ 0 & \frac{6EI}{L_e^2} & \frac{2EI}{L_e} & 0 & -\frac{6EI}{L_e^2} & \frac{4EI}{L_e} \end{array} \right] = \left[\begin{array}{c|c} K_{11}^e & K_{12}^e \\ \hline K_{21}^e & K_{22}^e \end{array} \right] \quad (\text{B-1})$$

$$M = \frac{\rho A L_e}{420} \left[\begin{array}{ccc|ccc} 140 & 0 & 0 & 70 & 0 & 0 \\ 0 & 156 & 22L_e & 0 & 54 & -13L_e \\ 0 & 22L_e & 4L_e^2 & 0 & 13L_e & -3L_e^2 \\ \hline 70 & 0 & 0 & 140 & 0 & 0 \\ 0 & 54 & 13L_e & 0 & 156 & -22L_e \\ 0 & -13L_e & -3L_e^2 & 0 & -22L_e & 4L_e^2 \end{array} \right] = \left[\begin{array}{c|c} M_{11}^e & M_{12}^e \\ \hline M_{21}^e & M_{22}^e \end{array} \right] \quad (\text{B-2})$$

The notation and partitioning of matrices in elements as M_{ij}^e and K_{ij}^e is used for coupling the shells together. Furthermore, the superscript e stands for the number of shell element used in the overall tower structure. The i and j corresponds to the node positions within each shell element. To be more precise, each shell element is formed by two consecutive nodes within the overall tower structure.

Subsequently, the linear parameter dependency of wall thickness in both the mass and stiffness matrix can be shown for the Equation (B-2), Equation (B-1). For the application of the Controller Structure Optimization (CSO), the resulting tower model should be susceptible for wall thickness perturbations. In order to show the principle, the thin walled cylinder expressions as stated in Table 4-1 are substituted into the structural matrices.

- Stiffness matrix: For thin walled cylinders, the second moment of inertia I_z and cross sectional area A are both linearly dependent on the wall thickness parameter. Looking at the Euler-Bernoulli stiffness matrix, it can be noticed that each matrix entry is linear in either A or I_z as well. For the Euler-Bernoulli beam, the resulting stiffness matrix of Equation (B-1) is recasted to show the linear dependency of the wall thickness for all matrix entries:

$$K(t) = \left[\begin{array}{ccc|ccc} \frac{2\pi r E}{L_e} & 0 & 0 & -\frac{2\pi r E}{L_e} & 0 & 0 \\ 0 & \frac{12E\pi r^3}{L_e^3} & \frac{6E\pi r^3}{L_e^2} & 0 & -\frac{12E\pi r^3}{L_e^3} & \frac{6E\pi r^3}{L_e^2} \\ 0 & \frac{6E\pi r^3}{L_e^2} & \frac{4E\pi r^3}{L_e} & 0 & -\frac{6E\pi r^3}{L_e^2} & \frac{2E\pi r^3}{L_e} \\ \hline -\frac{2\pi r E}{L_e} & 0 & 0 & \frac{2\pi r E}{L_e} & 0 & 0 \\ 0 & -\frac{12E\pi r^3}{L_e^3} & -\frac{6E\pi r^3}{L_e^2} & 0 & \frac{12E\pi r^3}{L_e^3} & -\frac{6E\pi r^3}{L_e^2} \\ 0 & \frac{6E\pi r^3}{L_e^2} & \frac{2E\pi r^3}{L_e} & 0 & -\frac{6E\pi r^3}{L_e^2} & \frac{4E\pi r^3}{L_e} \end{array} \right] t \quad (\text{B-3})$$

- Mass matrix: In this case the wall thickness dependency is only present in the cross sectional area A the element. Following the same reasoning as for the stiffness matrix,

Equation (B-2) is rewritten in order to visualize the linear dependency for the wall thickness parameter.

$$M(t) = \frac{\rho\pi rLt}{840} \begin{bmatrix} 140 & 0 & 0 & 70 & 0 & 0 \\ 0 & 156 & 22L_e & 0 & 54 & -13L_e \\ 0 & 22L_e & 4L_e^2 & 0 & 13L_e & -3L_e^2 \\ 70 & 0 & 0 & 140 & 0 & 0 \\ 0 & 54 & 13L_e & 0 & 156 & -22L_e \\ 0 & -13L_e & -3L_e^2 & 0 & -22L_e & 4L_e^2 \end{bmatrix} \quad (\text{B-4})$$

Hence, for thin walled cylinders, the structural matrices are linearly dependent on the wall thickness parameter. Recall from Chapter 2 that with the above stated matrices, the tower model can be parameterized through the wall thickness. Since the above matrices in only describe a single beam element, the mass and stiffness matrices of all 40 shell elements should be coupled in order to form the total tower structure.

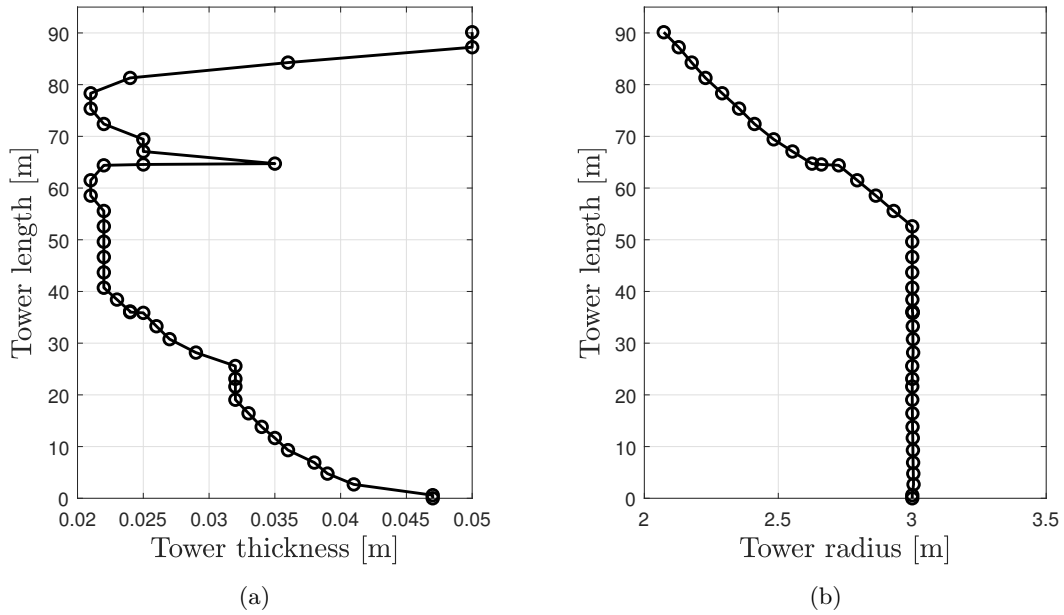


Figure B-2: The element-wise thickness along the tower length (a) and the element-wise radius along the tower length (b).

Table B-1: Numerical values for the RNA of the 8.0MW SGRE wind turbine.

	Symbolic expression	Numerical Value
Rotor Inertia	J_r	109687930 [$kg \cdot m^2$]
Rotor-Nacelle-Assembly mass	m_{RNA}	449300 [kg]
Offset of RNA mass in z-direction	$z_{\Delta cog}$	-1.89 [m]
Pitch delay	τ	0.3 [s]

Table B-2: Element values and characteristics for the Euler-Bernoulli beam theory for the 8.0MW SGRE wind turbine.

Beam element parameters	Symbolic expression	Numerical Value
Density	ρ	7850 [kg/m^3]
Young Modulus	E	210 [GPa]
Poisson ratio	ν	0.3
Length of element	L_e	– [m]
Wall thickness	t	– [m]
Radius element	r	– [m]
Timoshenko shear coefficient	k_y	2

Table B-3: Operating characteristics for the 8.0MW SGRE wind turbine

Operation characteristics	Symbolic expression	Numerical Value
Rated rotor speed	$\Omega_{r,rated}$	10.8 [rpm]
Rated wind speed	V_{rated}	12 [m/s]
Cut-In wind speed	$V_{cut,in}$	3 [m/s]
Cut-Out wind speed	$V_{cut,out}$	28 [m/s]
Rated Power	P_{rated}	8.0 [MW]

Appendix C

Fatigue analysis

This appendix is dedicated to the used fatigue analysis, which is performed for the verification study within BHAWC. For the verification study of Chapter 5, two different methods of assessing the fatigue of time-domain simulations are discussed below. The first method makes use of rainflow counting algorithm of [Niesłony \(2009\)](#) in order to determine the damage done to the support structure. The second method is calculating the pitch bearing damage over time.

Fatigue analysis for tower bottom moment

For the tower bottom the Fore-Aft (FA) bending motion is of interest. Especially the bending moment at the root (mudline), because there the bending moment is the largest. During the normal operation the support structure is subjected to oscillations, which are large or big in magnitude. These oscillations can be seen in the verification study in Chapter 5. In order to determine the damage done to the structure over the total lifetime of the turbine a qualitative measure should be introduced. For this qualitative measure rainflow counting can be used ([Dirlik, 1985](#)). The method can be explained by using Figure C-1. After this procedure all the oscillations are summed up. This summation can be compared with a so-called S-N curve, which provides the amount of cycles N corresponding to an applied stress S for which a material fails. By using a logarithmic scale for N , the S-N curve looks linear for most materials. The resulting relation satisfies $SN^m = \text{constant}$, which is called the Miner's rule, where m is known as the material specific Wöhler exponent. Eventually, by using this post-processed counting method, the Damage Equivalent Loads (DEL) can be calculated. By calculating the DEL, the fatigue can be compared for different experiment duration.

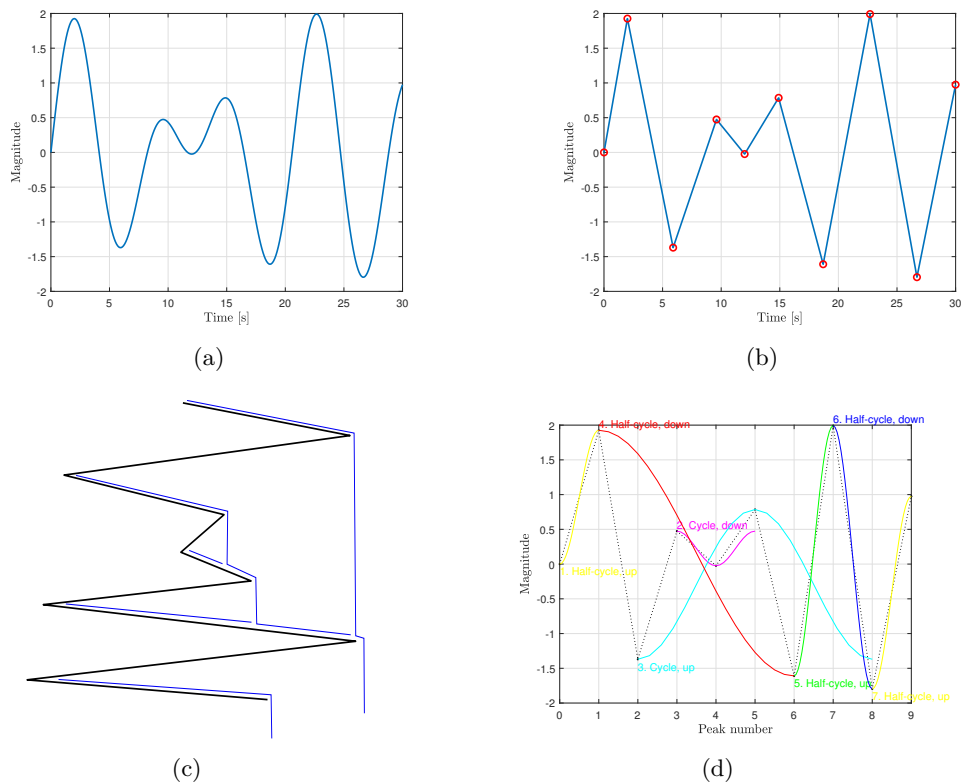


Figure C-1: The procedure of rainflow counting for an arbitrary signal. Firstly, there is a magnitude which fluctuates over time (a). Secondly, the minima and maxima of the graph are extracted (b). Thereafter, the plot is turned sideways, which results in the graph (c). This graph includes the raindrops, represented by the blue lines, which are flowing from the rightmost point downwards. The raindrops will continue to fall along the graph down until the following conditions are met. When the flow comes from a higher positive maximum (negative minimum) than the maximum (minimum) it started from. Also, when two flows meet each other from a roof above, it stops. Based on the flow lengths the graph (d) can be made with the tools provided by [Niesłony \(2009\)](#), which distinguishes half an full cycles in magnitudes

Pitch bearing fatigue estimation

The most critical part of the application of active tower damping is the insurmountable additional pitch activity. Moreover, the pitch bearing damage is regarded as one of the main critical design drivers for the application of this load reducing pitch control. The application of load reducing pitch control introduces small cyclic pitch movements with sudden direction changes. Therefore, a considerable amount of fatigue for the bearing and actuators is induced by the extra pitch activity. For the assessment of pitch bearing a rough estimate for the fatigue damage in the roller bearings is determined as follows:

$$D = \frac{1}{k} \sum_{i=1}^p \left(\cos(\theta_{pos}) \cdot M_{br,x} + \sin(\theta_{pos}) \cdot M_{br,y} \right)^p |\Delta\theta_i| \quad (\text{C-1})$$

where, $p = 3$ for spherical roller bearing, the flap-wise and edge-wise bending moments at the root of the blades are given by respectively, $M_{br,x}$ and $M_{br,y}$. The value of angular increments is given by $\Delta\theta_i$.

Bibliography

- F. D. Adegas. *Structured, Gain-Scheduled Control of Wind Turbines*. PhD thesis, PhD thesis, Aalborg University, 2013.
- Algemene Rekenkamer. Focus op kosten winderenergie op zee, 2018. <https://www.rekenkamer.nl/publicaties/rapporten/2018/09/27/focusonderzoek-kosten-van-windparken-op-zee>.
- R. J. Allemang. The modal assurance criterion—twenty years of use and abuse. *Sound and vibration*, 37(8):14–23, 2003.
- P. Apkarian and D. Noll. The \mathcal{H}_∞ control problem is solved. 2017.
- P. Apkarian, P. Gahinet, and C. Buhr. Multi-model, multi-objective tuning of fixed-structure controllers. In *2014 European Control Conference (ECC)*, pages 856–861. IEEE, 2014.
- L. Arany, S. Bhattacharya, S. Adhikari, S. Hogan, and J. Macdonald. An analytical model to predict the natural frequency of offshore wind turbines on three-spring flexible foundations using two different beam models. *Soil Dynamics and Earthquake Engineering*, 74:40–45, 2015.
- L. Arany, S. Bhattacharya, J. H. Macdonald, and S. J. Hogan. Closed form solution of eigen frequency of monopile supported offshore wind turbines in deeper waters incorporating stiffness of substructure and ssi. *Soil Dynamics and Earthquake Engineering*, 83:18–32, 2016.
- K. J. Aström and R. M. Murray. *Feedback systems: an introduction for scientists and engineers*. Princeton university press, 2010.
- F. D. Bianchi, H. De Battista, and R. J. Mantz. *Wind turbine control systems: principles, modelling and gain scheduling design*. Springer Science & Business Media, 2006.
- E. A. Bossanyi. The design of closed loop controllers for wind turbines. *Wind Energy: An International Journal for Progress and Applications in Wind Power Conversion Technology*, 3(3):149–163, 2000.

- R. D. Cook et al. *Concepts and applications of finite element analysis*. John Wiley & Sons, 2007.
- M. Damgaard, V. Zania, L. V. Andersen, and L. B. Ibsen. Effects of soil–structure interaction on real time dynamic response of offshore wind turbines on monopiles. *Engineering Structures*, 75:388–401, 2014.
- T. Dirlik. *Application of computers in fatigue analysis*. PhD thesis, University of Warwick, 1985.
- H. K. Fathy, J. A. Reyer, P. Y. Papalambros, and A. Ulsov. On the coupling between the plant and controller optimization problems. In *Proceedings of the 2001 American Control Conference*. (Cat. No. 01CH37148), volume 3, pages 1864–1869. IEEE, 2001.
- T. Fischer, W. de Vries, P. Rainey, B. Schmidt, K. Argyriadis, and M. Kühn. Offshore support structure optimization by means of integrated design and controls. *Wind Energy*, 15(1): 99–117, 2012.
- H. P. Gavin. Structural element stiffness, mass, and damping matrices. *CEE 541. Structural Dynamics*, 2014.
- M. Géradin and D. J. Rixen. *Mechanical vibrations: theory and application to structural dynamics*. John Wiley & Sons, 2014.
- K. M. Grigoriadis and R. E. Skelton. Integrated structural and control design for vector second-order systems via lmis. In *Proceedings of the 1998 American Control Conference. ACC (IEEE Cat. No. 98CH36207)*, volume 3, pages 1625–1629. IEEE, 1998.
- D.-W. Gu, P. Petkov, and M. M. Konstantinov. *Robust control design with MATLAB®*. Springer Science & Business Media, 2005.
- H. Hendriks and B. Bulder. Fatigue equivalent load cycle method. *ECN, The Netherlands, Tech. Rep. ECN-C-95-074*, 1995.
- D. J. Inman. *Vibration with control*. John Wiley & Sons, 2017.
- J. P. Jensen. Evaluating the environmental impacts of recycling wind turbines. *Wind Energy*, 22(2):316–326, 2019.
- D. d. Klerk, D. J. Rixen, and S. Voormeeren. General framework for dynamic substructuring: history, review and classification of techniques. *AIAA journal*, 46(5):1169–1181, 2008.
- W. E. Leithead and S. Dominguez. Coordinated control design for wind turbine control systems. In *Proceedings of European Wind Energy Conference and Exhibition, Athens, Greece*, volume 27, 2006.
- M. Liu and D. G. Gorman. Formulation of rayleigh damping and its extensions. *Computers & structures*, 57(2):277–285, 1995.
- J. Mohammadpour and C. W. Scherer. *Control of linear parameter varying systems with applications*. Springer Science & Business Media, 2012.

- D.-P. Molenaar. Cost-effective design and operation of variable speed wind turbines. 2003.
- C. Mone, A. Smith, B. Maples, and M. Hand. 2013 cost of wind energy. *National Renewable Energy Laboratory: Golden CO*, 2015.
- A. Niesłony. Determination of fragments of multiaxial service loading strongly influencing the fatigue of machine components. *Mechanical Systems and Signal Processing*, 23(8): 2712–2721, 2009.
- R. Osgood. Dynamic characterization testing of wind turbines. Technical report, National Renewable Energy Lab., Golden, CO (US), 2001.
- B. Paijmans, W. Symens, H. Van Brussel, and J. Swevers. Identification of interpolating affine lpv models for mechatronic systems with one varying parameter. *European Journal of Control*, 14(1):16–29, 2008.
- H. Panzer, J. Hubele, R. Eid, and B. Lohmann. Generating a parametric finite element model of a 3d cantilever timoshenko beam using matlab. Technical report, Lehrstuhl für Regelungstechnik, 2009.
- L. Y. Pao and K. E. Johnson. Control of wind turbines. *IEEE Control Systems Magazine*, 31(2):44–62, April 2011.
- V. Pascu, S. Kanev, and J.-W. van Wingerden. Adaptive tower damping control for offshore wind turbines. *Wind Energy*, 20(5):765–781, 2017.
- P. Passon, K. Branner, S. Larsen, and J. Hvenekær Rasmussen. *Offshore Wind Turbine Foundation Design*. PhD thesis, Denmark, 2015.
- M. Pastor, M. Binda, and T. Harčarik. Modal assurance criterion. *Procedia Engineering*, 48: 543–548, 2012.
- J. A. Perez, C. Pittet, D. Alazard, and T. Loquen. Integrated control/structure design of a large space structure using structured hâŁd control. *IFAC-PapersOnLine*, 49(17):302–307, 2016.
- F. Perrone and M. Kühn. Offshore wind turbine tower fore-aft fatigue load reduction by coupling control and vibrational analysis. *Journal of Ocean and Wind Energy*, 2(3):168–175, 2015.
- Rijksoverheid. Vattenfall bouwt tweede windpark op zee zonder subsidie, 2019. <https://www.rijksoverheid.nl/actueel/nieuws/2019/07/10/vattenfall-bouwt-tweede-windpark-op-zee-zonder-subsidie>.
- F. Sandner, D. Schlipf, D. Matha, R. Seifried, and P. W. Cheng. Reduced nonlinear model of a spar-mounted floating wind turbine. 2012.
- M. Shan. *Load Reducing Control for Wind Turbines.: Load Estimation and Higher Level Controller Tuning based on Disturbance Spectra and Linear*. BoD–Books on Demand, 2018.
- F. A. Shirazi, K. M. Grigoriadis, and D. Viassolo. An integrated approach towards structural and lpv controller design in wind turbines. In *American Control Conference (ACC), 2012*, pages 5789–5794. IEEE, 2012.

- M. M. d. Silva. *Computer-Aided Integrated Design of Mechatronic Systems*. PhD thesis, Katholieke Universiteit Leuven, 2009.
- S. Skogestad and I. Postlethwaite. *Multivariable feedback control: analysis and design*, volume 2. Wiley New York, 2007.
- B. Tony. Wind energy handbook, 2001.
- G. Van der Veen, M. Langelaar, S. Van Der Meulen, D. Laro, W. Aangenent, and F. van Keulen. Integrating topology optimization in precision motion system design for optimal closed-loop control performance. *Mechatronics*, 47:1–13, 2017.
- R. Van Herpen, T. Oomen, E. Kikken, M. van de Wal, W. Aangenent, and M. Steinbuch. Exploiting additional actuators and sensors for nano-positioning robust motion control. *Mechatronics*, 24(6):619–631, 2014.
- E. Van Solingen, J.-W. van Wingerden, R. De Breuker, and M. Verhaegen. Optimization of linear parameterizable \mathcal{H}_∞ controllers in the frequency domain. *IFAC Proceedings Volumes*, 47(3):736–741, 2014.
- K. Vandyshev, M. Langelaar, F. van Keulen, and J. van Eijk. Combined topology and shape optimization of controlled structures. In *EngOpt 2012-International Conference on Engineering Optimization*, 2012.
- M. Verhaegen and V. Verdult. *Filtering and system identification: a least squares approach*. Cambridge university press, 2007.
- R. Wisser, M. Hand, J. Seel, and B. Paulos. Reducing wind energy costs through increased turbine size: Is the sky the limit? *Lawrence Berkeley National Laboratory*, 2016.

Glossary

List of Acronyms

ATD	Active Tower Damper
BHAWC	Bonus Horizontal Axis Wind turbine Code
CL	Closed-Loop
CPC	Collective Pitch Controller
CSO	Controller Structure Optimization
DEL	Damage Equivalent Loads
DoF	Degrees of Freedom
FLS	Fatigue Limit State
FA	Fore-Aft
LCoE	Levelized Costs of Energy
LFT	Linear Fractional Transformation
LMIs	Linear Matrix Inequalities
MAC	Modal Assurance Criterion
MIMO	Multiple-Input Multiple-Output
OWT	Offshore Wind Turbine
OL	Open-Loop
ODE	Ordinary Differential Equation
ODEs	Ordinary Differential Equations
RHP	Right-Half-Plane

RNA	Rotor Nacelle Assembly
RSC	Rotor Speed Controller
SS	Side-Side
SGRE	Siemens Gamesa Renewable Energy
SLOW	Simplified Low Order Wind turbine
SISO	Single-Input Single-Output
SVD	Singular Value Decomposition
TP	Transition Piece
ULS	Ultimate Limit State
VAF	Variance Accounted For